

Supporting Information

Optimized NiFe-Based Coordination Polymer Catalysts: Sulfur-Tuning and *Operando* Monitoring of Water Oxidation

Yonggui Zhao,[‡] Wenchao Wan,[‡] Nanchen Dongfang, C. A. Triana, Lewis Douls, Rolf Erni, Chong Huang, Marcella Iannuzzi, and Greta R. Patzke*

Y. G. Zhao, Dr. W. C. Wan, N. C. Dongfang, Dr. C. A. Triana, L. Douls, C. Huang, PD Dr. M. Iannuzzi, and Prof. G. R. Patzke

Department of Chemistry, University of Zurich, Winterthurerstrasse 190, CH-8057 Zurich, Switzerland

E-mail: greta.patzke@chem.uzh.ch

Dr. R. Erni

Electron Microscopy Center, Empa, Swiss Federal Laboratories for Materials Science and Technology, Überlandstrasse 129, CH-8600 Dübendorf, Switzerland

*Corresponding author

[‡]These authors contributed equally

Table of Contents

1. Experimental details and methods	S3
2. Modeling of the local coordination environments (Figure S1)	S8
3. Basic characterization of as-prepared samples	S9
3.1 Characterization of O _d -R-NiFe-CPs and S-R-NiFe-CPs (Figures S2-S14).....	S9
3.2 Characterization of NiFe-O and S-NiFe-O (Figures S15-S17)	S17
4. <i>Ex situ</i> XAS, EPR, and XPS characterization	S19
4.1 Ni <i>K</i> -edge XAS data of O _d -R-NiFe-CPs, S-R-NiFe-CPs, NiFe-O, and S-NiFe-O (Figure S18).....	S19
4.2 Fe <i>K</i> -edge XAS data of O _d -R-NiFe-CPs, S-R-NiFe-CPs, NiFe-O, and S-NiFe-O (Figure S19).....	S20
4.3 XAS characterization of S-R-NiFe-CPs (2, 5, 10, 20, and 50 mg) (Figures S20-S23)	S21
4.4 EPR characterization of as-investigated catalysts (Figure S24).....	S25
4.5 XPS characterization of as-investigated catalysts (Figures S25-S26)	S26
5. Electrochemical OER performance (Figures S27-S34).....	S28
6. Post-catalytic characterization (Figure S35).....	S36
7. OER activities of O _d -R-NiFe-CPs with different concentrations of K ₂ SO ₄ (Figure S36).....	S37
8. <i>Operando</i> XAS characterization (Figures S37-S41)	S38
9. <i>Operando</i> EIS characterization (Figure S42)	S42
10. pH-dependent OER experiments (Figure S43).....	S43
11. Adsorption slab models for DFT simulations (Figures S44-46)	S44
Table S1. ICP-MS results in fresh 1.0 M KOH before and after OER measurements	S46
Table S2. ICP-MS results: atomic Ni/Fe/S ratios for the as-synthesized catalysts	S46

Table S3. Fitting parameters of Ni <i>K</i> -edge EXAFS spectra for as-prepared catalysts and references.....	S47
Table S4. Fitting parameters of Fe <i>K</i> -edge EXAFS spectra for as-prepared catalysts and references	S48
Table S5. Fitting parameters of <i>operando</i> Ni <i>K</i> -edge EXAFS spectra of S-R-NiFe-CPs for OER.....	S49
Table S6. Fitting parameters of <i>operando</i> Fe <i>K</i> -edge EXAFS spectra of S-R-NiFe-CPs for OER.....	S50
Table S7. Comparison of OER performance of as-prepared catalysts with recent representative studies on NiFe-based OER electrocatalysts.....	S51
References	S52
Supplementary Discussion I.....	S10
Supplementary Discussion II.....	S34

1. Experimental details and methods

Preparation of Fe-free purified KOH electrolyte. The Fe-free KOH electrolyte was prepared via a high purity Ni-based hydroxide adsorption strategy.^[1] In a typical procedure, 2 g of high purity nickel(II) nitrate hexahydrate ($\geq 99.999\%$) was dissolved into 4 mL of DI water. Then, 20 mL of 1.0 M KOH was injected into the above Ni-containing solution to form high purity Ni(OH)₂. The precipitate was collected via centrifugation and washed three times with a mixture of 20 mL of DI water and 2 mL of 1.0 M KOH. Afterward, the precipitate was dispersed into 50 mL of 1.0 M KOH for 10 min. Finally, the Fe-free KOH was obtained by centrifugation. Based on the ICP-MS results (**Table S1**), the as-prepared purified KOH solution showed <1 ppb of Fe, which was in agreement with previous studies.^[1-4]

Materials characterization. Powder X-ray diffraction (PXRD) patterns were recorded on a STOE STADI P diffractometer (transmission mode, Ge monochromator) with Mo K α ($\lambda = 0.7093\text{ \AA}$) radiation (50 kV and 40 mA). Field-emission scanning electron microscopy (FESEM-Zeiss Supra 50 VP), and transmission electron microscopy (TEM-FEI Tecnai G2 Spirit) were used for investigating the morphological properties of the as-prepared samples. The elemental compositions of the as-prepared samples were analyzed with FESEM-energy-dispersive X-ray spectroscopy (EDX) and inductively coupled plasma mass spectrometry (Agilent 8800 ICP-MS). High-resolution TEM (HR-TEM), high angle annular dark field-scanning transmission electron microscopy (HAADF-STEM), and scanning transmission electron microscopy-energy dispersive X-ray spectroscopy (STEM-EDX) element mappings were recorded on a FEI Titan Themis equipped with a hexapole-type aberration corrector for scanning transmission electron microscopy (CEOS DCOR) and a Super EDX system. X-ray photoelectron spectroscopy (XPS) studies were performed on a PerkinElmer PHI 1600 ESCA system with Mg K α radiation (1253.6 eV). Room temperature electron paramagnetic resonance (EPR) spectra were recorded on a Bruker MiniScope MS 5000 spectrometer.

***Ex situ and operando* X-ray absorption spectroscopy (XAS) measurements.** *Ex situ* and *operando* X-ray absorption near-edge structure (XANES) and extended X-ray absorption fine structure (EXAFS) tests (Ni and Fe *K*-edge) were performed at the European Synchrotron Radiation Facility (ESRF), Swiss-Norwegian Beamline BM31, Grenoble, France. All the XAS data were collected via a transmission mode with a Si(111) double crystal monochromator, which was cooled with liquid nitrogen. *Ex situ* tests were performed via a cellulose dispersion strategy. In a typical example, the solid powder samples were diluted with certain amounts of cellulose to reach an absorption step of ca. 1. The XANES spectra of reference Ni and Fe foils

were measured first and used for energy calibrations. *Operando* measurements were carried out at room temperature with an in-house developed electrochemical cell. A standard three-electrode system equipped with a reference Hg/HgO electrode (1.0 M KOH), counter graphite rod electrode, and carbon paper as the working electrode, respectively, was used. The catalyst layer was prepared by drop-coating on carbon paper. The loading mass was 2.0~3.0 mg/cm². Due to the high catalytic activities of the investigated samples in 1.0 M KOH, our *operando* measurements were thereby conducted in 0.1 M KOH to reduce the influence of gas bubble formation on the collected XAS signals at high voltage. During the *operando* XAS experiments, the chronoamperometry method was applied by a stepwise increase from 0.8 to 1.5 V vs. RHE. In order to improve the quality of the XAS signal, all *operando* XAS signals recorded at the constant potential were repeated 6 times (~3 min per spectrum) at the Ni K-edge. Due to the low amounts of Fe ions in the investigated samples, the acquisition time at the Fe K-edge was increased up to 15 min per spectrum. Then, the collected raw XAS signals (same conditions) were merged through the ATHENA and used for further analysis. The EXAFS data were k^3 -weighted by the wavevector k , and analyzed in the k -range from 0 to 12 Å⁻¹. The Fourier transform (FT) spectra in the real-space were analyzed in the interval from 0 to 6 Å. For the fitting of XAS data, the fitting of reference samples was conducted first to obtain a S_0^2 value, which was used as a constant value for other samples. All EXAFS spectra are presented without phase correction.

Preparation of working electrode. First, the catalyst inks were prepared by dispersion of 5.0 mg of catalysts and 2 mg carbon black in 1 mL of ethanol and 50 µL of 5 wt% Nafion solution under sonication for 30 mins. Then, a total of 6 µL of the catalyst inks were dropped on a glassy carbon rotating disk electrode (GC-RDE, diameter of 3 mm) with a loading mass of ~0.4 mg/cm². Afterward, the electrode was dried at room temperature overnight before use.

Electrocatalytic oxygen evolution reaction (OER). OER measurements were performed at room temperature in 1.0 M KOH (pH~13.80) with a Metrohm Autolab PGSTAT302N potentiostat. A standard three-electrode system using a reference Hg/HgO electrode (1.0 M KOH), counter graphite rod electrode, and GC-RDE as the working electrode, respectively, was used. Before the measurements, the GC-RDE was polarized with 50 cycles of cyclic voltammetry (CV) at 50 mV/s without any rotations. Then, the CV curve of OER was recorded at a low scan rate of 5 mV/s with a rotation of 1600 rpm. All potentials were converted to RHE according to $E(\text{RHE}) = E + E(\text{Hg/HgO}) + 0.059 \times \text{pH}$ with a 90 % iR-compensation. All the tests were repeated at least 3 times to ensure data reproducibility. Electrochemical impedance spectroscopy (EIS) measurements were performed within a frequency range from 0.01 Hz to

10 k Hz (5 mV amplitude). The electrochemical surface area (ECSA) was calculated according to $ECSA = \text{geometric surface area} \times C_{dl}/C_0$, where C_{dl} is the double-layer capacitance (C_{dl}) and C_0 is 0.04 mF/cm². The CV curves are recorded in a non-Faradaic region from 1.21 and 1.31 V with a scan rate increase from 10 mV/s to 100 mV/s. Durability tests were performed with both CV cycling and chronopotentiometric methods.

Faradaic efficiency was calculated based on the rotating ring-disk electrode theory (RRDE):^[1,5]

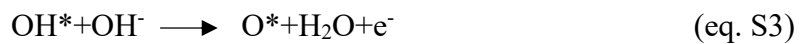
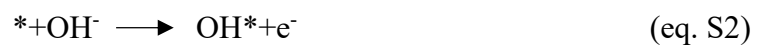
$$\text{Faradaic efficiency} = i_{\text{ring}} / (i_{\text{disk}} \times N) \quad (\text{eq. S1})$$

where i_{disk} and i_{ring} are disk and ring currents, respectively. N is the current collection coefficient and is equal to 0.2. A galvanostatic method with a rotation speed of 1600 rpm was employed for the measurements.

Density function theory (DFT) calculations.

All DFT simulations were calculated using the CP2K package with Grimme D3 corrected PerdewBurke-Ernzerhof (PBE).^[6-8] A 500 Ry was set up for plane-wave cut-off energy. Goedecker-Teter-Hutter (GTH) pseudopotential and DZVP-MOLOPT-GTH basis were employed to investigate the local molecular environment. The theoretical model was built by the NiO₂ (012)-terminated surface. Fe atoms were inserted afterward by substituting 1/3 of Ni atoms. A built 4×4×2 supercell with a total of 128 atoms was used for all simulations. The simulated energy in **Figure S2** is calculated based on a built 10×10×2 supercell with a total of 384 atoms. The Broyden-Fletcher-Goldfarb-Shanno algorithm was used to optimize the built models, and the convergence criterion of the forces was 10⁻⁴ bohr/hartree. During the optimization process, the residual force was set up for 0.05 eV/Å, moreover, the atomic positions were fully relaxed until a maximum energy difference. A 15 Å thickness of vacuum layer was added into the built supercell to remove the interaction effects arising from the surfaces.

In the alkaline conditions, a conventional adsorbate evolution mechanism (AEM) is described as follows:^[9-11]



where * represents an active adsorption site, and OH*, O*, and OOH* are the corresponding OER intermediates, respectively.

As such an AEM pathway, the Gibbs free energy (ΔG) changes of each step were calculated by the following equations.

$$\Delta G_1 = E_{\text{OH}^*} - E^* - E_{\text{H}_2\text{O}} + 1/2 E_{\text{H}_2} + (\Delta \text{ZPE} - T\Delta S)_1 - eU \quad (\text{eq. S6})$$

$$\Delta G_2 = E_{\text{O}^*} - E_{\text{OH}^*} + 1/2 E_{\text{H}_2} + (\Delta \text{ZPE} - T\Delta S)_2 - eU \quad (\text{eq. S7})$$

$$\Delta G_3 = E_{\text{OOH}^*} - E_{\text{O}^*} - E_{\text{H}_2\text{O}} + 1/2 E_{\text{H}_2} + (\Delta \text{ZPE} - T\Delta S)_3 - eU \quad (\text{eq. S8})$$

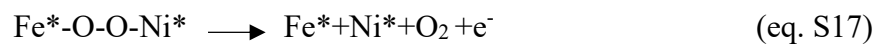
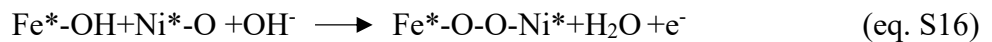
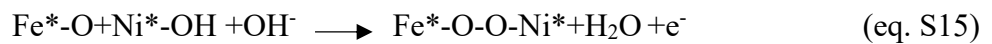
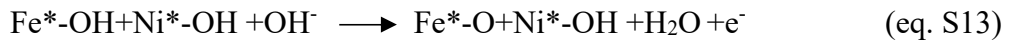
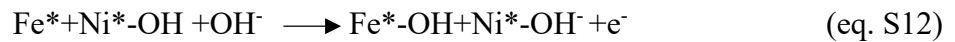
$$\Delta G_4 = 4.92 \text{ eV} - E^* + E_{\text{OOH}^*} - E_{\text{O}_2} - 1/2 E_{\text{H}_2} - (\Delta \text{ZPE} - T\Delta S)_4 - eU \quad (\text{eq. S9})$$

Therefore, the theoretical overpotential η_{theory} is defined as:

$$\eta_{\text{theory}} = \max \{ \Delta G_1, \Delta G_2, \Delta G_3, \Delta G_4 \} / e - 1.23 \text{ V} \quad (\text{eq. S10})$$

Where E_{M^*} denotes the binding energy for the adsorption intermediates. ΔZPE and ΔS are the changes of zero-point energy and entropy corrections, respectively. U is the additional bias, which is used for the computation of reaction-free energy in each step. Since all the reactions occurred at room temperatures, the temperature effects were not involved in this study.

As evident by the pH-dependent experiments (**Figure S43**), our results indicate that the as-investigated NiFe-based catalysts proceed via a non-concerted proton-electron transfer process. If such a process occurs, the OER process is suggested to undergo a dual-site mechanism (DSM) pathway.^[12-15] Based on recent studies, we propose the following DSM pathway for our catalysts.



Therefore, the Gibbs free energy (ΔG) changes of each step in a DSM pathway were calculated by the following equations.

$$\Delta G_1 = E_{\text{Fe}^* + \text{Ni}^* - \text{OH}} - E_{\text{Fe}^* + \text{Ni}^*} - E_{\text{H}_2\text{O}} + 1/2 E_{\text{H}_2} + (\Delta \text{ZPE} - T\Delta S)_1 - eU \quad (\text{eq. S18})$$

$$\Delta G_2 = E_{\text{Fe}^* - \text{OH} + \text{Ni}^* - \text{OH}} - E_{\text{Fe}^* + \text{Ni}^* - \text{OH}} - E_{\text{H}_2\text{O}} + 1/2 E_{\text{H}_2} + (\Delta \text{ZPE} - T\Delta S)_2 - eU \quad (\text{eq. S19})$$

$$\Delta G_3 = E_{\text{Fe}^*-\text{O}+\text{Ni}^*-\text{OH}} - E_{\text{Fe}^*-\text{OH}+\text{Ni}^*-\text{OH}} + 1/2 E_{\text{H}_2} + (\Delta \text{ZPE} - T\Delta S)_3 - eU \quad (\text{eq. S20})$$

$$\Delta G_{3^*} = E_{\text{Fe}^*-\text{OH}+\text{Ni}^*-\text{O}} - E_{\text{Fe}^*-\text{OH}+\text{Ni}^*-\text{OH}} + 1/2 E_{\text{H}_2} + (\Delta \text{ZPE} - T\Delta S)_{3^*} - eU \quad (\text{eq. S21})$$

$$\Delta G_4 = E_{\text{Fe}^*-\text{O}-\text{O}-\text{Ni}^*} - E_{\text{Fe}^*-\text{O}+\text{Ni}^*-\text{OH}} + 1/2 E_{\text{H}_2} + (\Delta \text{ZPE} - T\Delta S)_4 - eU \quad (\text{eq. S22})$$

$$\Delta G_{4^*} = E_{\text{Fe}^*-\text{O}-\text{O}-\text{Ni}^*} - E_{\text{Fe}^*-\text{OH}+\text{Ni}^*-\text{O}} + 1/2 E_{\text{H}_2} + (\Delta \text{ZPE} - T\Delta S)_{4^*} - eU \quad (\text{eq. S23})$$

$$\Delta G_5 = 4.92 \text{ eV} + E_{\text{Fe}^*+\text{Ni}^*} - E_{\text{Fe}^*-\text{O}-\text{O}-\text{Ni}^*} + E_{\text{O}_2} - (\Delta \text{ZPE} - T\Delta S)_5 - eU \quad (\text{eq. S24})$$

It should be noted that we simulated two different pathways in eq.13 and eq.14. This is mainly because that the deprotonation process can occur at both Ni and Fe sites in this step. We discussed this part in more detail in the main text.

2. Modeling of the local coordination environment

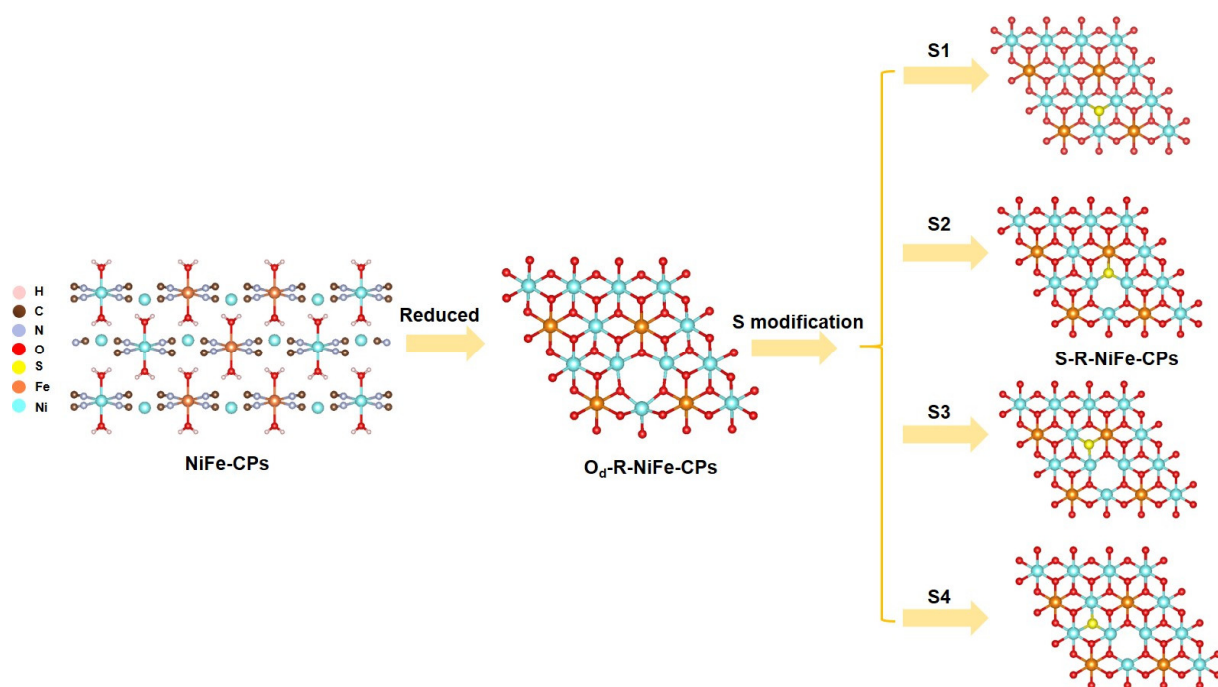


Figure S1. Schematic diagram of the synthetic process and the proposed reaction pathway during the sulfidation process.

3. Basic characterization of as-prepared samples

3.1 Characterization of O_d-R-NiFe-CPs and S-R-NiFe-CPs

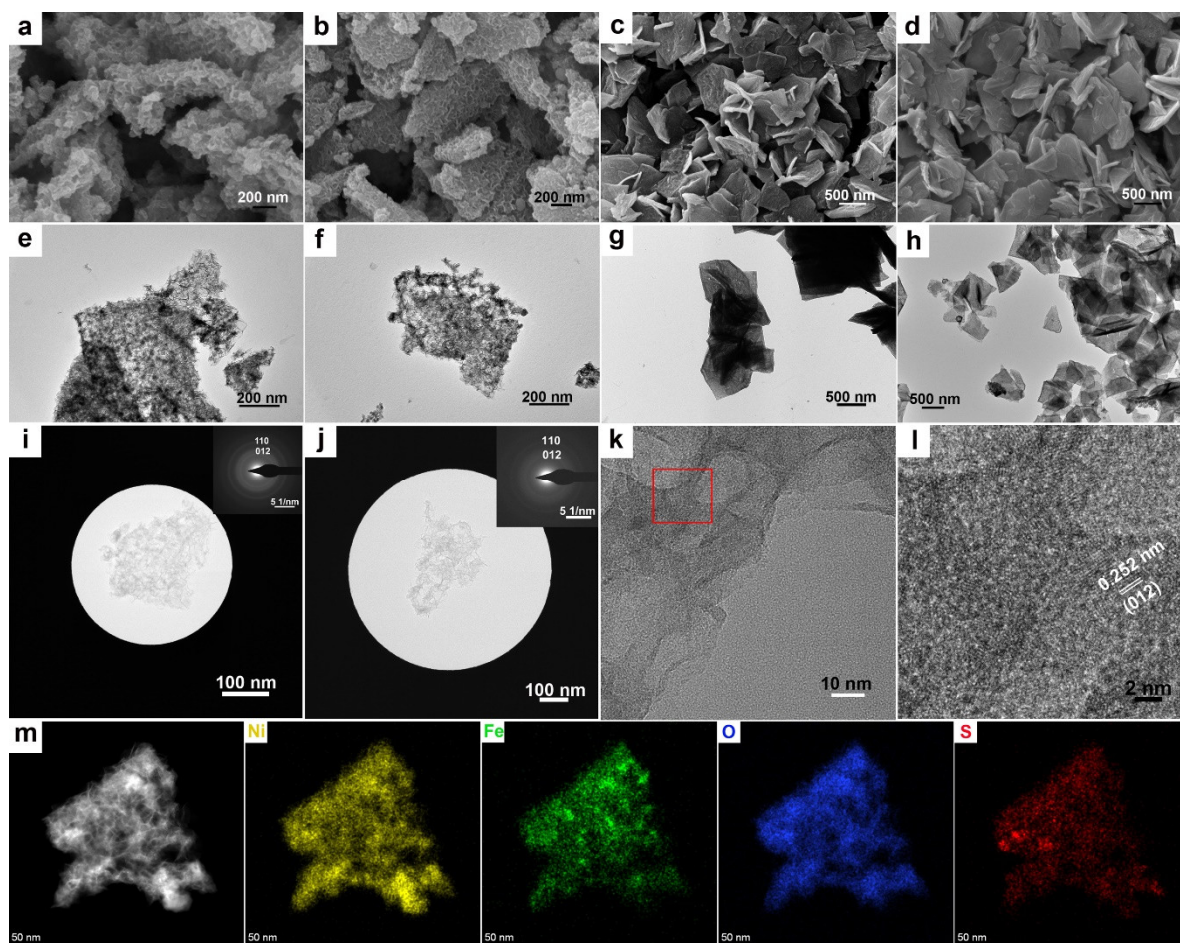


Figure S2. Representative FESEM and TEM images of: (a, e) O_d-R-NiFe-CPs, (b, f) S-R-NiFe-CPs, (c, g) NiFe-O, (d, h) S-NiFe-O; (i, j) HR-TEM images and the corresponding SAED patterns of O_d-R-NiFe-CPs and S-R-NiFe-CPs; (k, l) HR-TEM images of S-R-NiFe-CPs; (m) STEM-EDX elemental maps of S-R-NiFe-CPs (yellow = Ni, green = Fe, blue = O, red = S).

Supplementary Discussion I: Synthesis and characterization of O_d-R-NiFe-CPs and S-R-NiFe-CPs

Field-emission scanning electron microscopy (FESEM, **Figures S2a and S3a**) and transmission electron microscopy (TEM, **Figures S2e and S3b**) images demonstrate the ultra-thin nanosheet morphology of the investigated samples. The selected area electron diffraction (SAED, **Figure S2i**) pattern exhibits weakened intensities of diffraction rings, and the high-resolution transmission electron microscopy (HR-TEM, **Figure S3c,d**) images show disordered domains. This suggests low crystallinity and the presence of abundant structural deficiencies in the as-prepared O_d-R-NiFe-CPs, in agreement with the broad diffraction peaks observed in the PXRD pattern (**Figure S5**). Furthermore, FESEM and scanning transmission electron microscopy (STEM) combined with energy-dispersive X-ray spectroscopy (EDX) maps illustrate the homogenous element distributions of Ni, Fe, and O, which indicates the formation of homogenous O_d-R-NiFe-CPs nanosheets (**Figures S3e and S4**).

The PXRD patterns (**Figure S5**) of S-R-NiFe-CPs (2 and 5 mg) feature similar diffraction peaks without any impurities compared with O_d-R-NiFe-CPs. This indicates that partial incorporation of S atoms does not influence the pristine crystal structures of O_d-R-NiFe-CPs. FESEM and TEM images (**Figures S2b,f and S6d-f**) (5 mg) reveal the ultra-thin nanosheet morphology of S-R-NiFe-CPs. SAED and HR-TEM images (**Figure S2j**) of S-R-NiFe-CPs further illustrate its low crystallinity. Meanwhile, HR-TEM images (**Figure S2k,l**) indicate that (012) is the main exposed crystal plane in S-R-NiFe-CPs with a lattice spacing of 0.252 nm (Ni(OH)₂·0.75H₂O, PDF No. 38-0715), in line with the HR-TEM results of O_d-R-NiFe-CPs (**Figure S3c,d**). STEM-EDX element maps further demonstrate the ultra-thin morphological properties of S-R-NiFe-CPs with a homogenous element distribution of Ni, Fe, O, and S (**Figure S2m**). The PXRD patterns (**Figure S5**) of the as-obtained S-R-NiFe-CPs (10, 20, and 50 mg) are similar to those of O_d-R-NiFe-CPs but exhibit additional peaks at $2\theta \approx 14.3^\circ$, 17.2° , and 24.3° . These newly appearing peaks are ascribed to the formation of Ni₃S₄ (PDF No. 76-1813), indicating that incorporation of excessive S amounts affects the phase purity of O_d-R-NiFe-CPs. Moreover, FESEM and TEM characterizations were further carried out to investigate the morphological evolution in S-R-NiFe-CPs (2 to 50 mg) (**Figures S6-S8**). Specifically, as confirmed by FESEM and TEM images (**Figures S6-S8**) in the presence of 50 mg of TAA, the as-prepared S-R-NiFe-CPs exhibit a distinct nanoparticle morphology compared with the samples obtained with low amounts of TAA (2 and 5 mg). Furthermore, the SAED patterns (**Figure S8c,d**) of S-R-NiFe-CPs (50 mg) not only exhibit somewhat weaker intensity of the diffraction rings but also display additional bright dots. This corroborates that the as-synthesized S-R-NiFe-CPs (50 mg) contain a secondary phase beyond the initial O_d-R-NiFe-CPs. Detailed HR-TEM images of S-R-NiFe-CPs (50 mg) were therefore further recorded. As illustrated in **Figure S8e,f**, HR-TEM images of S-R-NiFe-CPs (50 mg) exhibit two characteristic domains with a lattice spacing of 0.283 and 0.253 nm, respectively, corresponding to the exposed crystal planes (311) of Ni₃S₄ and (012) of O_d-R-NiFe-CPs. These results are consistent with our previous PXRD analyses of S-R-NiFe-CPs (**Figure S5**).

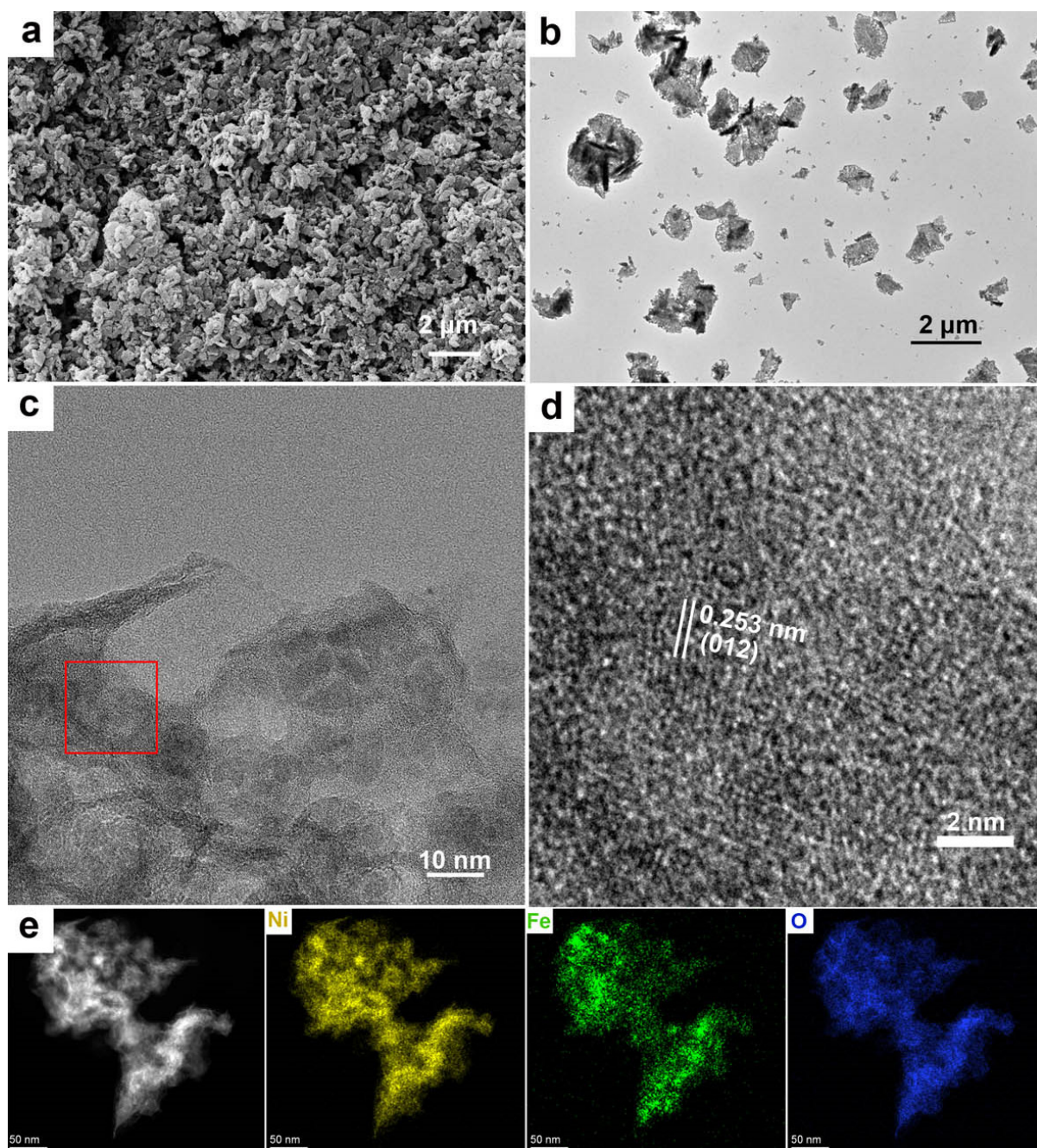


Figure S3. (a, b) FESEM and TEM images of as-prepared O_d -R-NiFe-CPs. (c, d) HR-TEM images of as-prepared O_d -R-NiFe-CPs. (e) HAADF-STEM images and STEM-EDX element mappings of O_d -R-NiFe-CPs.

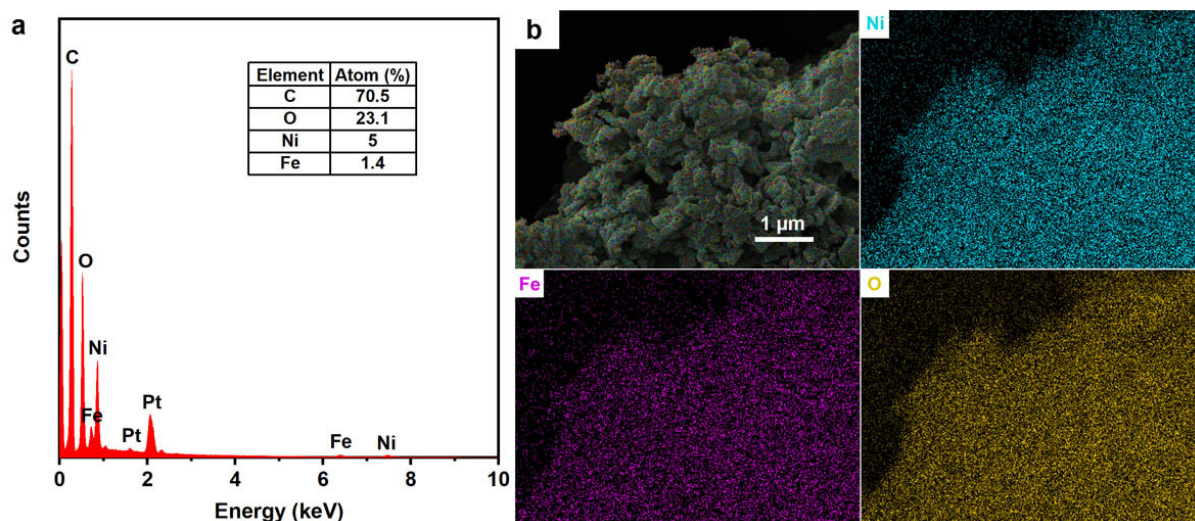


Figure S4. FESEM-EDX spectrum (a) and element mappings (b) of as-prepared O_d -R-NiFe-CPs.

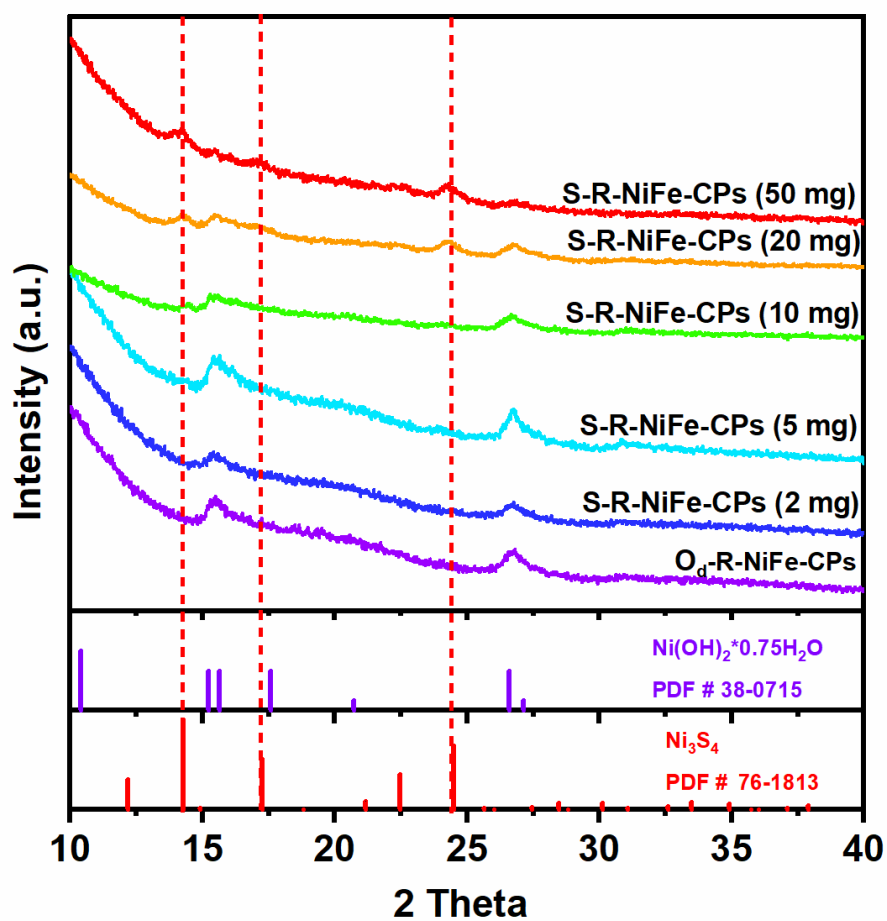


Figure S5. PXRD patterns of as-prepared O_d -R-NiFe-CPs and S-R-NiFe-CPs with different amounts of TAA.

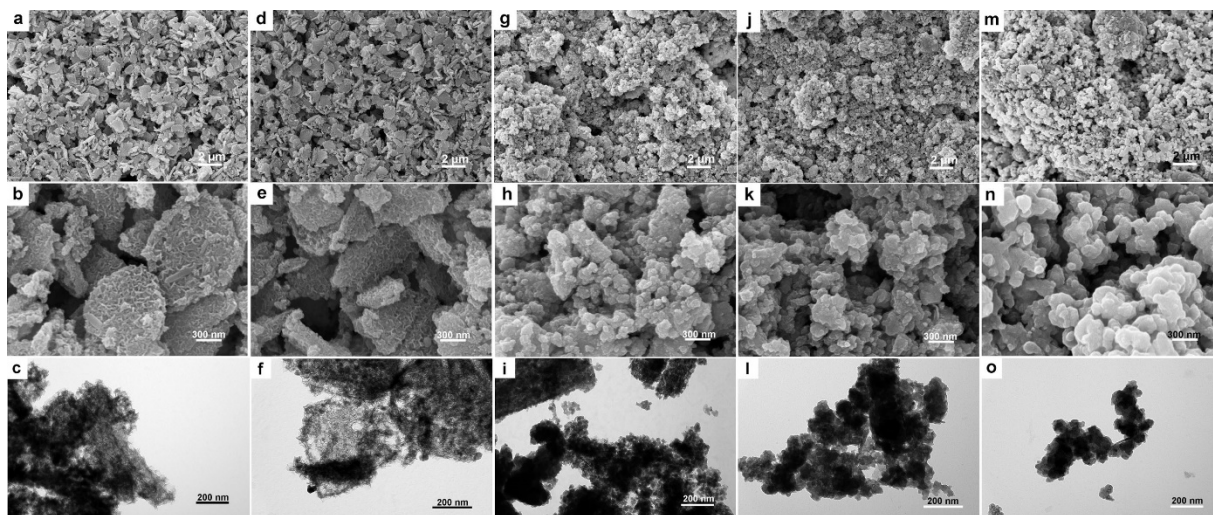


Figure S6. FESEM and TEM images of as-prepared S-R-NiFe-CPs with different amounts of TAA: (a-c) 2 mg; (d-f) 5 mg; (g-i) 10 mg; (j-l) 20 mg; (m-o) 50 mg.

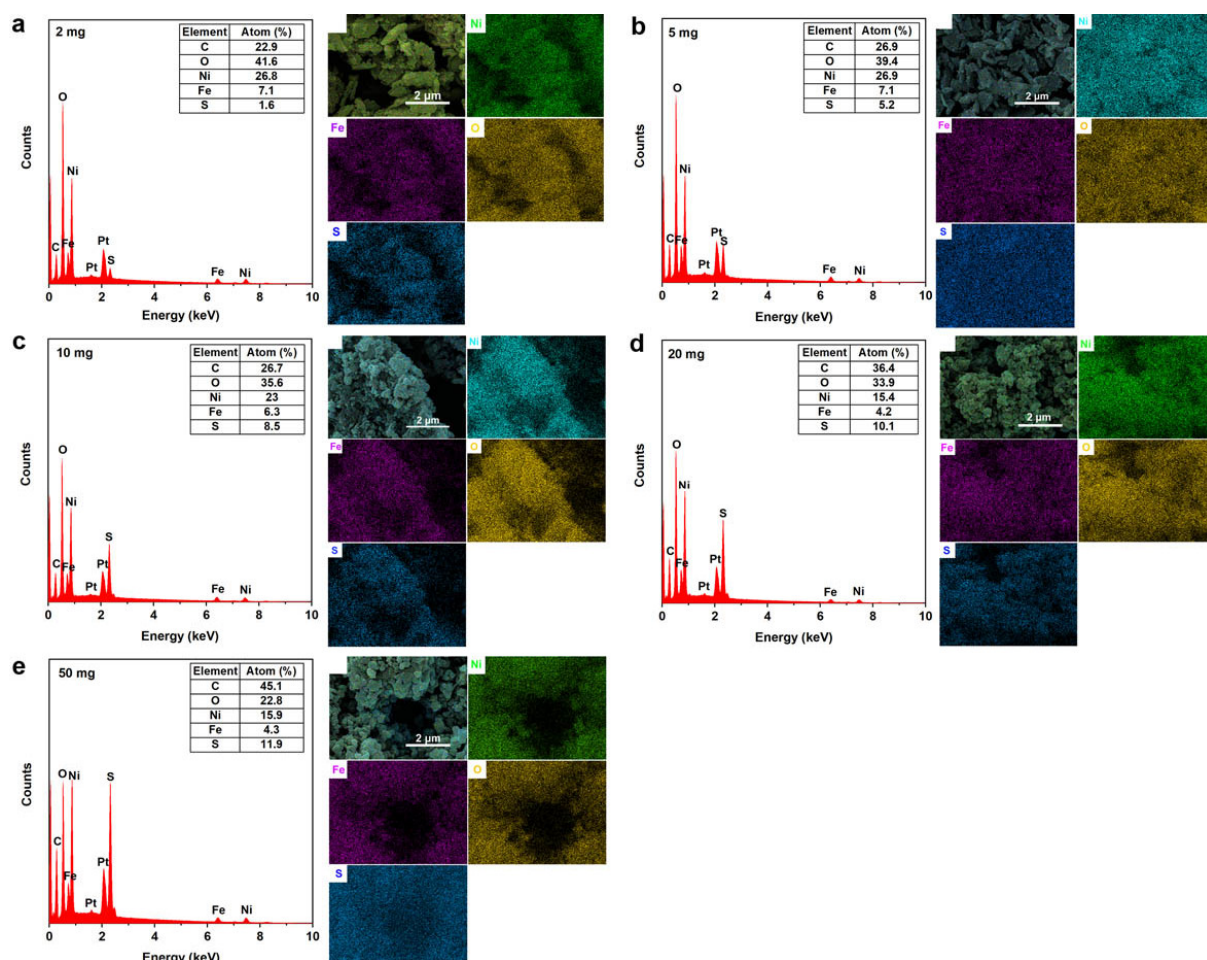


Figure S7. FESEM-EDX spectra and element mappings of as-prepared S-R-NiFe-CPs with different amounts of TAA: (a) 2 mg; (b) 5 mg; (c) 10 mg; (d) 20 mg; (e) 50 mg.

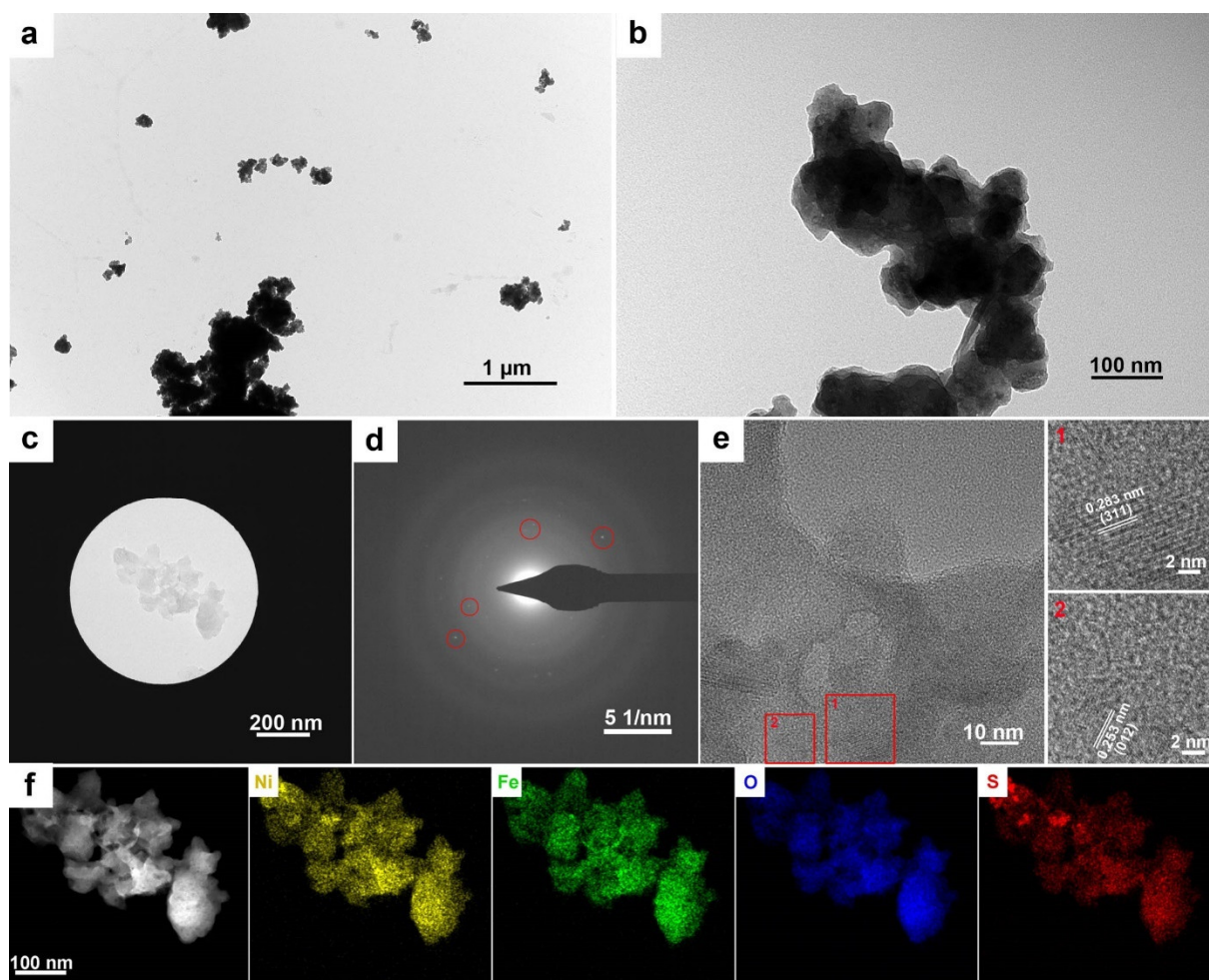


Figure S8. (a, b) TEM images of as-prepared S-R-NiFe-CPs (50 mg). (c, d) HR-TEM images and corresponding SAED pattern. (e) HR-TEM images. (f) HAADF-STEM image and STEM-EDX element mappings.

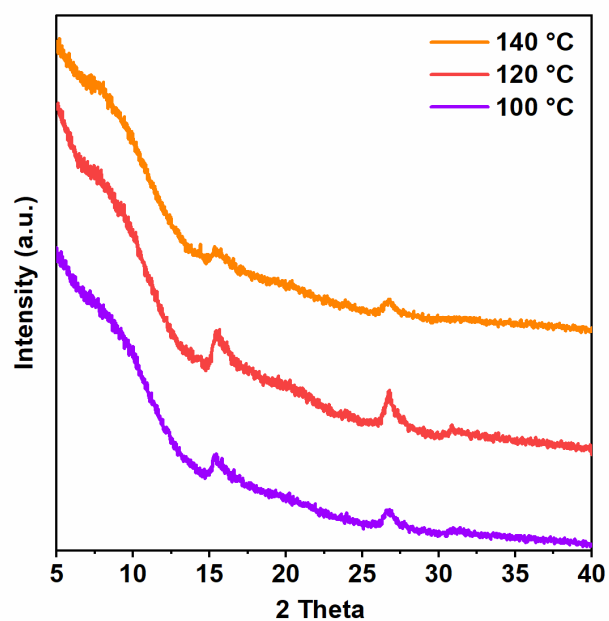


Figure S9. PXRD patterns of as-prepared S-R-NiFe-CPs (5 mg) at different reaction temperatures.

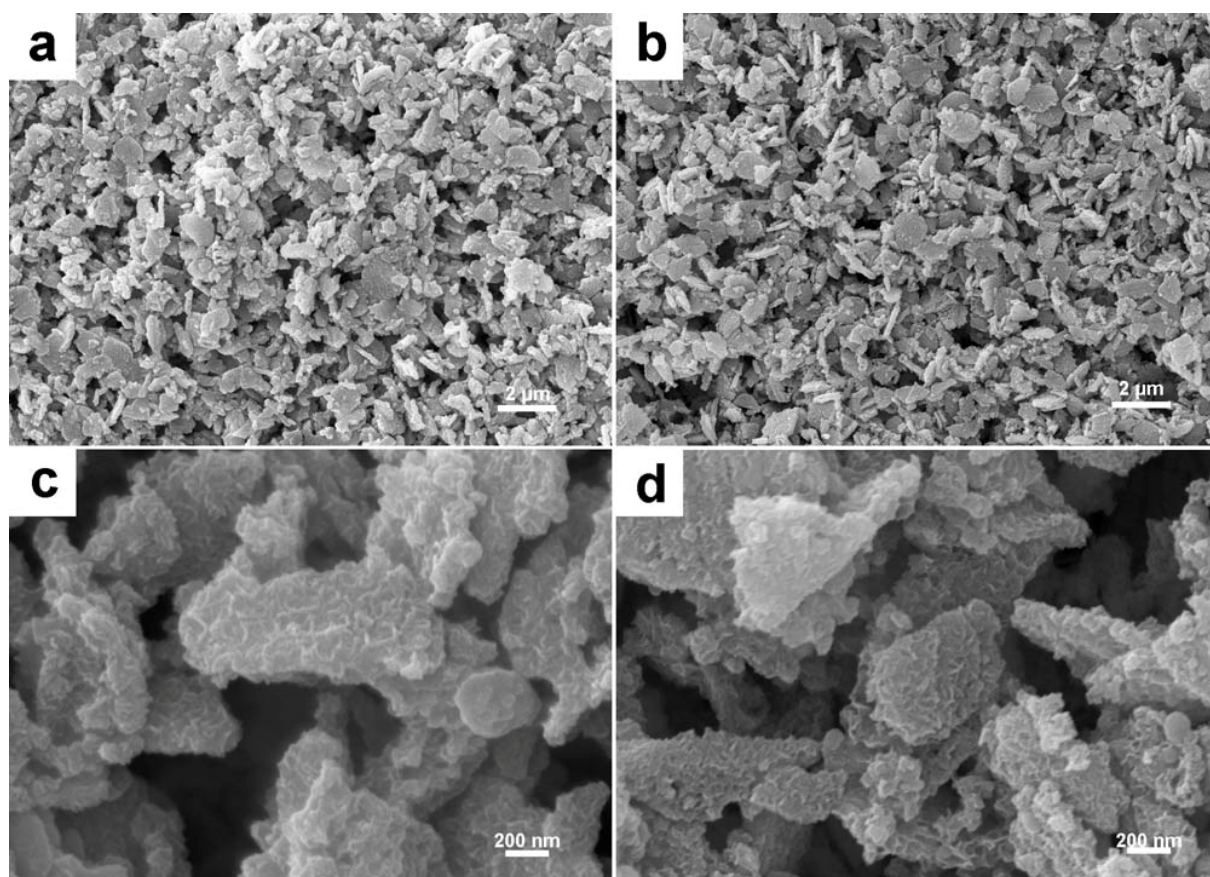


Figure S10. FESEM images of as-prepared S-R-NiFe-CPs (5 mg) at different reaction temperatures: (a, c) 100 °C; (b, d) 140 °C.

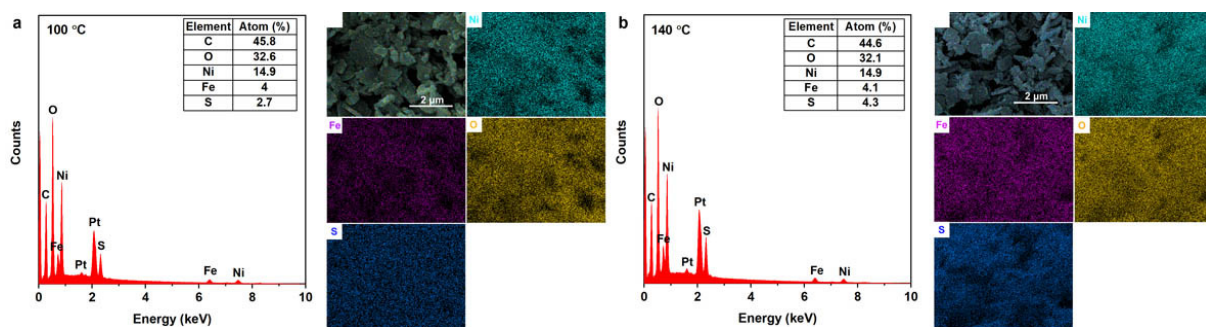


Figure S11. FESEM-EDX spectra and element mappings of as-prepared S-R-NiFe-CPs (5 mg) at different reaction temperatures: (a, c) 100 °C; (b, d) 140 °C.

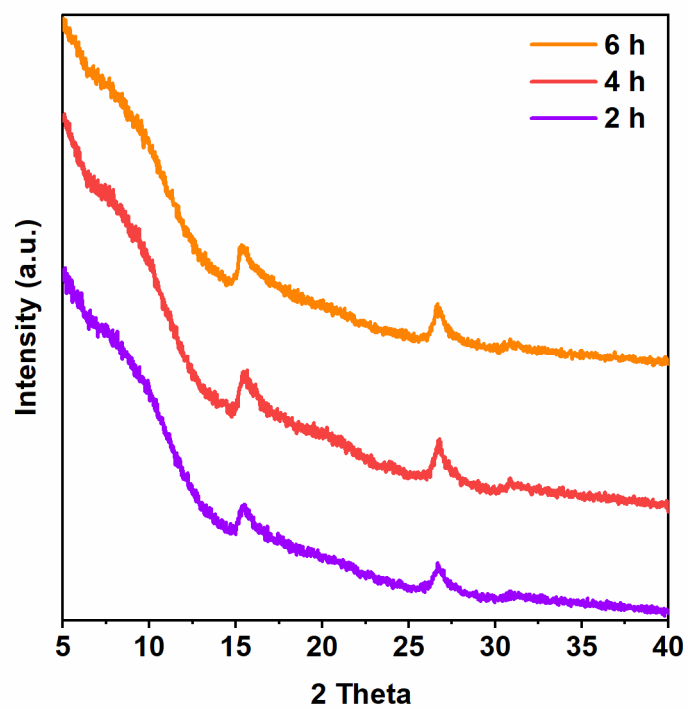


Figure S12. PXRD patterns of as-prepared S-R-NiFe-CPs (5 mg) after different reaction times.

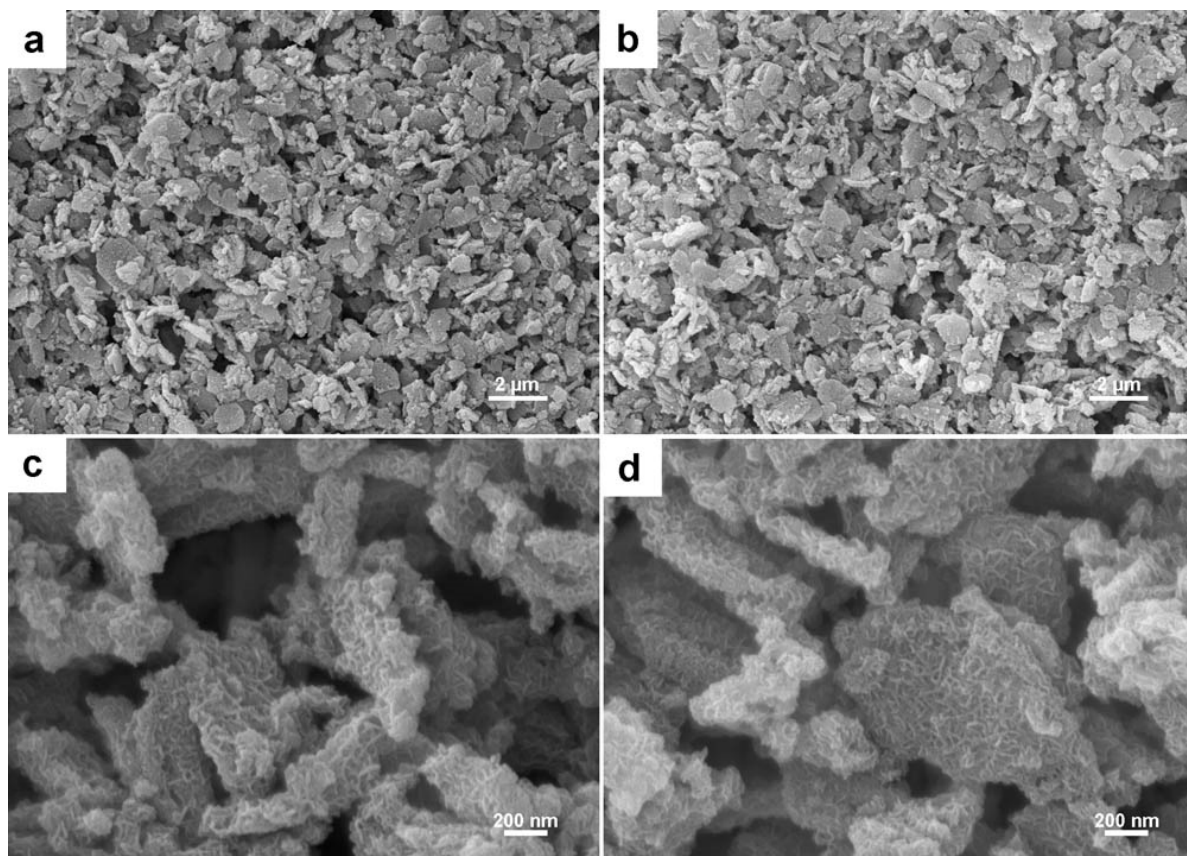


Figure S13. FESEM images of as-prepared S-R-NiFe-CPs (5 mg) after different reaction times: (a, c) 2 h; (b, d) 6 h.

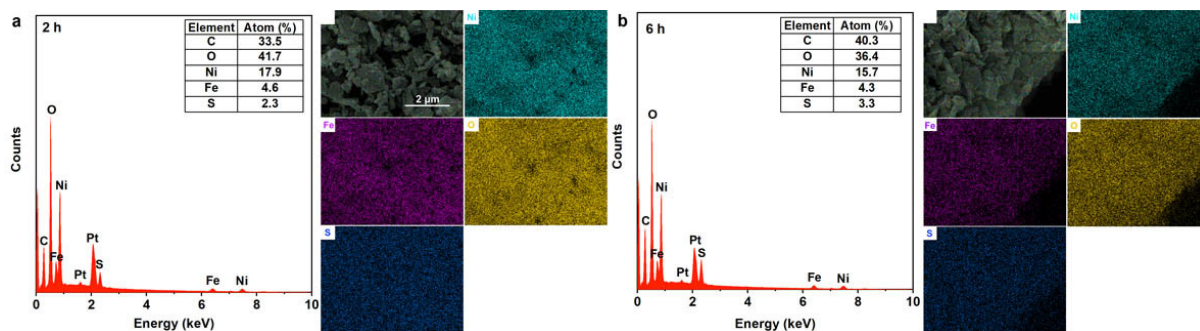


Figure S14. FESEM-EDX spectra and element mappings of as-prepared S-R-NiFe-CPs (5 mg) after different reaction times: (a, c) 2 h; (b, d) 6 h.

3.2 Characterization of NiFe-O and S-NiFe-O

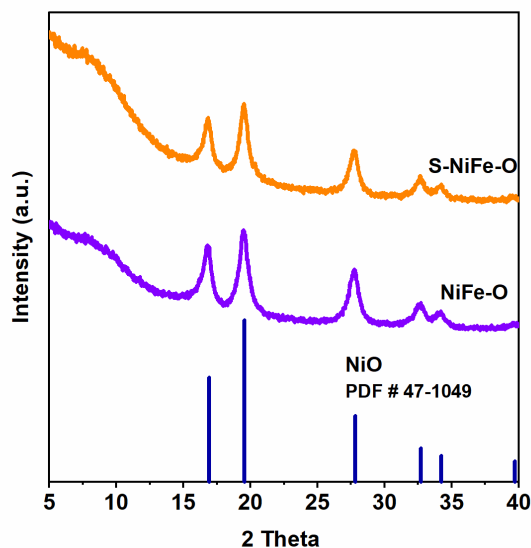


Figure S15. PXRD patterns of as-prepared NiFe-O and S-NiFe-O.

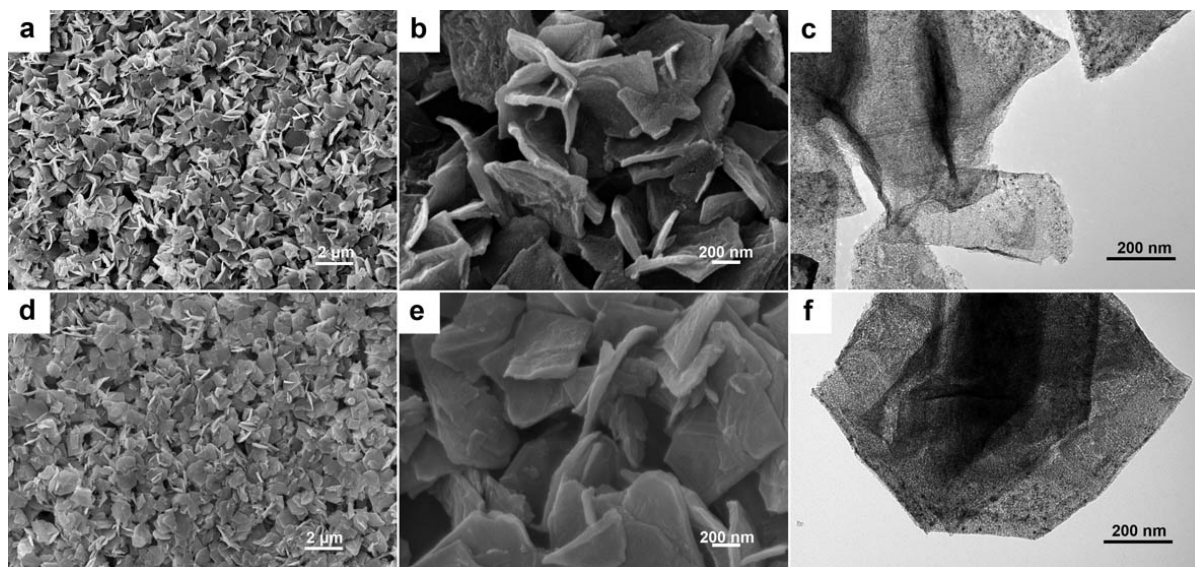


Figure S16. FESEM and TEM images of as-prepared NiFe-O (a-c) and S-NiFe-O (d-f).

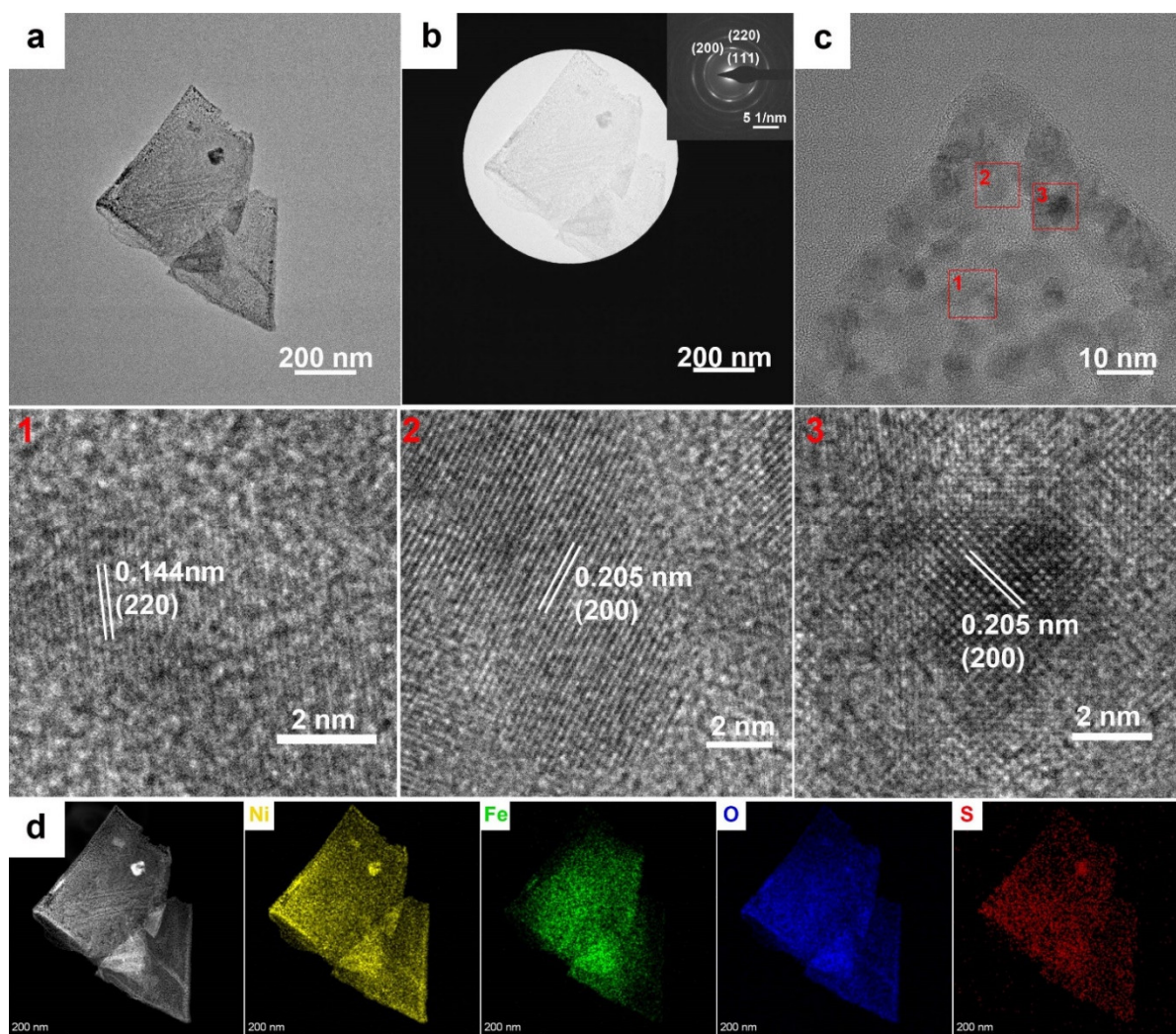


Figure S17. (a-c) HR-TEM images of as-prepared S-NiFe-O (the inset in **Figure S17b** shows the corresponding SAED pattern). (d) HAADF-STEM image and corresponding STEM-EDX element mappings.

PXRD patterns (**Figure S15**) demonstrate that the as-prepared NiFe-O and S-NiFe-O exhibit a well-defined rock salt structure without the presence of impurities. FESEM and TEM images (**Figure S16**) reveal similar nanosheet morphologies for the prepared NiFe-O and S-NiFe-O samples. The SAED pattern of S-NiFe-O (**Figure S17b**) was further recorded and exhibits three well-defined diffraction rings. These peaks can be assigned to the main exposed crystal planes (111), (211), and (301) of NiO (PDF No. 47-1049), respectively. HR-TEM images in **Figure S17c** display the characteristic lattice fringes of ~ 0.144 nm and 0.205 nm, corresponding to the exposed (220) and (200) planes, respectively. STEM-EDX element mappings further demonstrate that Ni, Fe, O, and S elements are homogeneously distributed in the selected S-NiFe-O nanosheet.

4. *Ex situ* XAS, EPR, and XPS characterizations

4.1 Ni *K*-edge EXAFS spectra of O_d-R-NiFe-CPs, S-R-NiFe-CPs, NiFe-O, and S-NiFe-O vs. references

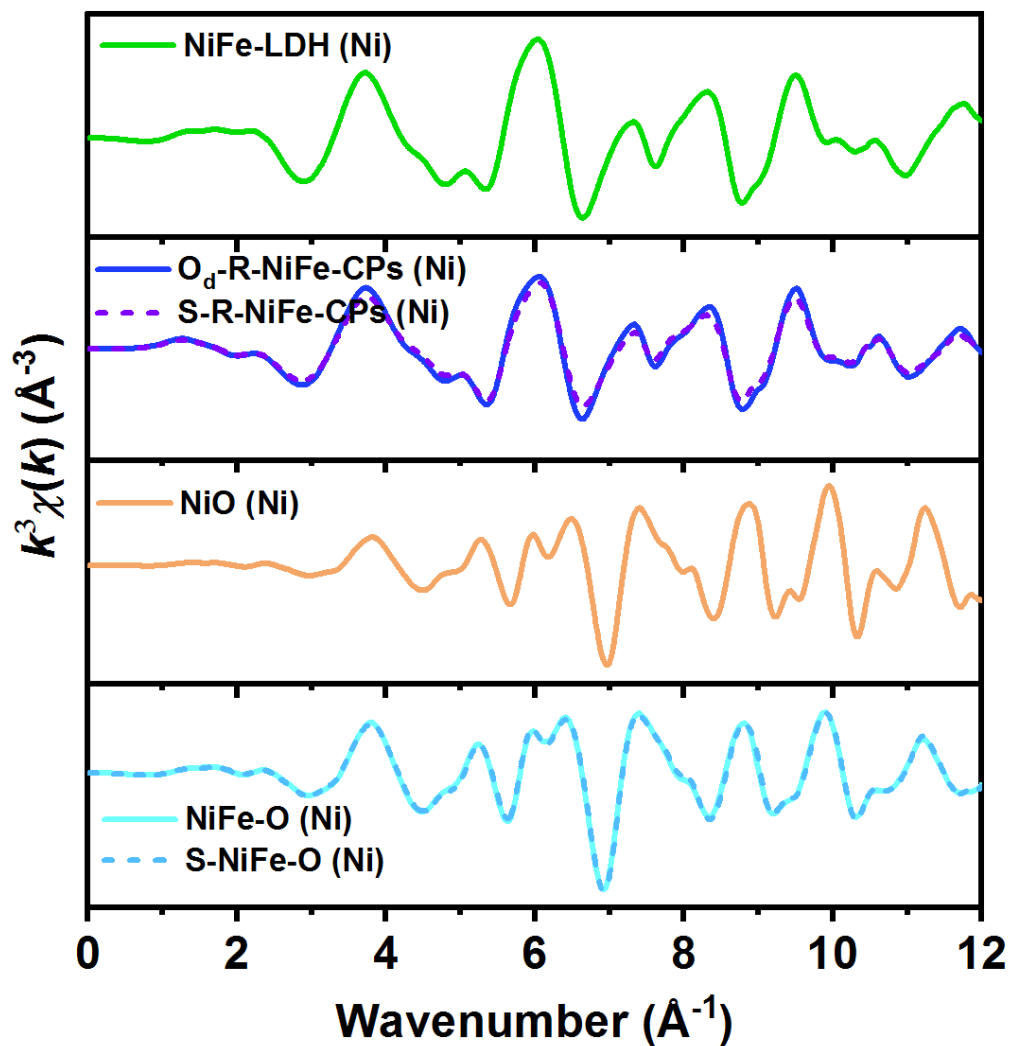


Figure S18. (a) Ni *K*-edge EXAFS spectra of as-synthesized samples vs. references.

4.2 Fe *K*-edge XAS data of O_d-R-NiFe-CPs, S-R-NiFe-CPs, NiFe-O, and S-NiFe-O

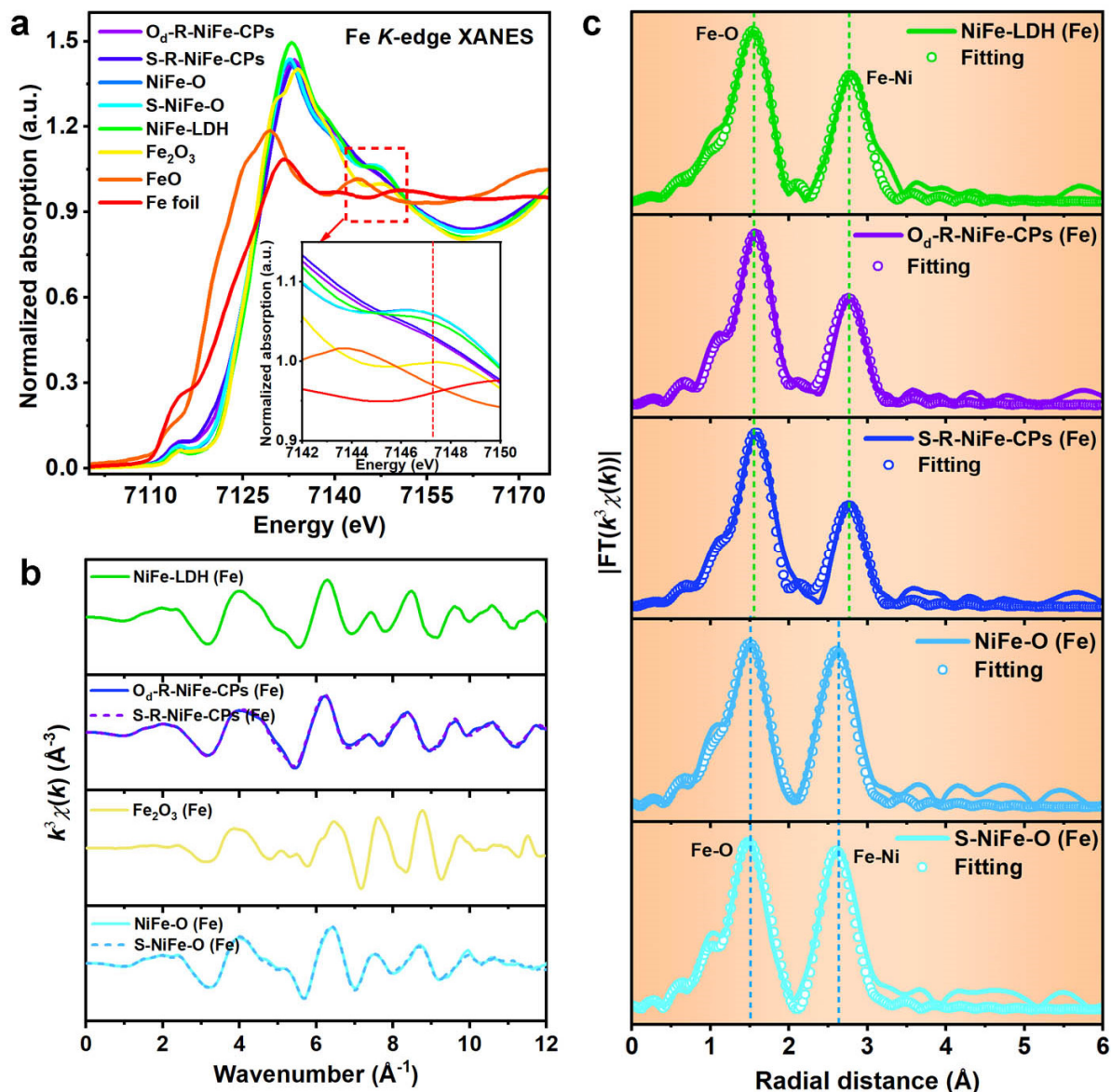


Figure S19. (a) Fe *K*-edge XANES spectra of as-synthesized samples vs. references. (b) Fe *K*-edge EXAFS spectra of as-synthesized samples vs. references. (c) Fitting of the Fe *K*-edge FT-EXAFS spectra of as-synthesized samples vs. references.

The investigations of Fe *K*-edge XAS data demonstrate that the as-prepared S-R-NiFe-CPs featured similar XANES and EXAFS spectra compared to O_d-R-NiFe-CPs (**Figure S19a,b**). Moreover, the fitting results of the FT-EXAFS spectra of O_d-R-NiFe-CPs and S-R-NiFe-CPs reveal that the incorporation of S atoms does not alter the local coordination environment of Fe centers (**Table S4**). The Fe *K*-edge XAS data also provided analogous evidence for the similar local electronic structure and coordination environment of Fe centers in NiFe-O and S-NiFe-O. All of the above investigations imply that the S atoms mainly refill the oxygen deficiencies around the Ni sites.

4.3 XAS characterization of S-R-NiFe-CPs synthesized with different amounts of TAA

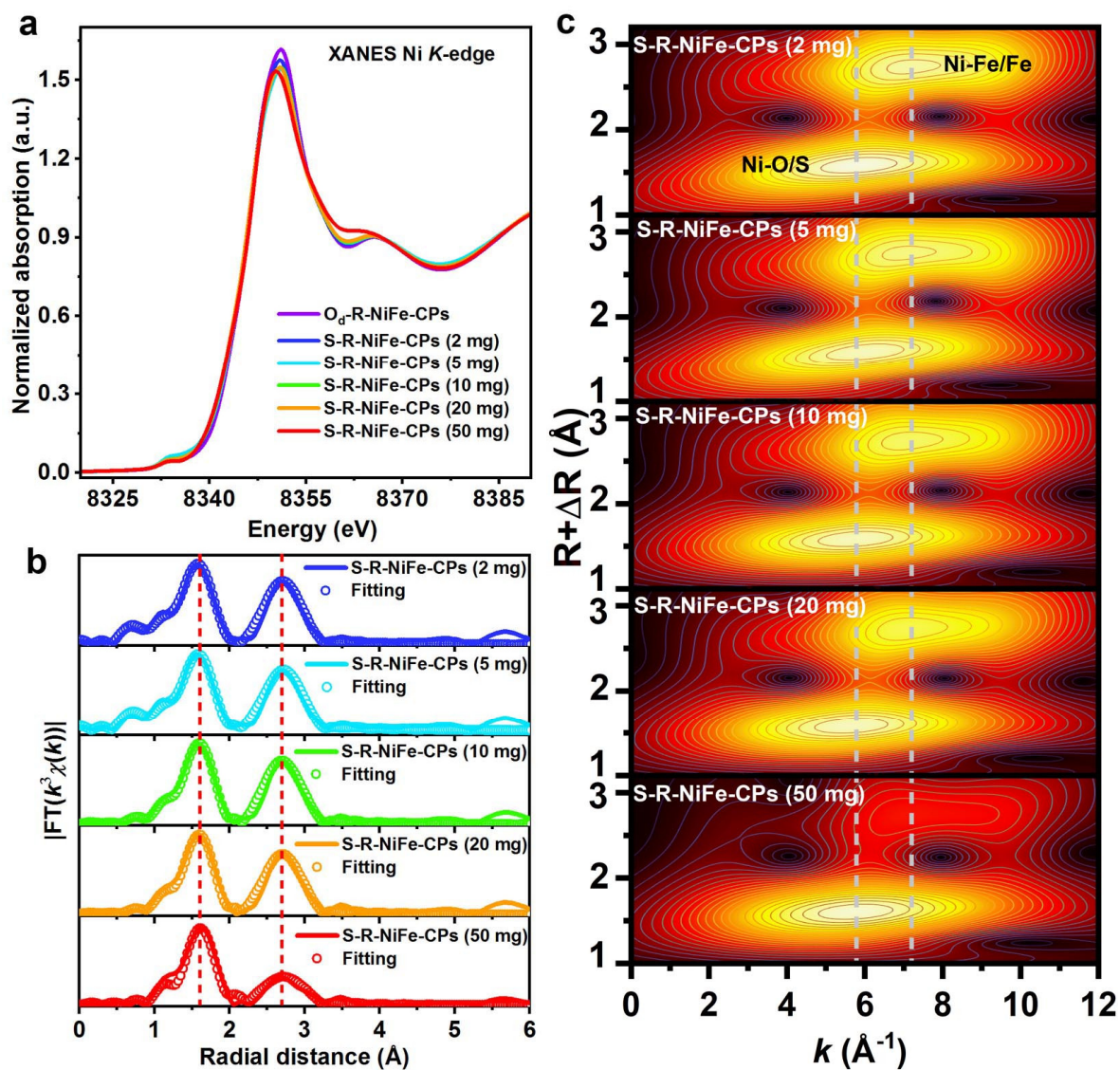


Figure S20. (a) Ni K-edge XANES spectra of O_d-R-NiFe-CPs and S-R-NiFe-CPs obtained with different amounts of TAA. (b, c) Ni K-edge FT-EXAFS spectra and WT contour profiles of S-R-NiFe-CPs obtained with different amounts of TAA.

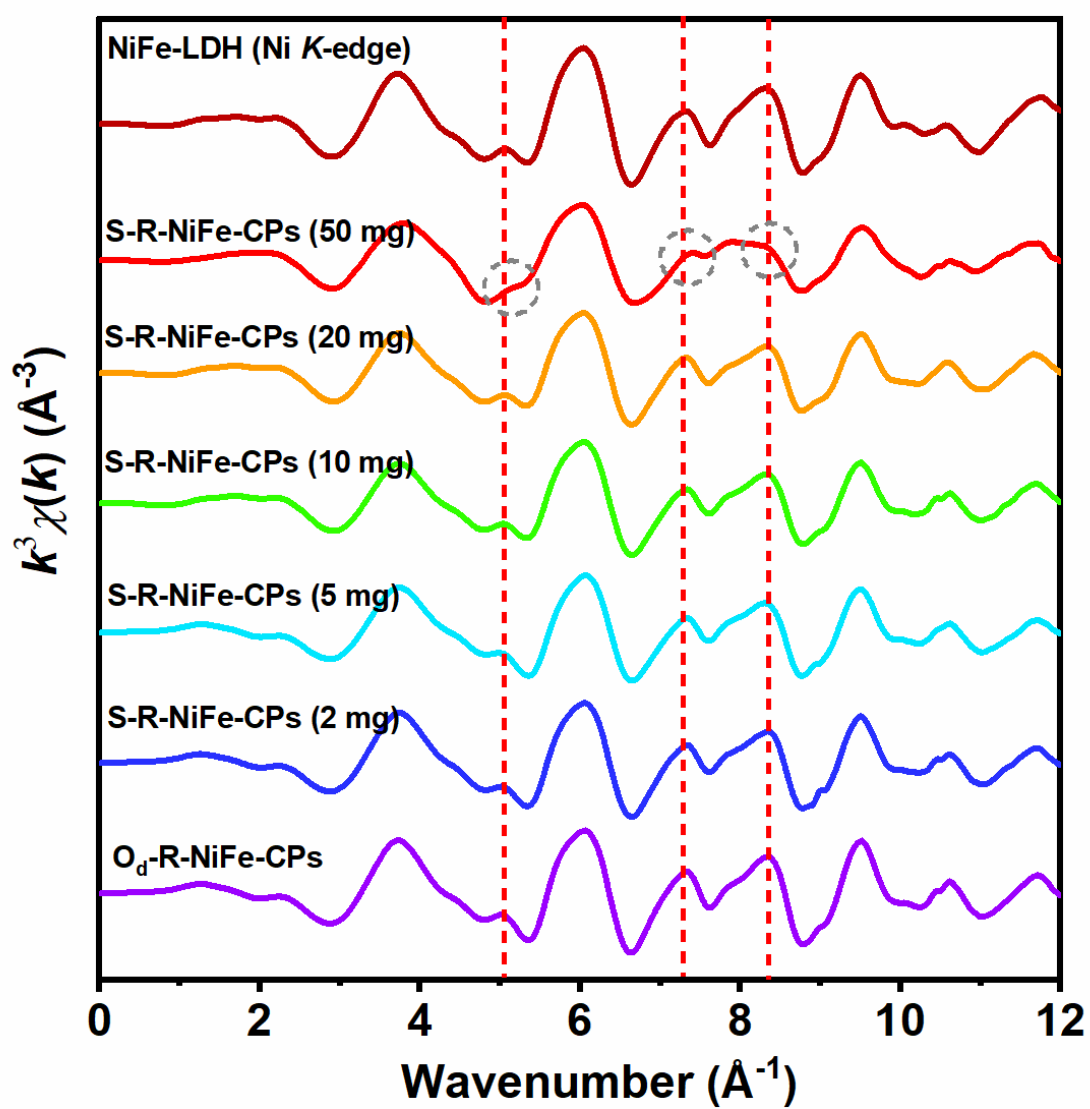


Figure S21. Ni K-edge EXAFS spectra of O_d -R-NiFe-CPs and S-R-NiFe-CPs obtained with different amounts of TAA vs. reference NiFe-LDH.

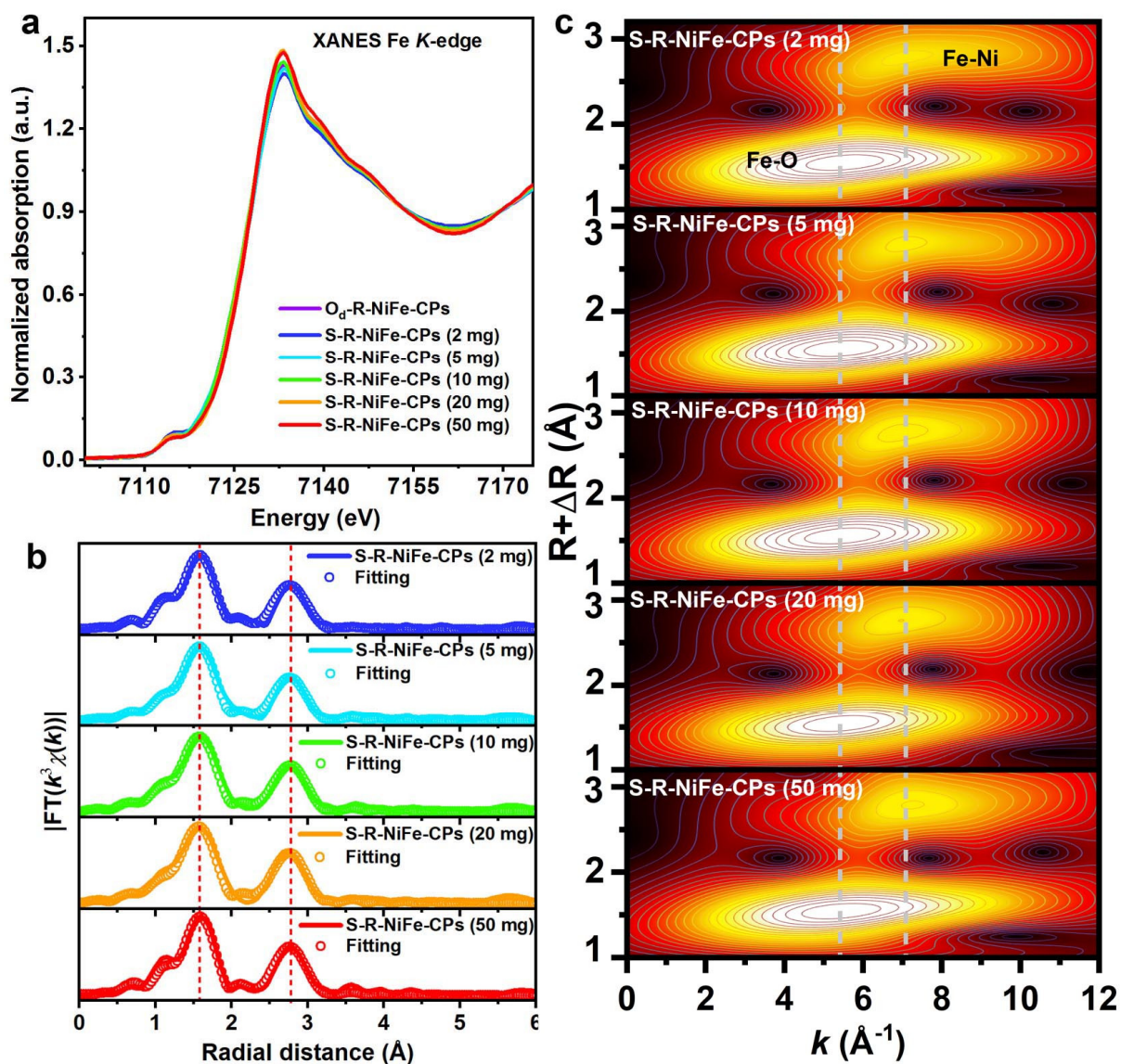


Figure S22. (a) Fe *K*-edge XANES spectra of O_d-R-NiFe-CPs and S-R-NiFe-CPs obtained with different amounts of TAA. (b, c) Fe *K*-edge FT-EXAFS spectra and WT contour profiles of S-R-NiFe-CPs obtained with different amounts of TAA.

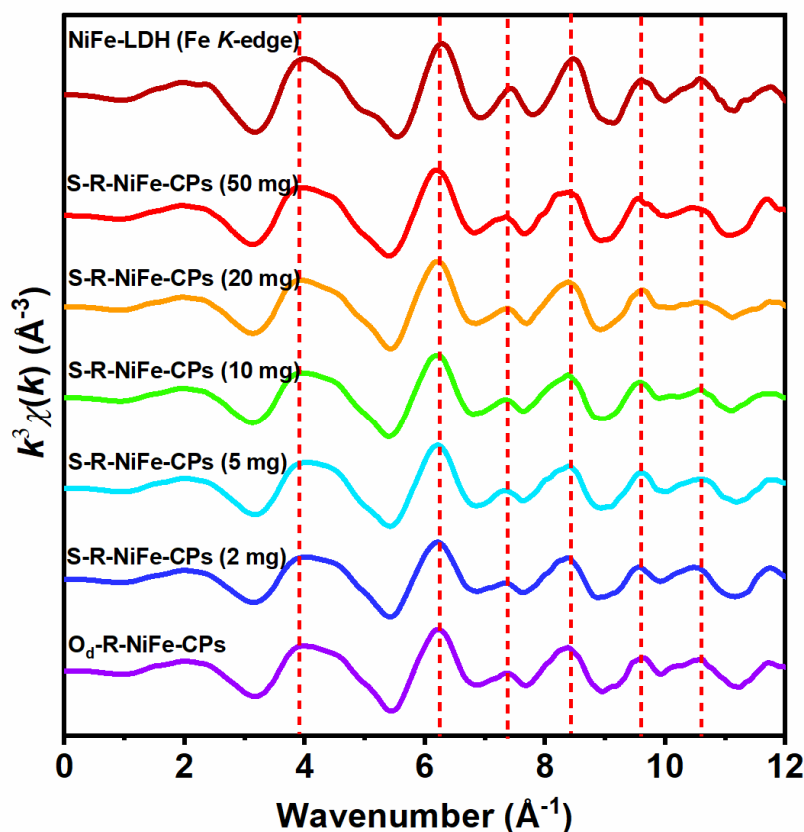


Figure S23. Fe *K*-edge EXAFS spectra of O_d-R-NiFe-CPs and S-R-NiFe-CPs obtained with different amounts of TAA vs. reference NiFe-LDH.

Investigation of the Ni *K*-edge FT-EXAFS spectra (**Figures S20-S21**) of S-R-NiFe-CPs (2 ~ 50 mg) demonstrates an obvious change in the local coordination environment of Ni centers. In detail, as shown in **Figure S20c**, as the amount of S atoms increases, the intensity maximum at around $k=7.2 \text{ \AA}^{-1}$ (backscattering of Ni-Ni/Fe pairs) in the wavelet transform (WT) of the EXAFS spectra of S-R-NiFe-CPs (2 ~ 50 mg) shows a decreasing trend towards weaker signals. According to the results of fitting the FT-EXAFS spectra (**Figure S20b and Table S3**), both the CN_{Ni-O} and $CN_{Ni-Ni/Fe}$ values remain almost unchanged when the amounts of S atoms are lower than 10 mg. For the samples with 20 and 50 mg, both the CN_{Ni-O} and $CN_{Ni-Ni/Fe}$ values decrease obviously compared with those of O_d-R-NiFe-CPs. While the calculated CN_{Ni-S} values show an increasing trend implying that the local coordination environments of Ni centers are strongly altered by sulfur atom incorporation, the variations in the coordination environment of Fe centers are negligible (**Figures S22-S23**).

4.4 EPR characterization of as-investigated catalysts

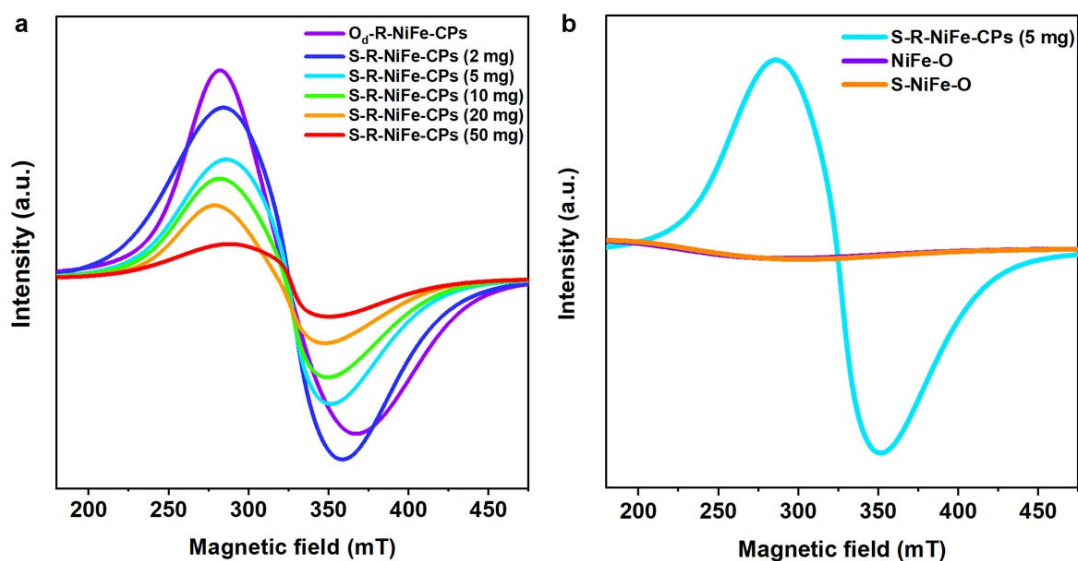


Figure S24. Room temperature EPR spectra of as-prepared samples.

We recorded EPR spectra to elucidate the influence of sulfidation on the oxygen deficiencies in the as-prepared samples. As shown in **Figure S24a**, the EPR spectrum of O_d -R-NiFe-CPs shows an isotropic peak with the strongest intensity, suggesting the presence of abundant unpaired electrons. In this study, these unpaired electrons are predominantly arising from the formation of oxygen deficiencies (**Tables S3-S4**). As the amounts of TAA were increased from 2 mg to 50 mg, the intensity of the isotropic peak of S-R-NiFe-CPs exhibits a continuously decreasing trend, reflecting the lower amounts of unpaired electrons. This provides further support that the introduced S atoms first refill the oxygen deficiencies, in line with the above XAS results (**Figures S19-S23**). For comparison, the EPR spectra of NiFe-O and S-NiFe-O were also recorded. According to the obtained results in **Figure S24b**, both NiFe-O and S-NiFe-O were not sensitive towards EPR measurements, which further confirmed that the alterations of EPR signals in **Figure S24b** originate from sulfur atom incorporation into the oxygen-deficient sites.

4.5 XPS characterization of as-investigated catalysts

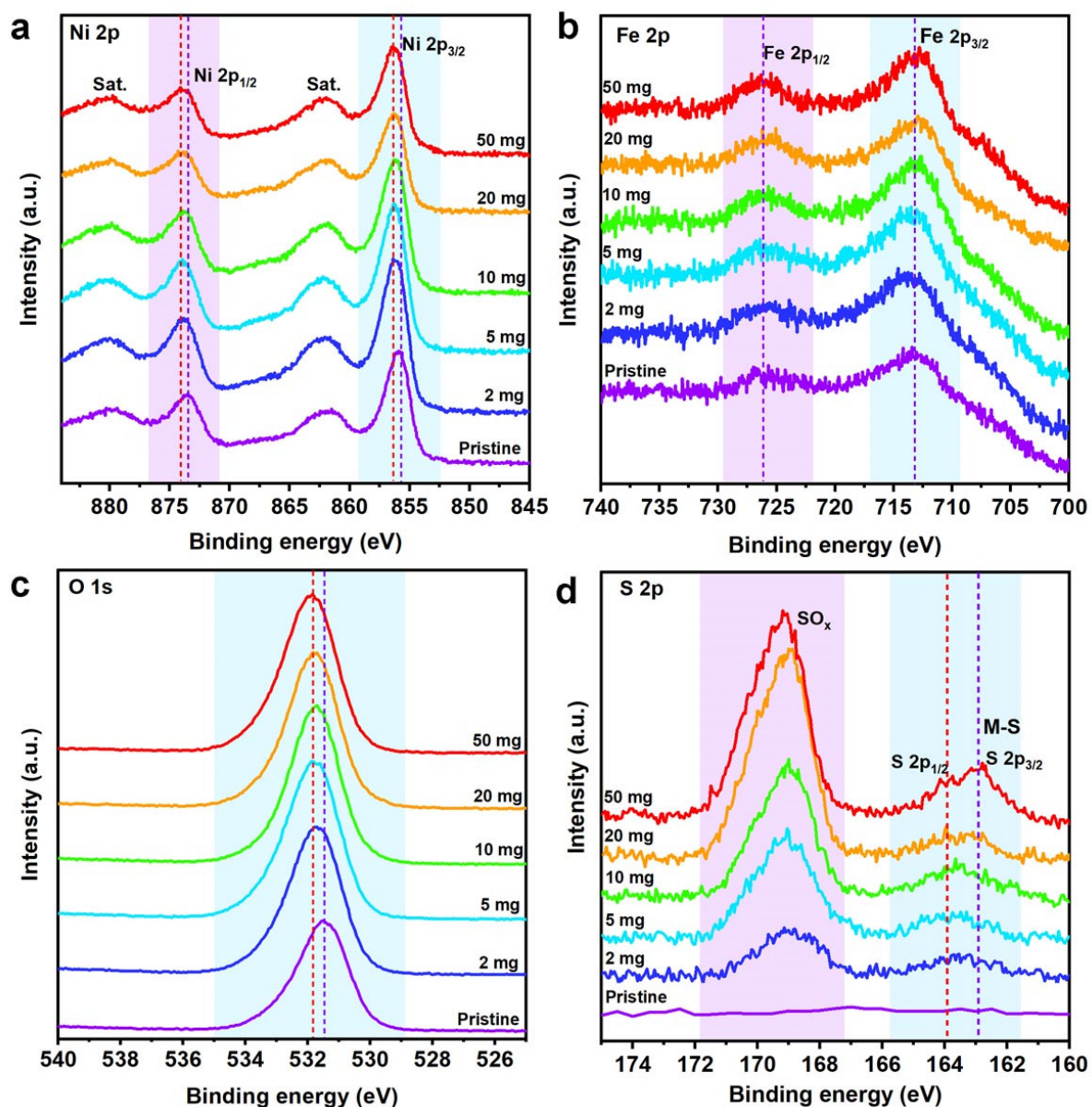


Figure S25. High-resolution XPS spectra of O_d-R-NiFe-CPs (pristine) and S-R-NiFe-CPs (2, 5, 10, 20, and 50 mg): (a) Ni 2p; (b) Fe 2p; (c) O 1s; (d) S 2p.

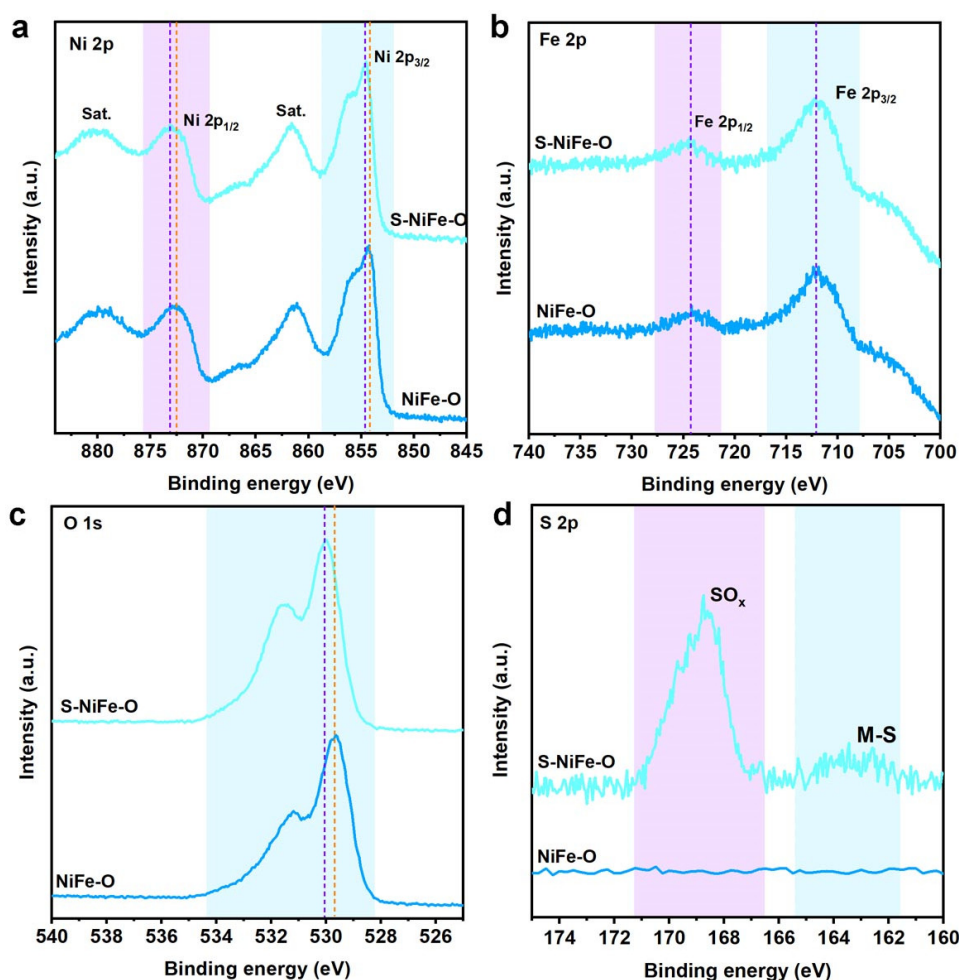


Figure S26. High-resolution XPS spectra of NiFe-O and S-NiFe-O: (a) Ni 2p; (b) Fe 2p; (c) O 1s; (d) S 2p.

The surface electronic structures of the synthesized samples were examined by the deconvoluted high-resolution Ni 2p, Fe2p, O1s, and S 2p (**Figures S25-S26**) XPS spectra. Noteworthy, the binding energy positions of Ni 2p and O 1s (**Figure S25a,c**) in S-R-NiFe-CPs exhibit a slight positive shift compared with that of O_d-R-NiFe-CPs. However, concerning the binding energy positions in the Fe 2p regions, all the investigated samples remained identical. Furthermore, the S 2p XPS spectra of the investigated samples were also investigated and showed an increasing tendency of peak intensity for S 2p_{1/2} and S2p_{3/2}, indicating the increased numbers of M-S bonds. For comparison, the XPS spectra of NiFe-O and S-NiFe-O were also recorded (**Figure S26**). The XPS results of NiFe-O and S-NiFe-O demonstrated similar evidence for the positive energy shift observed from Ni 2p and O 1s compared with that of O_d-R-NiFe-CPs and S-R-NiFe-CPs. Combining these XPS results together with the above EPR results at hand (**Figures S24-S26**), we conclude that only the surface electronic structures of Ni and O centers in O_d-R-NiFe-CPs were altered after incorporation of sulfur atoms. These results further suggest that the sulfidation reaction mechanism follows the proposed reaction pathways of S1 and S4 in **Figure S1**. In detail, for low amounts of TAA, the incorporated S atoms mainly refilled the oxygen deficiencies during the sulfidation process. When a high amount of TAA was applied, part of the S atoms can still follow the proposed reaction pathway of S1 to refill the oxygen deficiencies (**Figure S1**). However, the excess sulfur atoms likely replace partial oxygen atoms around the Ni site to construct the proposed structure S4 as described in **Figure S1**.

5. Electrochemical OER performance

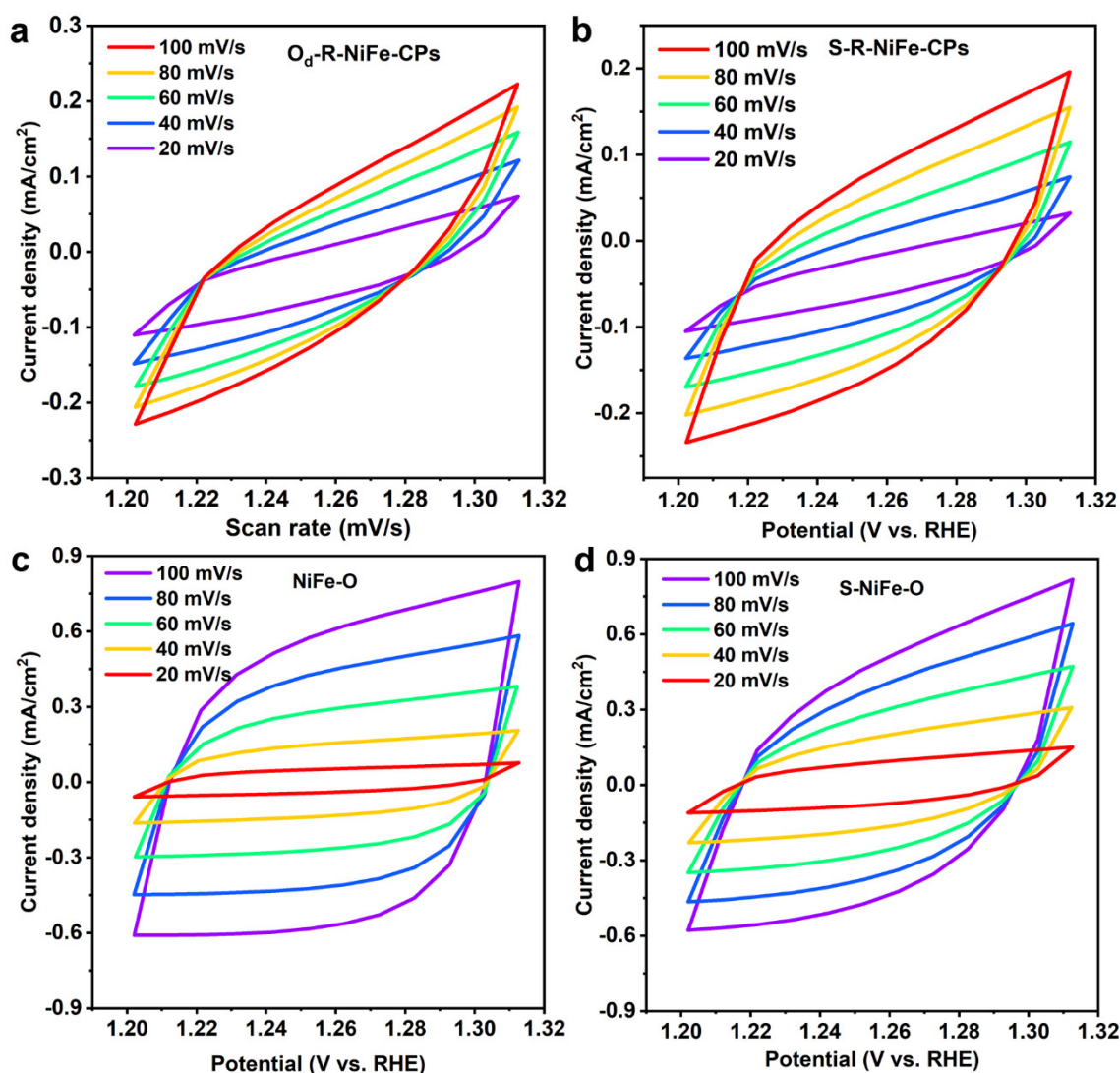


Figure S27. CV curves of O_d-R-NiFe-CPs (a), S-R-NiFe-CPs (b), NiFe-O (c), and S-NiFe-O (d) in 1.0 M KOH.

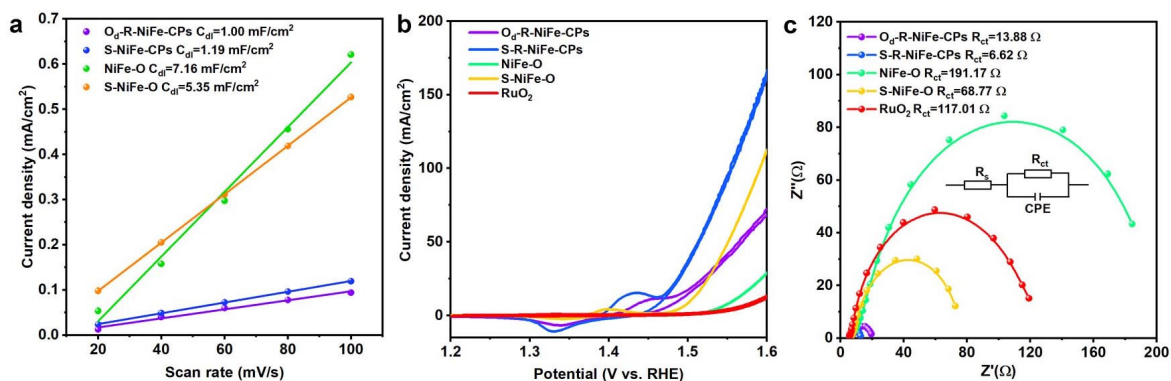


Figure S28. (a) Double-layer capacitance (C_{dl}) of as-prepared catalysts. (b, c) CV curves of as-prepared catalysts vs. reference RuO₂ before and after 90%-iR corrections. (d) Nyquist plots of as-prepared catalysts vs. reference RuO₂ (at an overpotential of 250 mV).

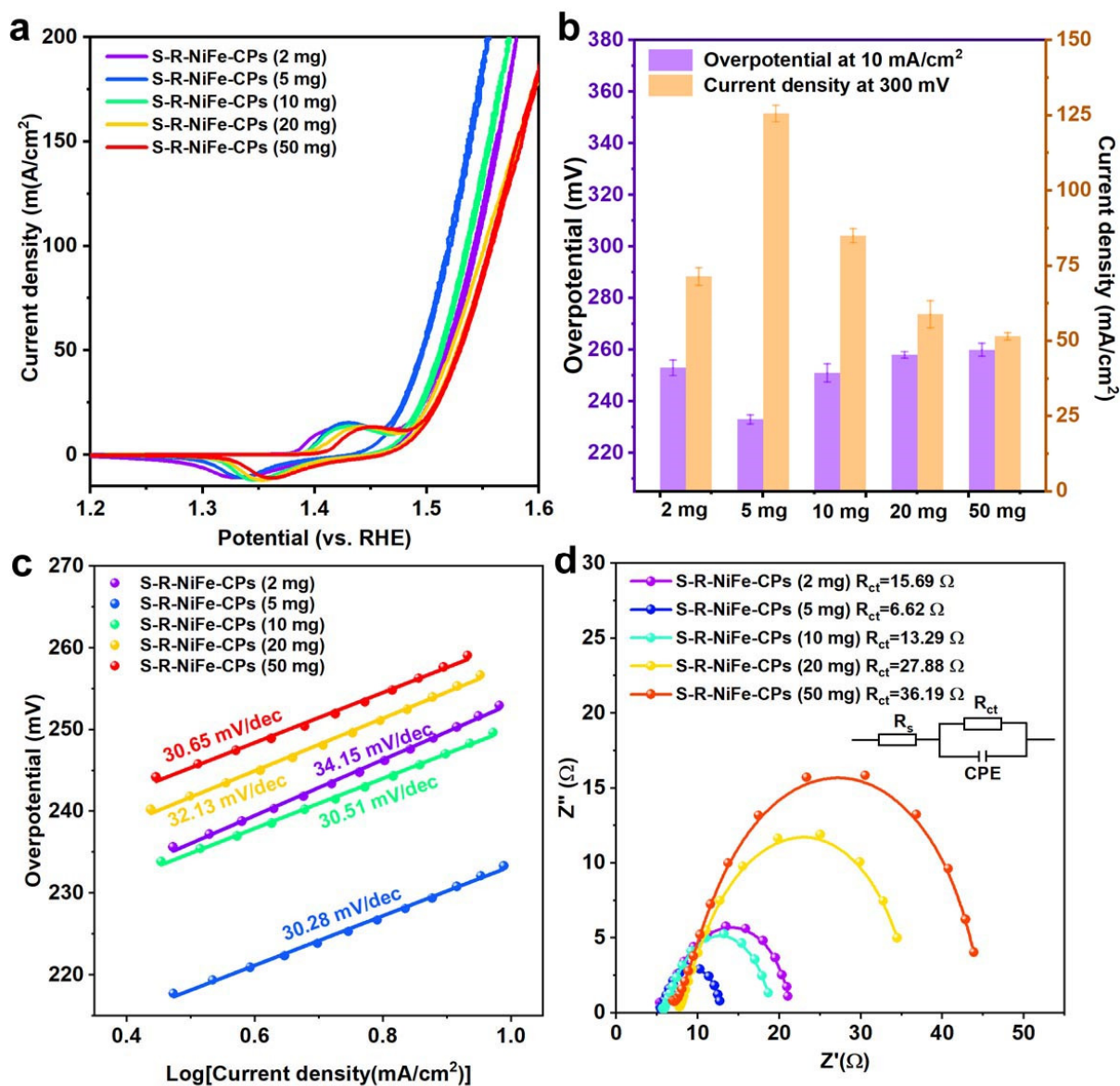


Figure S29. Electrocatalytic performance of S-R-NiFe-CPs obtained with different amounts of TAA in 1.0 M KOH for OER. (a) CV curves. (b) Comparison of overpotentials at 10 mA/cm² and current densities at an overpotential of 300 mV. (c) Tafel plots. (d) Nyquist plots (at an overpotential of 250 mV).

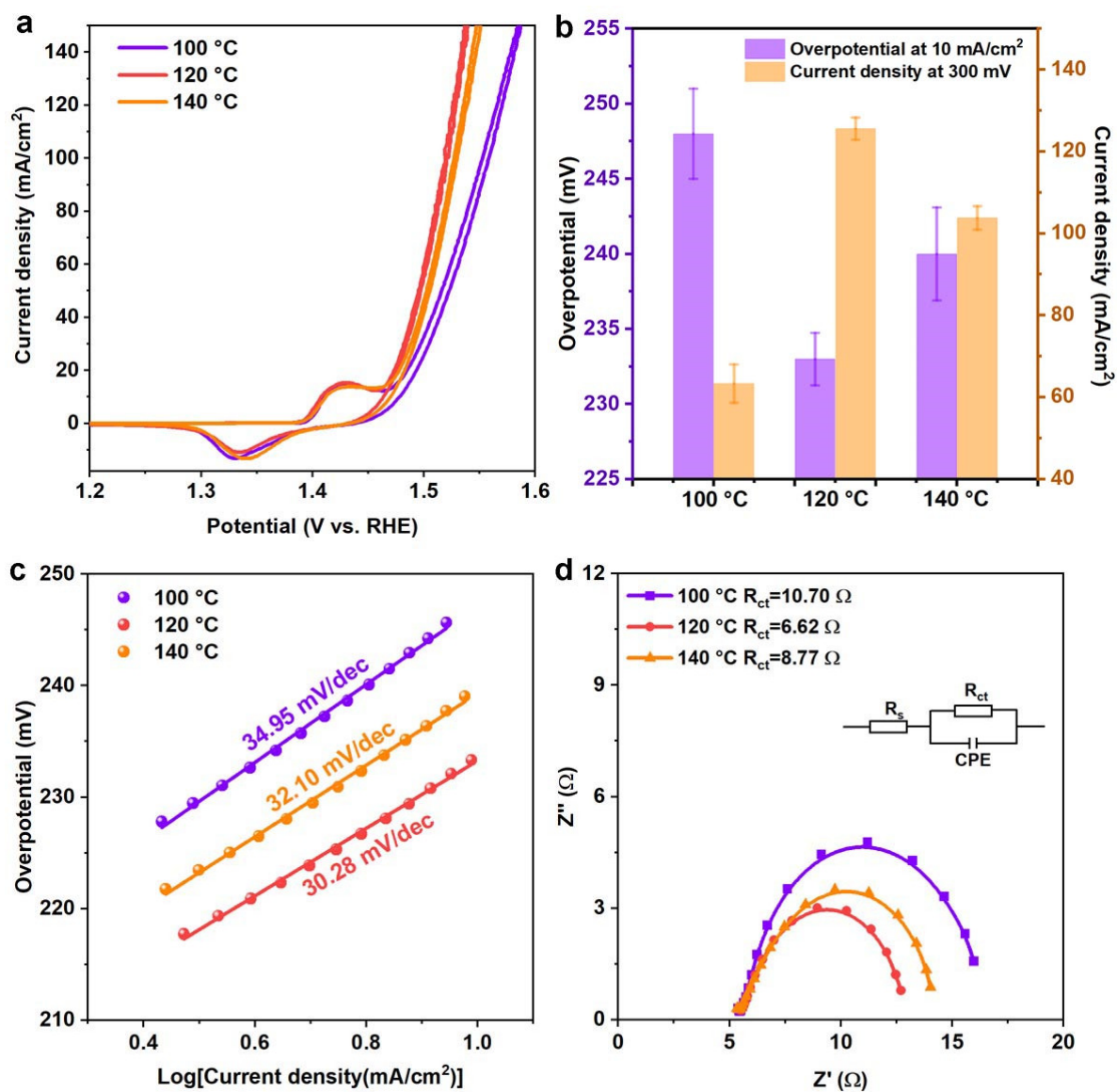


Figure S30. Electrocatalytic performance of S-R-NiFe-CPs at different reaction temperatures in 1.0 M KOH for OER. (a) CV curves. (b) Comparison of overpotentials at 10 mA/cm² and current densities at an overpotential of 300 mV. (c) Tafel plots. (d) Nyquist plots (at an overpotential of 250 mV).

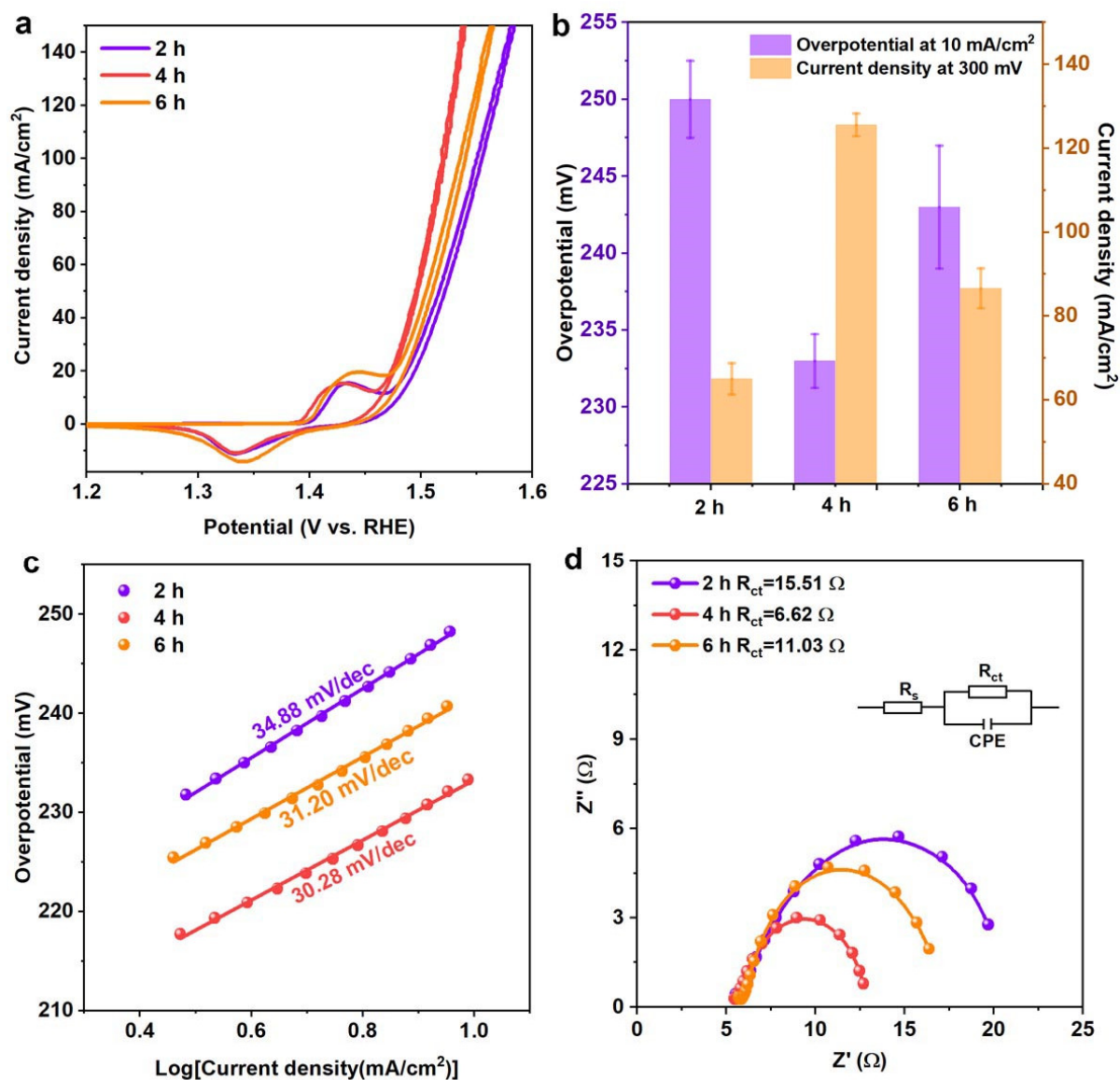


Figure S31. Electrocatalytic performance of S-R-NiFe-CPs after different reaction times in 1.0 M KOH for OER. (a) CV curves. (b) Comparison of overpotential at $10 \text{ mA}/\text{cm}^2$ and current densities at an overpotential of 300 mV. (c) Tafel plots. (d) Nyquist plots (at an overpotential of 250 mV).

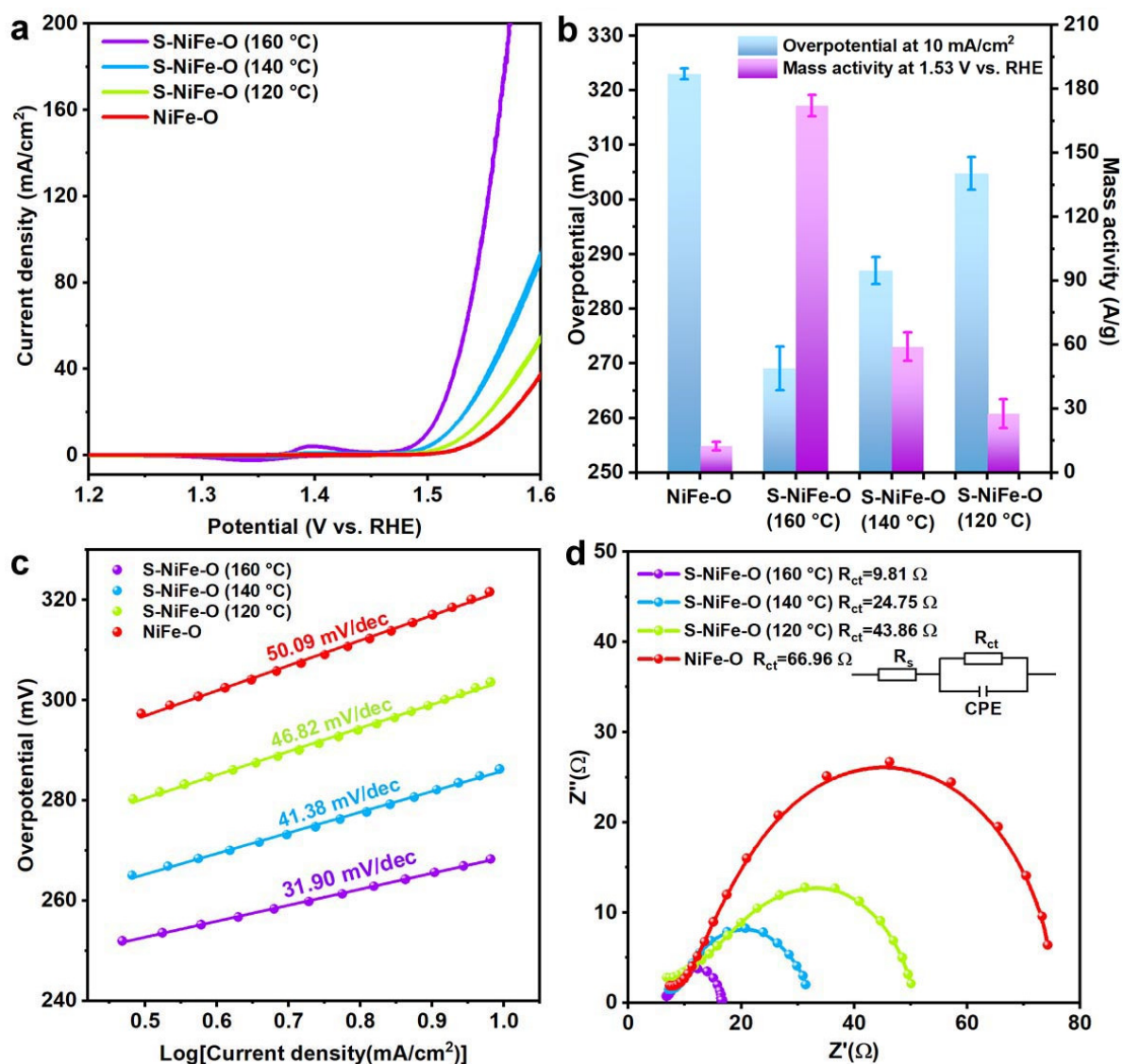


Figure S32. Electrocatalytic performance of NiFe-O and S-NiFe-O generated at different reaction temperatures in 1.0 M KOH for OER. (a) CV curves. (b) Comparison of overpotential at 10 mA/cm² and current densities (at an overpotential of 300 mV). (c) Tafel plots. (d) Nyquist plots (at an overpotential of 300 mV).

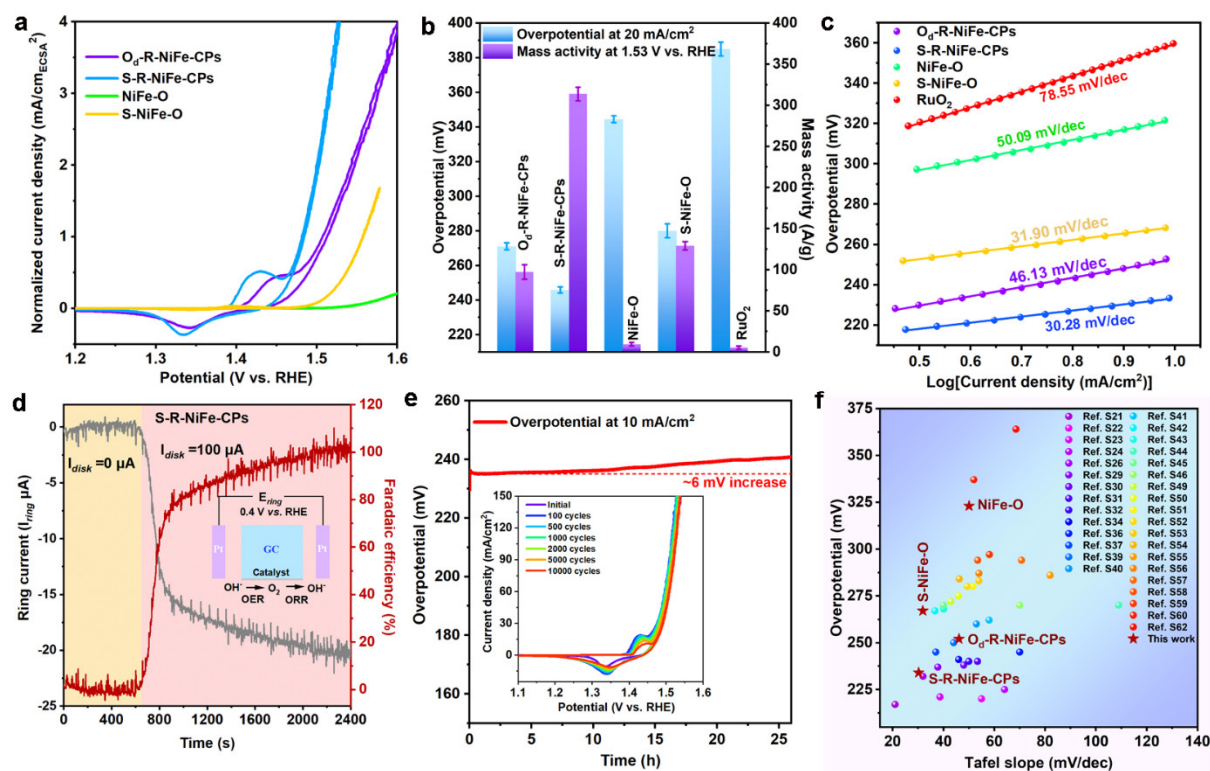


Figure S33. (a) Normalized CV curves (current normalized by ECSA) of O_d-R-NiFe-CPs, S-R-NiFe-CPs, NiFe-O, and S-NiFe-O. (b) Comparison of overpotentials at 20 mA/cm_{geometric}² and mass activities at 1.53 V vs. RHE. (c) Tafel plots of the as-prepared catalysts and reference RuO₂. (d) Faradaic efficiency of S-R-NiFe-CPs tested in Ar-saturated 1.0 M KOH (the inset represents the schematic diagram of RRDE technique). (e) Chronopotentiometry measurements of S-R-NiFe-CPs. (f) Comparison of overpotentials at a current density of 10 mA/cm² and Tafel slope values of the as-prepared catalysts with recent representative studies on NiFe-based electrocatalysts.

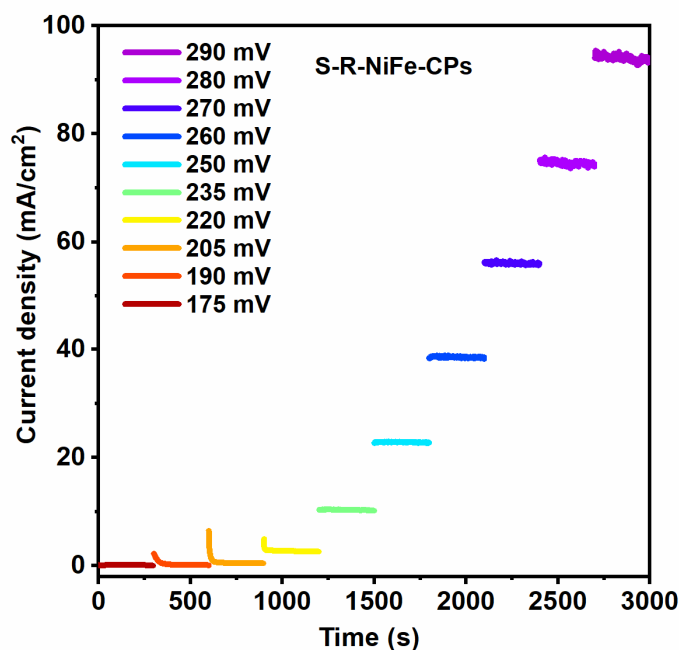


Figure S34. (a) Multi-potential-step chronoamperometric test of S-R-NiFe-CPs with overpotentials from 175 to 290 mV.

Supplementary Discussion II: Electrocatalytic OER performance

The OER activities of the as-synthesized catalysts were evaluated with a standard three-electrode system in 1.0 M KOH vs. commercial RuO₂ as a reference. As shown in **Figures S27-S28**, the CV curves of the investigated catalysts were first corrected with a 90% iR compensation. Then, the currents were normalized to the electrochemical surface area (ECSA) to reflect the intrinsic catalytic activity. To optimize the OER activity, the influence of the different synthetic parameters (e.g. TAA amounts, reaction temperature, and reaction times) on the OER activity was explored. The results (**Figures S29-S31**) indicate that the as-prepared S-R-NiFe-CPs synthesized with 5 mg of TAA at 120 °C for 4 h exhibit the best OER activity. For the control experiments with NiFe-O and S-NiFe-O (**Figure S32**), the best OER activity was observed for S-NiFe-O samples prepared with 5 mg of TAA at 160 °C for 4 h. **Figure 2c** and **Figure S28b** show the CV curves of the investigated catalysts before and after normalization to ECSA. To attain a specific current density of 1 mA/cm_{ECSA}² and a geometric current density of 10 mA/cm_{geo}², the as-prepared S-R-NiFe-CPs exhibit the lowest overpotentials of 254 mV and 234 mV, respectively. This outperforms the OER activity of O_d-R-NiFe-CPs (283 mV and 254 mV), S-NiFe-O (327 mV and 269 mV), and NiFe-O (320 mV and 421 mV at 0.5 mA/cm_{ECSA}²). **Figure 33b** further compares the overpotentials at the geometric current density of 20 mA/cm_{geo}² and the mass activities at an overpotential of 300 mV. As expected, S-R-NiFe-CPs display the lowest overpotential of 245 mV and the highest mass activity of 314 A/g, being better than O_d-R-NiFe-CPs (271 mV and 97 A/g), S-NiFe-O (280 mV and 129 A/g), NiFe-O (345 mV and 9 A/g), and commercial RuO₂ (385 mV and 5 A/g).

Tafel slope values of the investigated catalysts were further calculated based on the iR corrected CV curves. As illustrated in **Figure 33c**, the Tafel slope values follow the order S-R-NiFe-CPs (30.28 mV/dec) < S-NiFe-O (31.90 mV/dec) < O_d-R-NiFe-CPs (46.13 mV/dec) < NiFe-O (50.09 mV/dec) < commercial RuO₂ (78.55 mV/dec). It should be noted that both S-R-NiFe-CPs and S-NiFe-O show a smaller Tafel slope value compared with O_d-R-NiFe-CPs and NiFe-O. This strongly suggests that engineering of partial S substitution can optimize the intrinsic OER kinetics of the investigated catalysts, thereby resulting in an improved OER activity. Furthermore, electrochemical impedance spectroscopy (EIS) tests (**Figure S28c**) were performed at an overpotential of 250 mV, which demonstrates the favorable charge transfer properties of S-R-NiFe-CPs. This further highlights the benefits of employing sulfur atom modification towards high OER performance. To confirm that the recorded currents primarily originate from the OER, the Faradaic efficiency was determined using the rotating-ring disk electrode (RRDE) technique. Our measurement results (**Figure 33d**) indicate nearly 100% of Faradaic efficiency for the best-performing S-R-NiFe-CPs, thus verifying its four-electron transfer characteristics during the OER process ($4\text{OH}^- \rightarrow \text{O}_2 + 2\text{H}_2\text{O} + 4\text{e}^-$).

The electrochemical stability was assessed through both CV cycling and chronopotentiometry methods. As shown in **Figure 33e**, the as-prepared S-R-NiFe-CPs can maintain its initial catalytic activity over 25 h with only slight potential variations (~6 mV increase). It should be emphasized that this slight activity decline is primarily due to the detachment of the catalyst layers from the electrode. This is a common issue for the GC electrode under high rotation speed for long-time measurements (>12 h).^[16,17] The CV curve of S-R-NiFe-CPs can be well retained after 10000 CVs (inset in **Figure 33e**). Furthermore, we conducted the multi-potential step chronoamperometry test to examine the electrochemical

stability of S-R-NiFe-CPs at different current densities. Our results (**Figure S34**) corroborated that the as-prepared S-R-NiFe-CPs well maintained the high catalytic activity during the test, further revealing their good electrochemical stability towards application conditions for high-performance OER catalysts. The excellent OER activity and superior electrochemical stability of S-R-NiFe-CPs outperform most recently studied NiFe-based OER electrocatalysts (**Figure 33f**).

6. Post-catalytic characterization

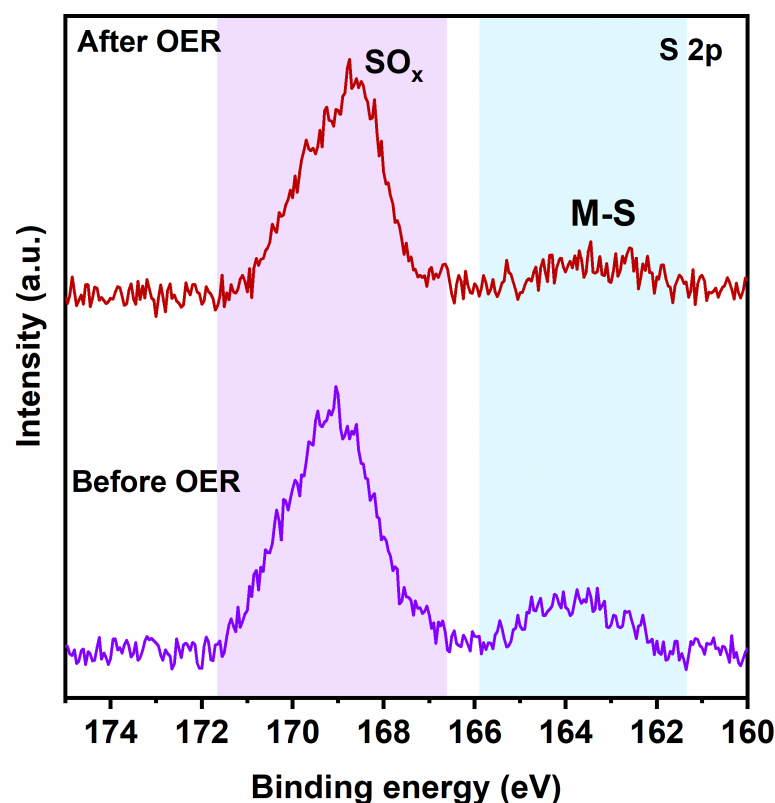


Figure S35. High-resolution S 2p XP spectra of S-R-NiFe-CPs before and after OER.

We performed XPS characterizations to investigate the structural stability of S-R-NiFe-CPs after the OER process. As shown in **Figure S35**, the post-catalytic sample displays an identical high-resolution S 2p XP spectrum compared with that of the pristine sample. This demonstrates that the local electronic structures of S-R-NiFe-CPs can be maintained well during the OER process. To get further insights into the dynamics of the local coordination environment during the OER process, *operando* monitoring experiments are essential.

7. OER activities of O_d-R-NiFe-CPs with different concentrations of K₂SO₄

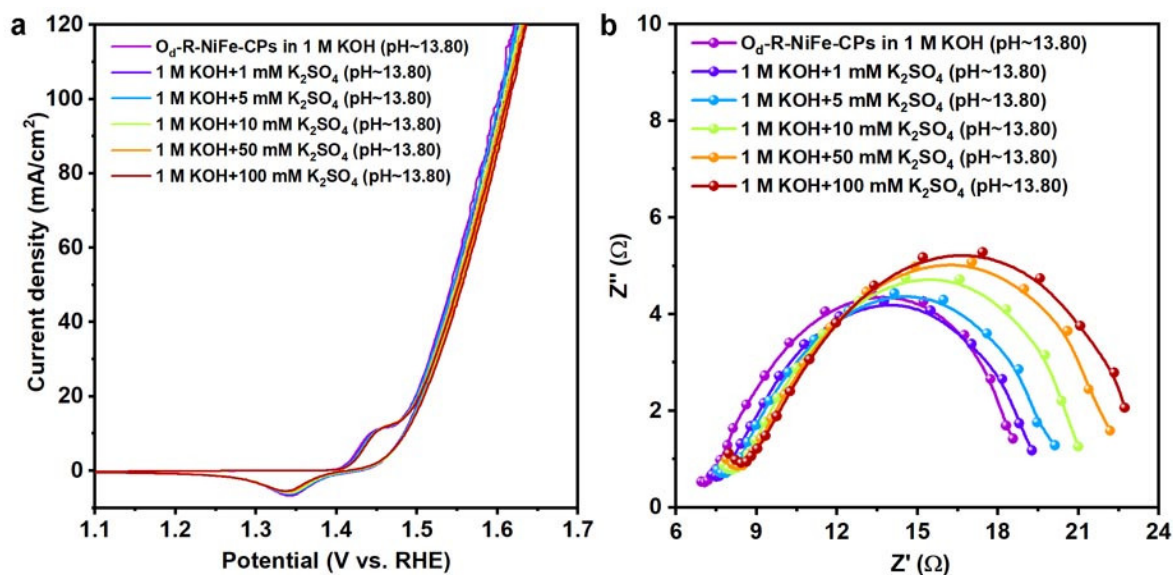


Figure S36. Electrocatalytic performance of O_d-R-NiFe-CPs performed in 1.0 M KOH with different concentrations of K₂SO₄ for OER. (a) CV curves. (b) Nyquist plots (at an overpotential of 250 mV).

Recent related works indicated that surface residual chalcogens played a non-negligible role in the catalytic activities of OER electrocatalysts.^[18-20] Given the appearance of the obvious surface SO_x signals in the XPS results of S-R-NiFe-CPs (**Figure S35**), we further conducted the OER measurements with as-prepared O_d-R-NiFe-CPs in 1.0 M KOH with different concentrations of SO₄²⁻ anions. As shown in **Figure S36a**, as the concentrations of SO₄²⁻ anions were increased from 1 mM to 100 mM, O_d-R-NiFe-CPs show nearly identical CV curves. This reflects no enhancements on the OER activity of O_d-R-NiFe-CPs with the addition of SO₄²⁻ anions to the electrolyte. The Nyquist plots (**Figure S36b**) exhibit slight changes with the observations of different diameters of semicircles, which reflects the variations of the charge transfer resistances. To the best of our knowledge, these variations can most likely be ascribed to the alterations in the diffusion effects in the presence of SO₄²⁻ anions in the electrolyte.^[17-18] With these results at hand, we conclude that surface residual SO_x groups are not the key factor for the enhanced OER activity of S-R-NiFe-CPs. We assume that the surface-adsorbed oxyanions contribute to the OER activity only in some specific systems, such as catalysts with a single type of metal centers.^[18-20] In the case of OER catalysts with multiple metal centers, such as NiFe-based OER catalysts, the contribution of the surface-adsorbed oxyanions to the OER is less important compared to the true active species of high-valent Ni^{IV}-O-Fe^{IV}-moieties. To confirm such a hypothesis, future works involving surface-sensitive techniques (such as *in situ* XPS and soft XAS) are required to conduct a depth-profiling investigation of the surface behavior of catalysts during the OER.

8. *Operando* XAS characterizations

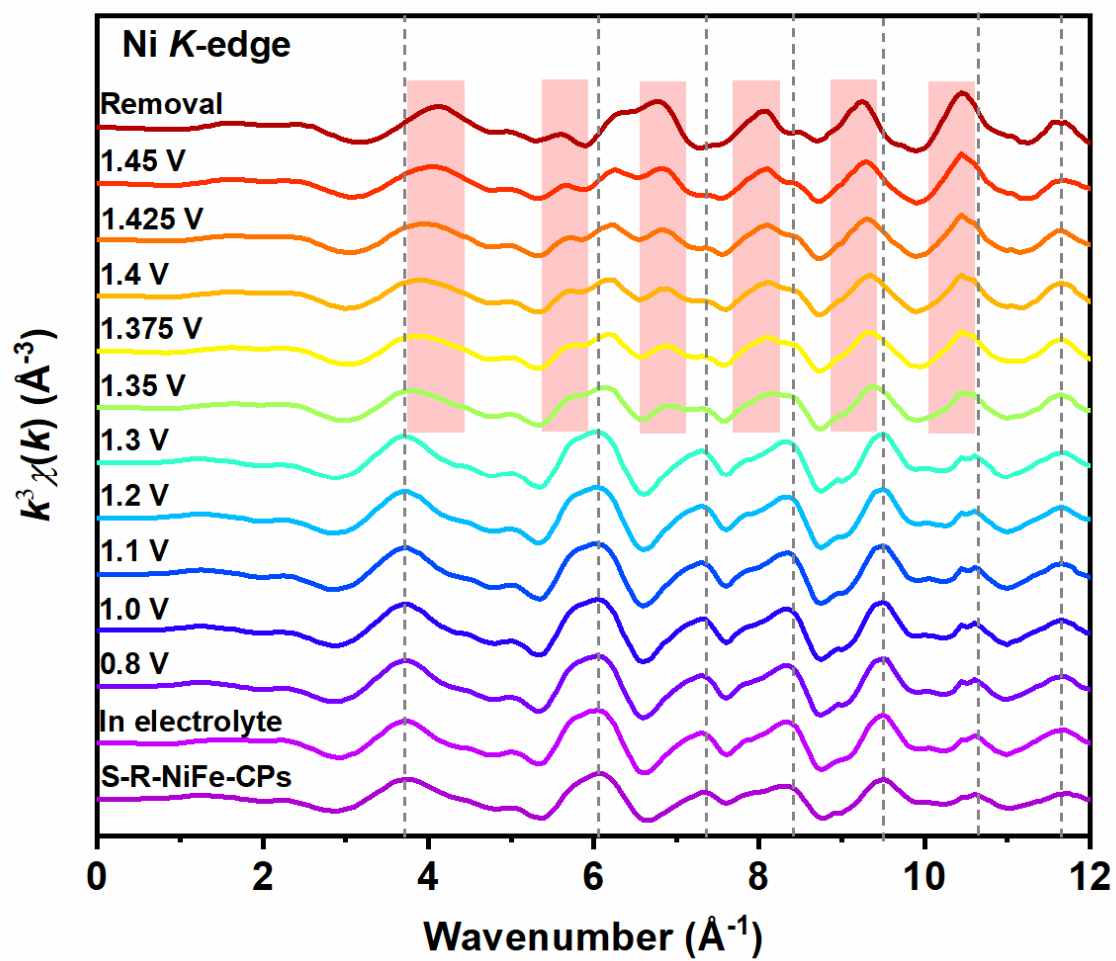


Figure S37. *Operando* Ni K-edge EXAFS spectra of S-R-NiFe-CPs recorded at different potentials (vs. RHE) in 0.1 M KOH for OER.

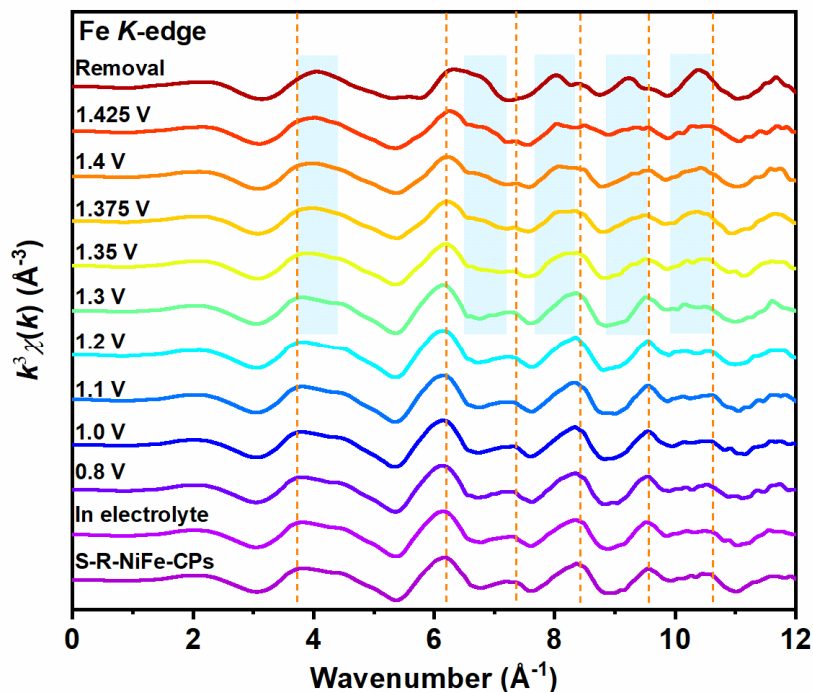


Figure S38. Operando Fe K-edge EXAFS spectra of S-R-NiFe-CPs recorded at different potentials (vs. RHE) in 0.1 M KOH for OER.

Given the low atomic ratio of Fe/Ni in S-R-NiFe-CPs, in order to improve the quality of XAS signals, the required acquisition time for the Fe K-edge XAS signals was 5 times longer than for the Ni K-edge. Moreover, the EXAFS spectra as shown in **Figures S37** and **S38** are the average EXAFS spectra, which were obtained by merging 6 repeated spectra recorded at Ni and Fe K-edges, respectively. When the applied potential was higher than 1.45 V and 1.425 V vs. RHE (**Figure S39**), the formation of O₂ bubbles drastically influenced the data quality of Ni and Fe K-edge XAS signals, respectively. Therefore, we only present the XAS data recorded below the aforementioned potentials.

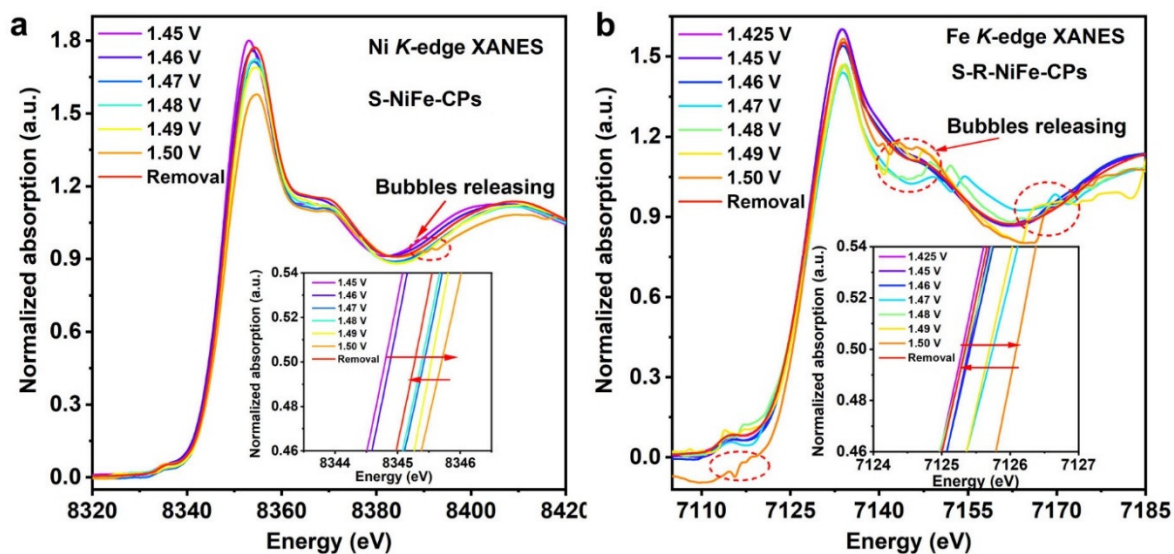


Figure S39. Operando XANES spectra of S-R-NiFe-CPs at potentials from 1.425 V to 1.45 V in 0.1 M KOH for OER: (a) Ni K-edge; (b) Fe-K edge.

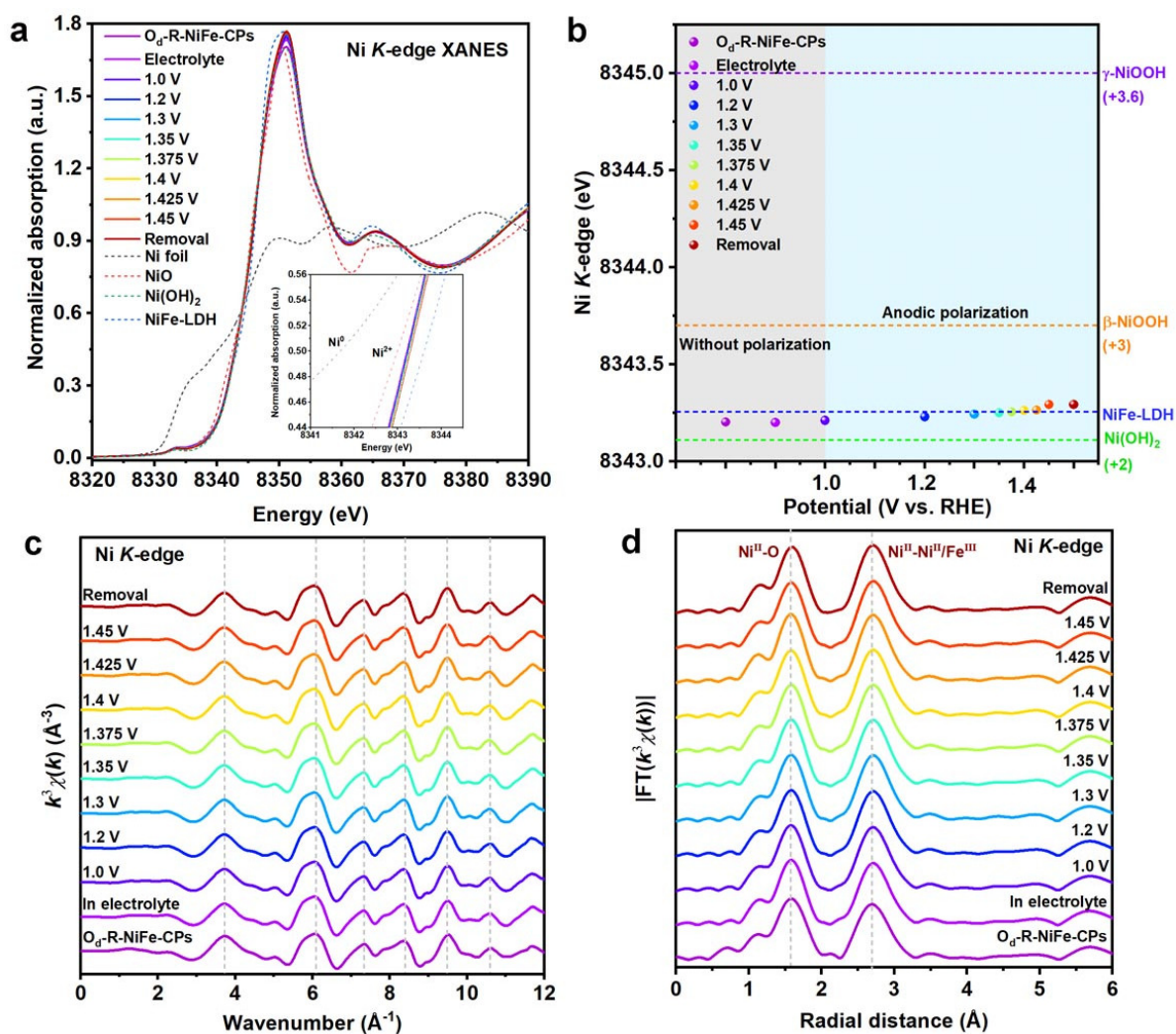


Figure S40. (a) *Operando* Ni K-edge EXAFS spectra of O_d-R-NiFe-CPs recorded at potentials from 1.0 V to 1.45 V (vs. RHE) in 0.1 M KOH towards OER vs. references. (b) Ni K-edge positions vs. applied potentials. (c, d) *Operando* Ni K-edge EXAFS and FT-EXAFS spectra of O_d-R-NiFe-CPs recorded at different potentials.

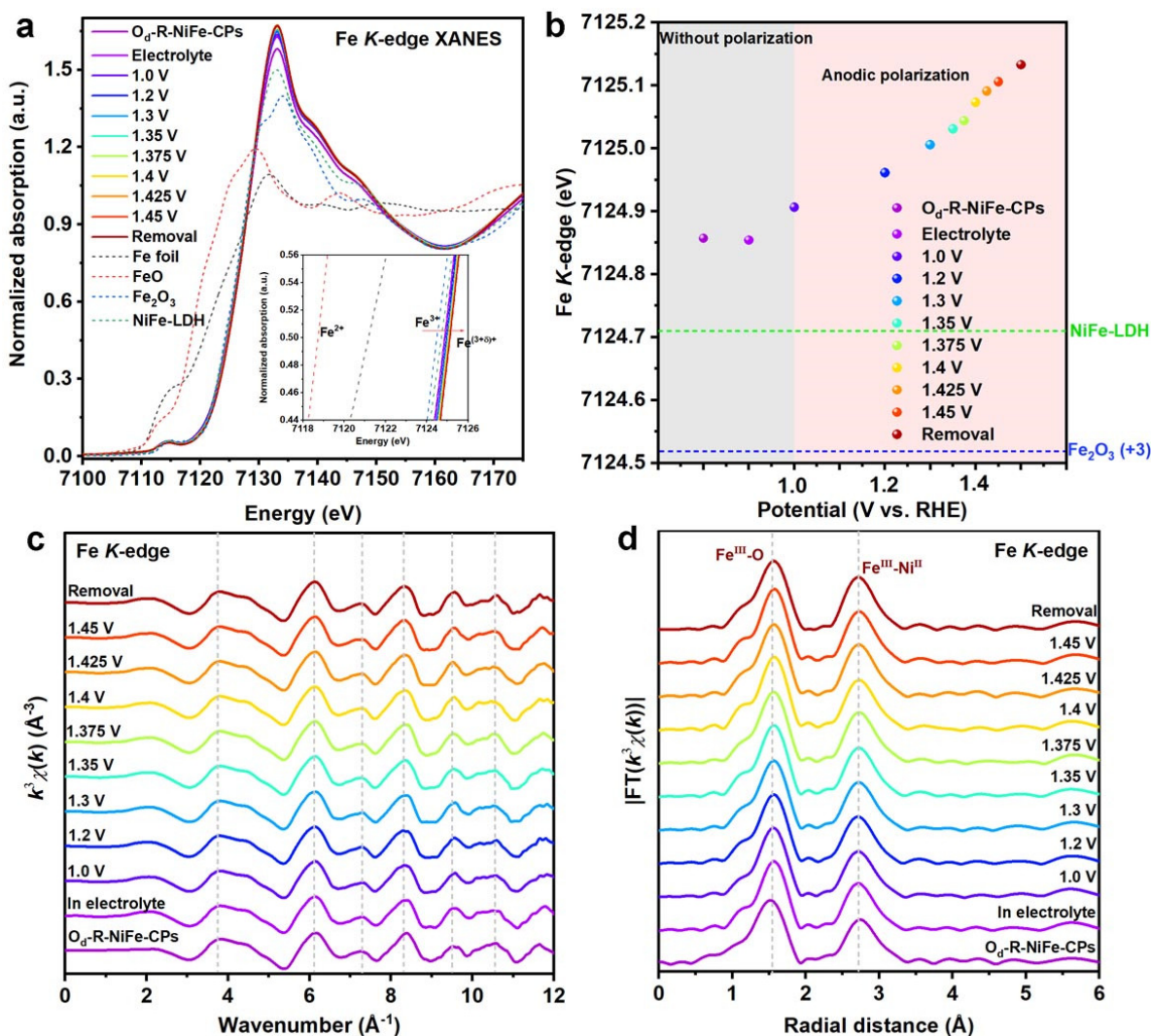


Figure S41. (a) Operando Fe K-edge EXAFS spectra of O_d -R-NiFe-CPs recorded at potentials from 1.0 V to 1.45 V (vs. RHE) in 0.1 M KOH towards OER vs. references. (b) Fe K-edge positions vs. applied potentials. (c, d) Operando Fe K-edge EXAFS and FT-EXAFS spectra of O_d -R-NiFe-CPs recorded at different potentials.

Starting with *operando* XANES spectra, our experimental results reveal similar changes in the valence state of Fe ions (**Figure S41a,b**) in O_d -R-NiFe-CPs compared with those observed in S-R-NiFe-CPs (**Figure 3c,d**), verifying the formation of high-valence Fe^{4+} species during the OER process. However, the changes in the valence states of Ni ions in O_d -R-NiFe-CPs are distinct from those of in S-R-NiFe-CPs. Although the valence state of Ni ions still shows a slight increase during the OER test (**Figure S40a,b**), the formation of high-valent $Ni^{3+/4+}$ species is much more difficult in O_d -R-NiFe-CPs under the same conditions compared with the same process for S-R-NiF-CPs (**Figure 3a,b**). Operando EXAFS and FT-EXAFS spectra of O_d -R-NiFe-CPs were further recorded to monitor the changes in the local coordination environments during the OER process. Our results (**Figures S40c,d** and **S41c,d**) show that the formation of $Ni^{III/IV}$ -O- $Fe^{III/IV}$ moieties is much more difficult in O_d -R-NiFe-CPs during the OER.

9. Operando EIS characterization

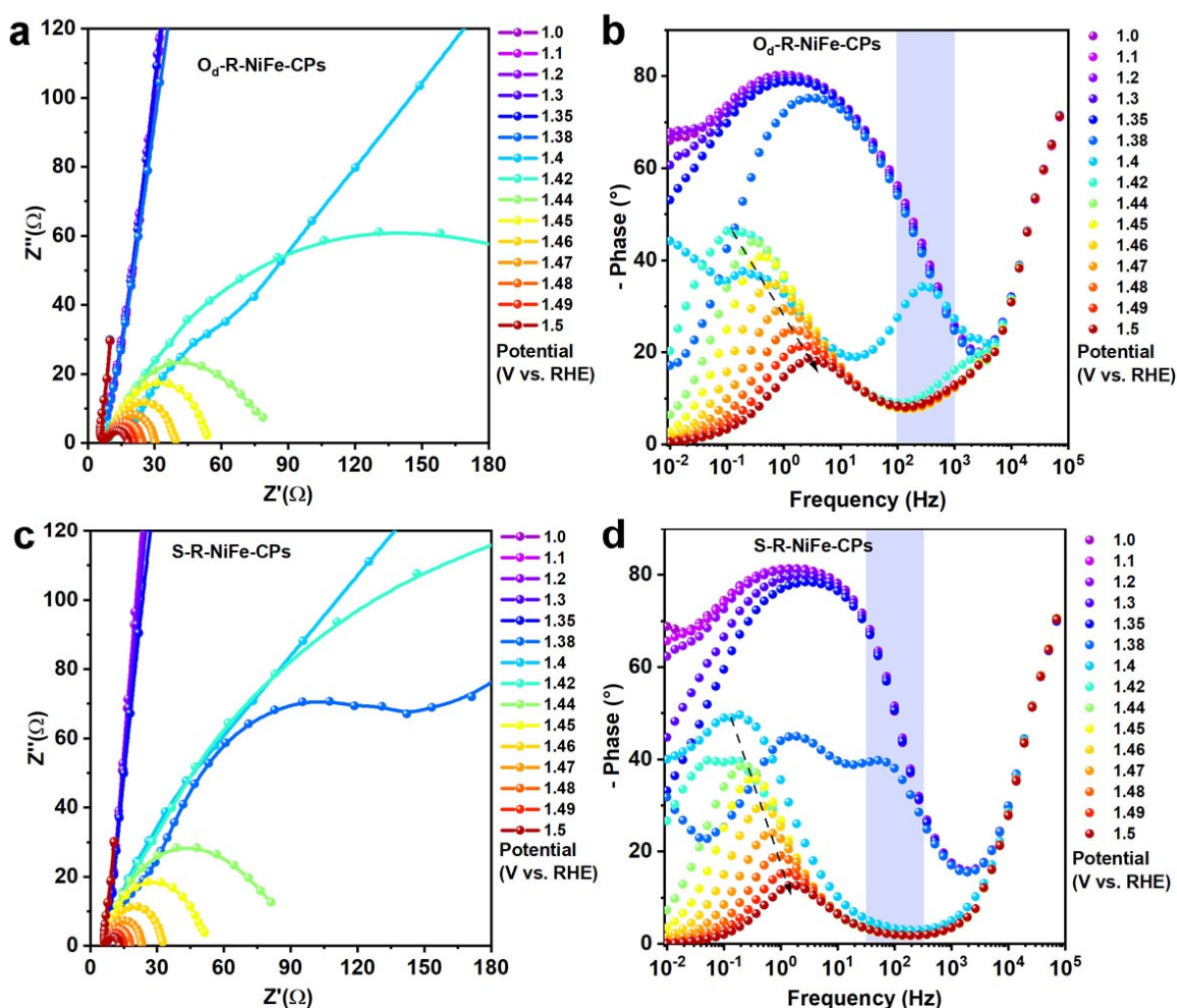


Figure S42. (a) *Operando* Nyquist plots of O_d-R-NiFe-CPs recorded at potentials from 1.0 V to 1.5 V (vs. RHE). (b) *Operando* Bode plots of O_d-R-NiFe-CPs recorded at potentials from 1.0 V to 1.5 V (vs. RHE). (c) *Operando* Nyquist plots of S-R-NiFe-CPs recorded at potentials from 1.0 V to 1.5 V (vs. RHE). (d) *Operando* Bode plots of S-R-NiFe-CPs recorded at potentials from 1.0 V to 1.5 V (vs. RHE).

As shown in **Figure S42a,c**, the Nyquist plots of both O_d-R-NiFe-CPs and S-R-NiFe-CPs feature distinct curves at different potentials, indicating that they exhibit different electrochemical behaviours. **Figure S42b,d** presents the corresponding Bode plots of two catalysts, in which the as-investigated catalysts show an extra phase peak in the middle frequency region of 100 Hz to 1000 Hz. Previous studies have demonstrated that the appearance of phase peak in the middle frequency region accounts for the appearance of double-layer capacitance, which results from the surface charge transfer processes during catalysis.^[21] In our study, the observed phase peaks (100 Hz to 1000 Hz) are primarily ascribed to the oxidation of Ni²⁺ to Ni^{3+/4+}. A close inspection of the Bode plots (**Figure S42b,d**) reveals that the oxidation of Ni ions in S-R-NiFe-CPs occurs at 1.38 V vs. RHE, which sets in around 0.02 V earlier than for O_d-R-NiFe-CPs.

10. pH-dependent OER experiments

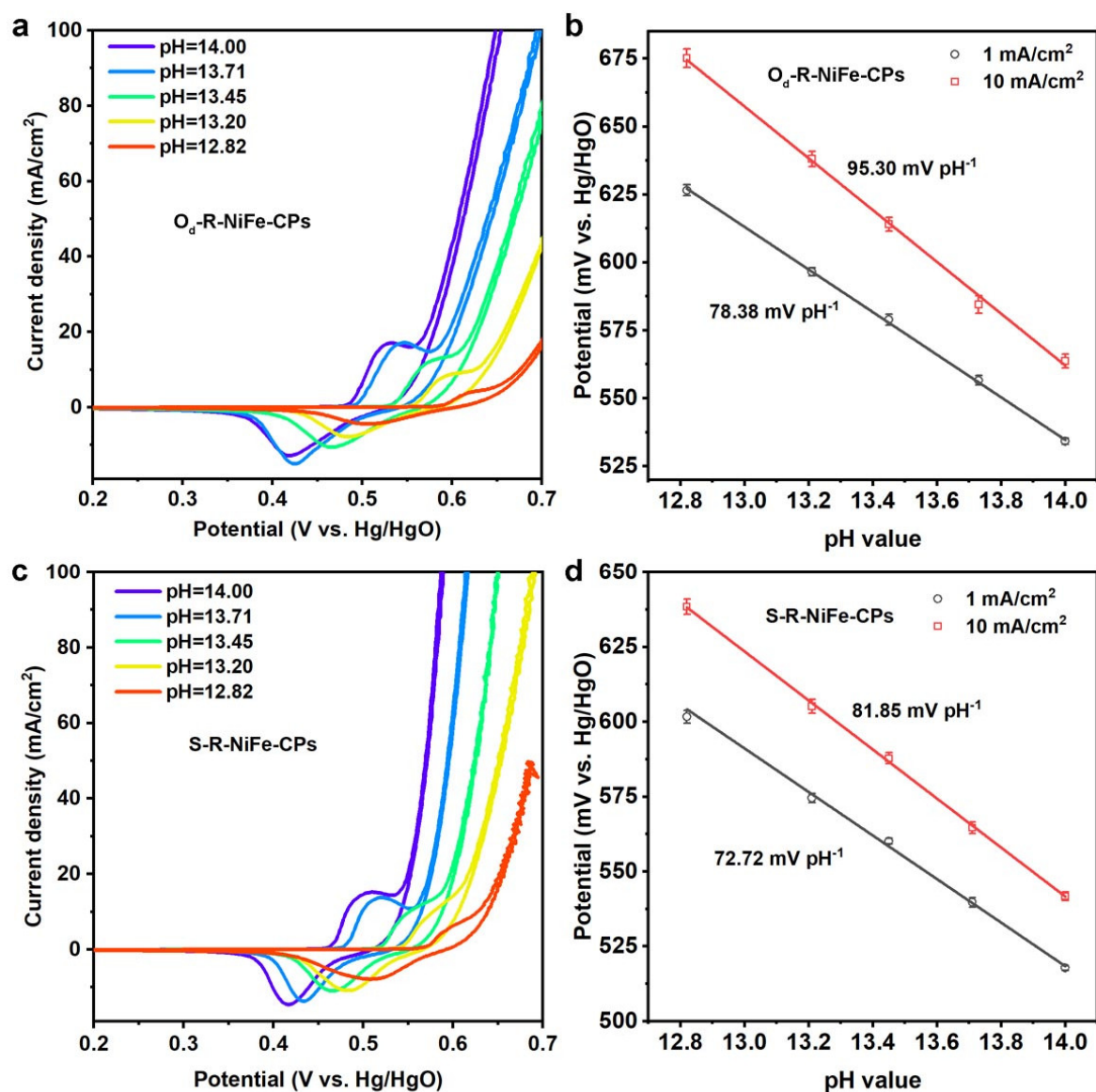


Figure S43. (a) LSV curves of O_d-R-NiFe-CPs at different pH values. (b) Pourbaix diagram of O_d-R-NiFe-CPs. (c) LSV curves of S-R-NiFe-CPs at different pH values. (d) Pourbaix diagram of S-R-NiFe-CPs.

11. Adsorption slab models for DFT simulations

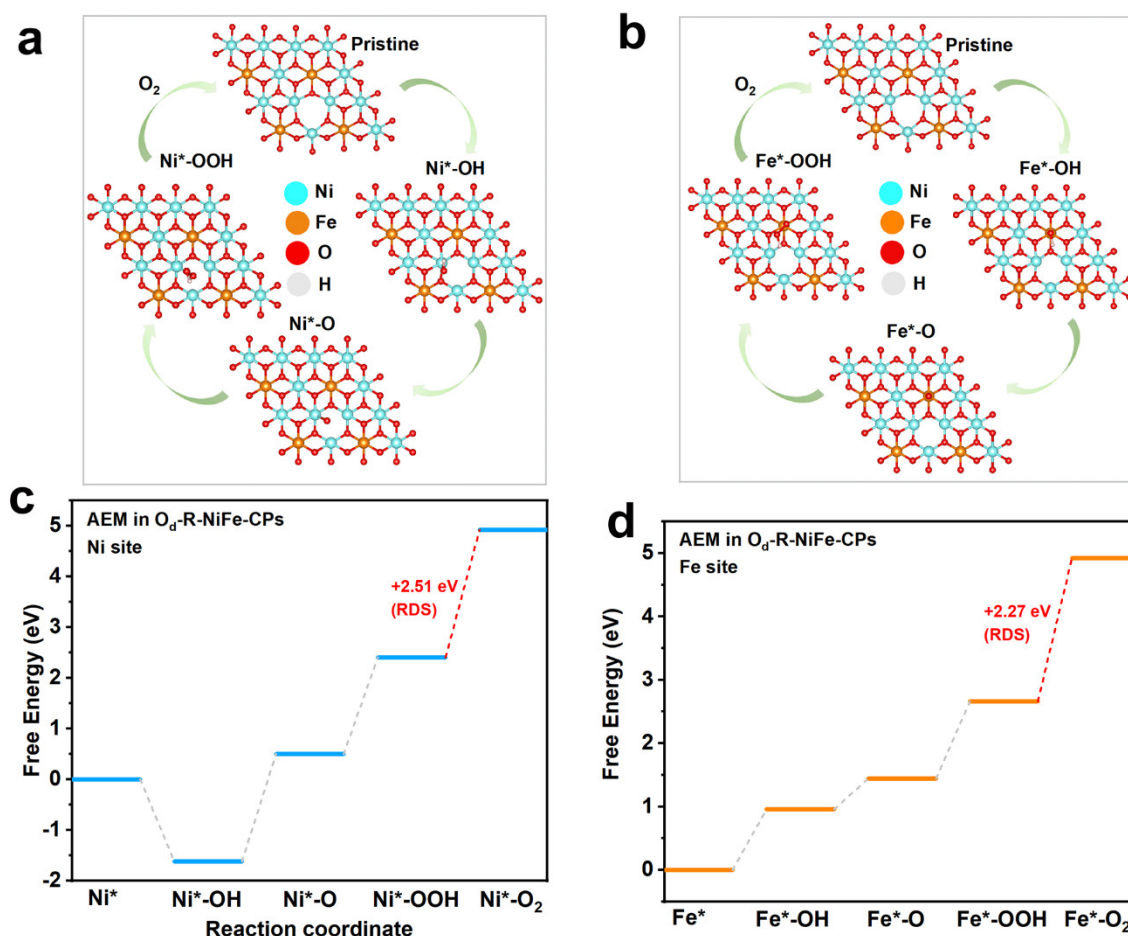


Figure S44. (a, b) Optimized adsorption slab models of O_d-R-NiFe-CPs with Ni and Fe as the active sites for OER, respectively. (c, d) Calculated free energy diagrams of OER intermediates adsorbed on Ni and Fe sites of O_d-R-NiFe-CPs (AEM).

Figure S44 presents DFT calculations for O_d-R-NiFe-CPs based on the conventional AEM mechanism. The calculations suggest that the OH⁻ adsorption on the Ni site is energetically preferential compared to the Fe sites. This is due to the regulated local electronic structure with the presence of oxygen deficiencies around Ni sites. However, for releasing O₂, the calculated results exhibit a more favorable value at Fe sites than at Ni sites (**Figure S44c,d**). The simulated free energy diagrams of OER steps reveal that the energy barriers for the rate-limiting step (RLS) at Ni and Fe sites are 2.51 eV and 2.27 eV, respectively.

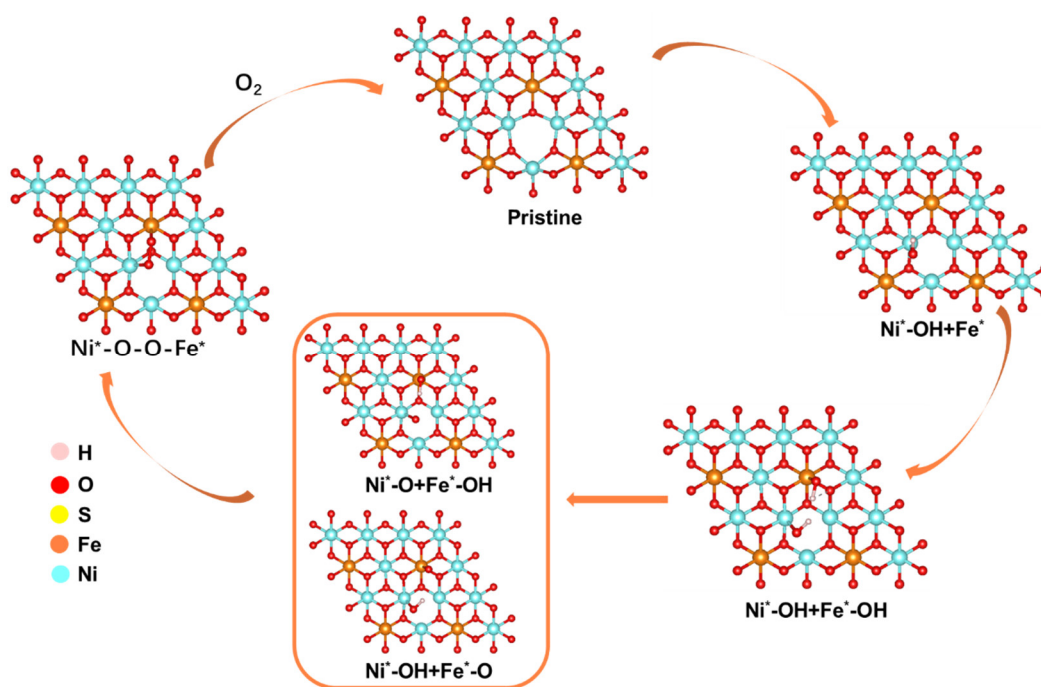


Figure S45. Optimized adsorption slab models of O_d -R-NiFe-CPs towards OER via DSM.

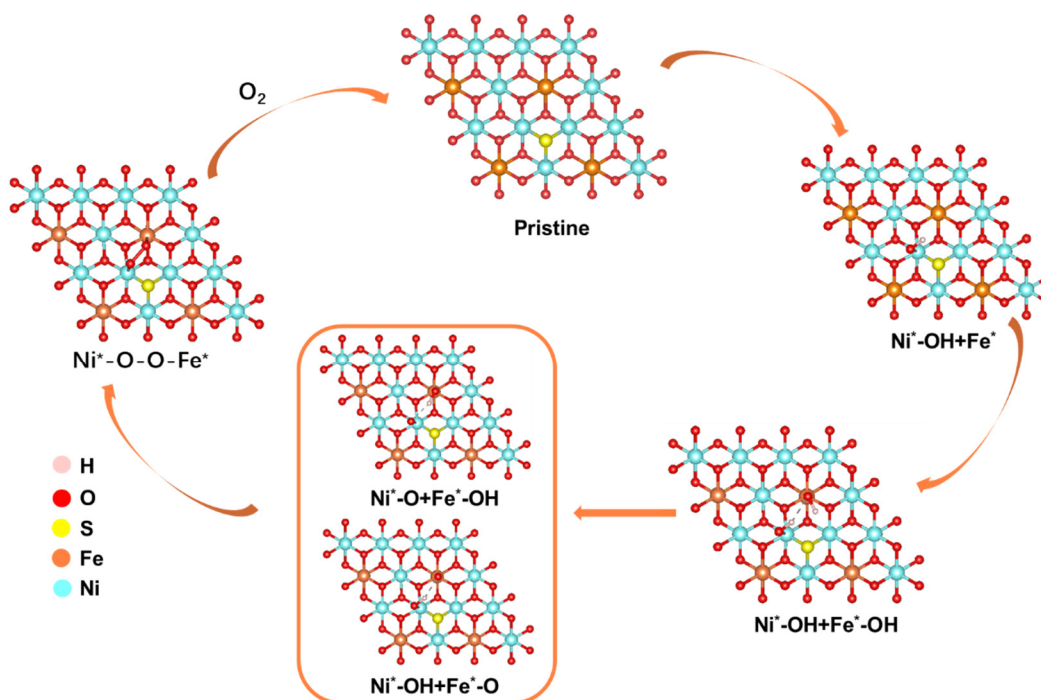


Figure S46. Optimized adsorption slab models of S-R-NiFe-CPs towards OER via DSM.

Table S1. ICP-MS results in fresh 1.0 M KOH before and after OER measurements. (Note: For the ICP-MS data collections, the catalysts were loaded on carbon paper with a loading mass of 2.0~3.0 mg/cm²)

Samples	Ni (ng/mL)	Fe (ng/mL)	S (ng/mL)
Fresh KOH	15.72	0.88	15.87
After immersion into electrolyte	10.77	0.53	14.73
After OER	10.37	0.80	15.94

Table S2. Atomic Ni/Fe/S ratios in O_d-R-NiFe-CPs, S-R-NiFe-CPs, NiFe-O, and S-NiFe-O based on ICP-MS results.

Samples	Atomic Ni/Fe ratio	Atomic Ni/Fe/S ratio
O _d -R-NiFe-CPs	3.51:1	-
S-R-NiFe-CPs (2 mg)	3.64:1	3.64:1:0.24
S-R-NiFe-CPs (5 mg)	3.58:1	3.58:1:0.79
S-R-NiFe-CPs (10 mg)	3.61:1	3.61:1:1.28
S-R-NiFe-CPs (20 mg)	3.65:1	3.65:1:2.25
S-R-NiFe-CPs (50 mg)	3.59:1	3.59:1:3.25
NiFe-O	3.37:1	-
S-NiFe-O	3.41:1	3.41:1:0.53

Table S3. Fitting parameters of the Ni *K*-edge EXAFS spectra for the as-prepared catalysts and references (**CN**: coordination numbers; **R**: interatomic distance; σ^2 : Debye-Waller factors; S_0^2 : amplitude reduction factor; ΔE : energy changes).

Samples	Path	CN	R	σ^2	S_0^2	ΔE
NiFe-LDH	Ni-O	6.00	2.06(0)	0.0069(6)	0.85	-1.70(1)
	Ni-Ni/Fe	6.00	3.12(7)	0.0093(2)		
Od-R-NiFe-CPs	Ni-O	5.15(2)	2.04(3)	0.0056(4)	0.85	-2.21(1)
	Ni-Ni/Fe	6.00	3.07(7)	0.0081(3)		
S-R-NiFe-CPs (2 mg)	Ni-O	5.11(7)	2.04(4)	0.0057(4)	0.85	-2.21(4)
	Ni-S	0.10(3)	2.12(4)	0.0030(9)		
	Ni-Ni/Fe	6.00(0)	3.08(9)	0.0092(1)		
S-R-NiFe-CPs (5 mg)	Ni-O	5.11(0)	2.05(1)	0.0051(5)	0.85	-1.84(5)
	Ni-S	0.32(3)	2.12(8)	0.0033(0)		
	Ni-Ni/Fe	6.00(0)	3.09(1)	0.0092(3)		
S-R-NiFe-CPs (10 mg)	Ni-O	5.10(2)	2.05(4)	0.0056(5)	0.85	-1.97(8)
	Ni-S	0.40(4)	2.12(8)	0.0060(7)		
	Ni-Ni/Fe	5.80(6)	3.09(2)	0.0094(3)		
S-R-NiFe-CPs (20 mg)	Ni-O	5.02(9)	2.05(3)	0.0052(9)	0.85	-2.40(5)
	Ni-S	0.55(9)	2.12(8)	0.0060(8)		
	Ni-Ni/Fe	5.62(8)	3.09(2)	0.0095(1)		
S-R-NiFe-CPs (50 mg)	Ni-O	4.83(3)	2.06(2)	0.0036(3)	0.85	-1.38(2)
	Ni-S	0.62(8)	2.12(8)	0.0067(8)		
	Ni-Ni/Fe	3.29(2)	3.10(3)	0.0095(2)		
NiO	Ni-O	6.00	2.07(0)	0.0036(3)	0.85	-4.41(7)
	Ni-Ni	12.00	2.94(7)	0.0038(2)		
NiFe-O	Ni-O	6.00(0)	2.07(0)	0.0068(1)	0.85	-3.75(6)
	Ni-Ni/Fe	10.48(3)	2.96(3)	0.0076(3)		
S-NiFe-O	Ni-O	5.73(2)	2.07(8)	0.0051(5)	0.85	-3.37(0)
	Ni-S	0.25(2)	2.10(7)	0.0089(1)		
	Ni-Ni/Fe	10.52(8)	2.96(2)	0.0076(4)		

Table S4. Fitting parameters of the Fe *K*-edge EXAFS spectra for the as-prepared catalysts and references (**CN**: coordination numbers; **R**: interatomic distances; σ^2 : Debye-Waller factors; S_0^2 : amplitude reduction factor; ΔE : energy changes).

Samples	Path	CN	R	σ^2	S_0^2	ΔE
NiFe-LDH	Ni-O	6.00	1.99(7)	0.0085(3)	0.75	0.35(2)
	Ni-Ni/Fe	6.00	3.11(4)	0.0114(6)		
O_d-R-NiFe-CPs	Fe-O	6.00	2.01(1)	0.0081(6)	0.75	1.67(6)
	Fe-Ni	6.00	3.11(5)	0.0119(6)		
S-R-NiFe-CPs (2 mg)	Fe-O	6.00	2.01(4)	0.0087(8)	0.75	1.47(5)
	Fe-Ni	6.00	3.11(7)	0.0126(9)		
S-R-NiFe-CPs (5 mg)	Fe-O	6.00	2.01(8)	0.0063(8)	0.75	-0.80(3)
	Fe-Ni	6.00	3.11(4)	0.0096(7)		
S-R-NiFe-CPs (10 mg)	Fe-O	6.00	2.02(1)	0.0081(2)	0.75	1.41(7)
	Fe-Ni	6.00	3.11(1)	0.0123(2)		
S-R-NiFe-CPs (20 mg)	Fe-O	6.00	2.01(4)	0.0078(5)	0.75	0.76(0)
	Fe-Ni	6.00	3.10(3)	0.0116(0)		
S-R-NiFe-CPs (50 mg)	Fe-O	6.00	2.01(4)	0.0069(1)	0.75	0.80(3)
	Fe-Ni	6.00	3.11(3)	0.0110(3)		
NiFe-O	Fe-O	6.00	1.97(4)	0.0107(2)	0.75	-1.32(4)
	Fe-Ni	6.00	2.98(6)	0.0112(5)		
S-NiFe-O	Fe-O	6.00	1.98(4)	0.0104(1)	0.75	-0.70(7)
	Fe-Ni	6.00	2.99(1)	0.0111(7)		

Table S5. Fitting parameters of *operando* Ni K-edge EXAFS spectra for S-R-NiFe-CPs towards OER in 0.1 M KOH (CN: coordination numbers; **R**: interatomic distances; σ^2 : Debye-Waller factors; S_0^2 : amplitude reduction factor; ΔE : energy changes).

Samples	Path	CN	R	σ^2	S_0^2	ΔE
In electrolyte	Ni-O	5.75(7)	2.05(3)	0.0052(5)	0.85	-2.27(0)
	Ni-S	0.35(0)	2.12(8)	0.0033(9)		
	Ni-Ni/Fe	6.00(0)	3.09(5)	0.0067(0)		
0.8 V vs. RHE	Ni-O	5.75(0)	2.05(0)	0.0047(3)	0.85	-2.33(8)
	Ni-S	0.33(7)	2.12(8)	0.0034(9)		
	Ni-Ni/Fe	6.00(0)	3.09(3)	0.0065(7)		
1.0 V vs. RHE	Ni-O	5.71(2)	2.05(1)	0.0046(5)	0.85	-2.22(9)
	Ni-S	0.33(3)	2.12(8)	0.0030(0)		
	Ni-Ni/Fe	6.00(0)	3.09(4)	0.0065(1)		
1.1 V vs. RHE	Ni-O	5.72(3)	2.05(1)	0.0045(1)	0.85	-2.35(8)
	Ni-S	0.35(9)	2.13(0)	0.0032(7)		
	Ni-Ni/Fe	6.00(0)	3.09(2)	0.0064(8)		
1.2 V vs. RHE	Ni-O	5.69(2)	2.05(2)	0.0046(3)	0.85	-2.25(3)
	Ni-S	0.33(3)	2.13(0)	0.0034(0)		
	Ni-Ni/Fe	6.00(0)	3.09(3)	0.0064(3)		
1.3 V vs. RHE	Ni-O	5.70(7)	2.05(1)	0.0045(6)	0.85	-2.30(4)
	Ni-S	0.33(3)	2.13(0)	0.0030(0)		
	Ni-Ni/Fe	6.00(0)	3.09(3)	0.0063(8)		
1.35 V vs. RHE	Ni-ONiOOH	1.38(7)	1.90(9)	0.0025(8)	0.85	-1.36(3)
	Ni-ONi(OH) ₂	4.01(4)	2.07(2)	0.0047(2)		
	Ni-S	0.32(2)	2.17(4)	0.0090(0)		
	Ni- Ni/FeNiOOH	1.32(1)	2.84(8)	0.0031(5)		
	Ni-Ni/Fe Ni(OH) ₂	4.71(5)	3.09(7)	0.0065(8)		
1.375 V vs. RHE	Ni-ONiOOH	2.00(8)	1.92(2)	0.0032(1)	0.85	-0.51(4)
	Ni-ONi(OH) ₂	3.26(4)	2.08(6)	0.0041(3)		
	Ni-S	0.31(9)	2.18(0)	0.0092(0)		
	Ni- Ni/FeNiOOH	1.79(1)	2.84(9)	0.0036(1)		
	Ni-Ni/Fe Ni(OH) ₂	4.17(4)	3.10(1)	0.0067(8)		
1.4 V vs. RHE	Ni-ONiOOH	2.55(7)	1.93(5)	0.0044(0)	0.85	-0.28(7)
	Ni-ONi(OH) ₂	2.90(4)	2.10(0)	0.0040(1)		
	Ni-S	0.32(7)	2.17(8)	0.0091(6)		
	Ni- Ni/FeNiOOH	2.34(4)	2.86(9)	0.0052(8)		
	Ni-Ni/Fe Ni(OH) ₂	3.89(7)	3.10(4)	0.0055(6)		
1.425 V vs. RHE	Ni-ONiOOH	3.68(4)	1.92(9)	0.0053(7)	0.85	-3.08(3)
	Ni-ONi(OH) ₂	2.09(5)	2.10(4)	0.0019(2)		
	Ni-S	0.33(3)	2.18(4)	0.0091(9)		
	Ni- Ni/FeNiOOH	2.68(1)	2.84(7)	0.0062(5)		
	Ni-Ni/Fe Ni(OH) ₂	3.22(2)	3.10(2)	0.0053(7)		
1.45 V vs. RHE	Ni-ONiOOH	4.25(2)	1.94(7)	0.0094(4)	0.85	-2.48(7)
	Ni-S	0.37(0)	2.32(5)	0.0001(9)		
	Ni- Ni/FeNiOOH	3.49(1)	2.83(7)	0.0060(7)		
	Ni-Ni/Fe Ni(OH) ₂	2.56(0)	3.08(4)	0.0048(8)		
Removed potential	Ni-ONiOOH	5.40(6)	1.90(5)	0.0086(7)	0.85	-3.40(2)
	Ni-S	0.38(8)	2.31(9)	0.0032(5)		
	Ni- Ni/FeNiOOH	4.33(8)	2.83(5)	0.0054(7)		
	Ni-Ni/FeNi(OH) ₂	1.66(2)	3.07(8)	0.0040(8)		

Table S5. Fitting parameters of *operando* Fe *K*-edge EXAFS spectra for S-R-NiFe-CPs towards OER in 0.1 M KOH (CN: coordination numbers; **R**: interatomic distances; σ^2 : Debye-Waller factors; S_0^2 : amplitude reduction factor; ΔE : energy changes).

Samples	Path	CN	R	σ^2	S_0^2	ΔE
In electrolyte	Fe-O	6.00	2.02(0)	0.0062(0)	0.75	-0.82(5)
	Fe-Ni	6.00	3.11(7)	0.0093(5)		
0.8 V vs. RHE	Fe-O	6.00	2.02(0)	0.0060(9)	0.75	-1.01(6)
	Fe-Ni	6.00	3.11(7)	0.0087(7)		
1.0 V vs. RHE	Fe-O	6.00	2.02(0)	0.0058(8)	0.75	-0.95(0)
	Fe-Ni	6.00	3.11(7)	0.0088(3)		
1.1 V vs. RHE	Fe-O	6.00	2.02(0)	0.0056(0)	0.75	-0.89(9)
	Fe-Ni	6.00	3.11(7)	0.0087(6)		
1.2 V vs. RHE	Fe-O	6.00	2.02(1)	0.0054(3)	0.75	-0.75(0)
	Fe-Ni	6.00	3.11(9)	0.0088(9)		
1.3 V vs. RHE	Fe-O	6.00	2.02(1)	0.0051(3)	0.75	-0.77(9)
	Fe-Ni	6.00	3.11(8)	0.0086(6)		
1.35 V vs. RHE	Fe-O	6.00	2.01(5)	0.0063(7)	0.75	-0.82(6)
	Fe-Ni ^{III}	0.83(0)	2.83(7)	0.0027(2)		
	Fe-Ni ^{II}	5.25(6)	3.08(9)	0.0091(1)		
1.375 V vs. RHE	Fe-O	5.75(0)	2.00(6)	0.0065(8)	0.75	-0.65(4)
	Fe-Ni ^{III}	1.40(8)	2.86(5)	0.0036(8)		
	Fe-Ni ^{II}	4.55(3)	3.11(5)	0.0082(6)		
1.4 V vs. RHE	Fe-O	5.43(3)	2.00(6)	0.0063(1)	0.75	-0.48(7)
	Fe-Ni ^{III}	1.53(2)	2.87(9)	0.0043(6)		
	Fe-Ni ^{II}	4.34(3)	3.11(8)	0.0077(5)		
1.425 V vs. RHE	Fe-O	5.33(2)	1.95(5)	0.0061(2)	0.75	-3.09(9)
	Fe-Ni ^{III}	1.70(9)	2.84(1)	0.0061(8)		
	Fe-Ni ^{II}	3.59(9)	3.08(5)	0.0098(8)		
Removed potential	Fe-O	5.22(7)	1.98(8)	0.0067(3)	0.75	-0.36(3)
	Fe-Ni ^{III}	3.23(9)	2.84(5)	0.0045(7)		
	Fe-Ni ^{II}	2.03(6)	3.07(5)	0.0051(6)		

Table S6. Comparison of OER performance of the as-prepared catalysts with recent representative studies on NiFe-based OER electrocatalysts.

Electrode materials	Overpotential (mV) at 10 mA/cm ²	Tafel slope (mV/dec)	Stability (h)	Substrate	Ref.
FeCoO _x -Vo-S	217	21	8 h	GC-RDE	[21]
Ni(Fe)OOH-FeS _x	220	55	16 h	Ni foam	[22]
EA-FCCN	221	38.7	20 h	Graphite paper	[23]
ATCH-Fe-S	225	64.1	16 h	Ni foam	[24]
S-(Ni,Fe)OOH	229	48.9	100 h	Ni foam	[25]
M-PCBN	232	32	60 h	Graphite paper	[26]
(Ni,Fe)OOH with SO ₄ ²⁻	234 (50 mA/cm ²)	27.7	100 h	Ni foam	[27]
NiCo-(oxy)hydroxysulfides	234	63	80 h	Carbon cloth	[28]
CoFe LDHs-Ar	237	37.85	-	GC-RDE	[29]
Ru SAs/C-FeCoNi	238	48	48 h	GC-RDE	[30]
Co ₈₀ Fe ₂₀ (OH)(OCH ₃)	240	53.45	10 h	GC-RDE	[31]
R-NCO	240	50	50 h	Ni foam	[32]
CoOOH/Co ₉ S ₈	240	86.4	160	Carbon cloth	[33]
o-CoTe ₂ @HPC/CNTs	241	46	24 h	GC-RDE	[34]
Fe,Ni-CoS ₂	242	35	500 h	GC-RDE	[35]
NiFe LDHs-V _{Fe}	245	70	-	GC-RDE	[36]
Fe-CoMo UH	245	37	90 h	Ni foam	[37]
Ni-Fe-Se nanocages	249	36	150 h	GC-RDE	[38]
CoV-UAH	250	44	170 h	Au foam	[39]
Fe-Co-O NSs	260	53	16 h	GC-RDE	[40]
NiO/Co ₃ O ₄	262	58	-	Ni foam	[41]
S-NiFe ₂ O ₄ /NF	267	36.7	24 h	Ni foam	[42]
Co ₃ Fe LDHs-SF ₆	268	40.12	-	GC-RDE	[43]
S-CoO _x	270	109	-	GC-RDE	[44]
S-NiFe-LDH-9-A	270 (50 mA/cm ²)	40	33 h	MoNi foam	[45]
Ni/Ni(OH) ₂	270	70	10	Ni foam	[46]
Fe _{0.4} Co _{0.6} Se ₂	270	36	24 h	GC-RDE	[47]
Fe-NiO/NiS ₂	270	40	10 h	Graphite paper	[48]
NFO/NF	272	43	12 h	Ni foam	[49]
Ni(Fe)OOH	275	45.9	20	Ni foam	[50]
P-Co ₃ O ₄	280	51.6	11 h	Ti mesh	[51]
NiFe-LDH nanoprisms	280	49.4	6 h	GC-RDE	[52]
NiFe-PB-V _{CN}	283	54	40 h	GC-RDE	[53]
CoSe ₂ UNMvac	284	46.3	20 h	GC-RDE	[54]
LDH-10	286	82	6 h	GC-RDE	[55]
FeOOH(Se)/IF	287	54	15 h	Fe foam	[56]
LC-CoOOH NAs/CFC	294	70.73	24 h	Graphite paper	[57]
CoSe ₂ -D _{Fe} -V _{Co}	294	53.5	14 h	GC-RDE	[58]
CoP-B1	297	58.1	11 h	GC-RDE	[59]
NiCo-LDHG	337	52	4 h	GC-RDE	[60]
Co ₉ S ₈ @Fe ₃ O ₄	350 (500 mA/cm ²)	54	120 h	Ni foam	[61]
ODAC-CoO	364	68.6	12 h	Graphite paper	[62]
NiFe-O	323	50.09	-	GC-RDE	This work
S-NiFe-O	269	31.90	-	GC-RDE	This work
O_d-R-NiFe-CPs	246	49.10	-	GC-RDE	This work
S-R-NiFe-CPs	234	30.28	26 h	GC-RDE	This work

References

- [1] Zhao, Y.; Wan, W.; Chen, Y.; Erni, R.; Triana, C. A.; Li, J.; Mavrokefalos, C. K.; Zhou, Y.; Patzke, G. R. Understanding and Optimizing Ultra-Thin Coordination Polymer Derivatives with High Oxygen Evolution Performance. *Adv. Energy Mater.* **2020**, *10*, 2002228.
- [2] Trotochaud, L.; Young, S. L.; Ranney, J. K.; Boettcher, S. W. Nickel-Iron Oxyhydroxide Oxygen-Evolution Electrocatalysts: The Role of Intentional and Incidental Iron Incorporation. *J. Am. Chem. Soc.* **2014**, *136*, 6744-6753.
- [3] Spanos, I.; Tesch, M. F.; Yu, M.; Tüysüz, H.; Zhang, J.; Feng, X.; Müllen, K.; Schlögl, R.; Mechler, A. K. Facile Protocol for Alkaline Electrolyte Purification and Its Influence on a Ni-Co Oxide Catalyst for the Oxygen Evolution Reaction. *ACS Catal.* **2019**, *9*, 8165-8170.
- [4] Farhat, R.; Dhainy, J.; Halaoui, L. I. OER Catalysis at Activated and Codeposited NiFe-Oxo/Hydroxide Thin Films Is Due to Postdeposition Surface-Fe and Is Not Sustainable without Fe in Solution. *ACS Catal.* **2020**, *10*, 20-35.
- [5] Huang, Z.-F.; Song, J.; Du, Y.; Xi, S.; Dou, S.; Nsanzimana, J. M. V.; Wang, C.; Xu, Z. J.; Wang, X. Chemical and Structural Origin of Lattice Oxygen Oxidation in Co-Zn Oxyhydroxide Oxygen Evolution Electrocatalysts. *Nat. Energy* **2019**, *4*, 329-338.
- [6] VandeVondele, J.; Hutter, J. Gaussian Basis Sets for Accurate Calculations on Molecular Systems in Gas and Condensed Phases. *J. Chem. Phys.* **2007**, *127*, 114105.
- [7] Hutter, J.; Iannuzzi, M.; Schiffmann, F.; VandeVondele, J. cp2k: Atomistic Simulations of Condensed Matter Systems. *Comput. Mol. Sci.* **2014**, *4*, 15-25.
- [8] Wan, W.; Triana, C. A.; Lan, J.; Li, J.; Allen, C. S.; Zhao, Y.; Iannuzzi, M.; Patzke, G. R. Bifunctional Single Atom Electrocatalysts: Coordination-Performance Correlations and Reaction Pathways. *ACS Nano* **2020**, *14*, 13279-13293.
- [9] Nørskov, J. K.; Rossmeisl, J.; Logadottir, A.; Lindqvist, L.; Kitchin, J. R.; Bligaard, T.; Jónsson, H. Origin of the Overpotential for Oxygen Reduction at a Fuel-Cell Cathode. *J. Phys. Chem. B* **2004**, *108*, 17886-17892.
- [10] Rossmeisl, J.; Logadottir, A.; Nørskov, J. K. Electrolysis of Water on (Oxidized) Metal Surfaces. *Chem. Phys.* **2005**, *319*, 178-184.
- [11] Peterson, A. A.; Abild-Pedersen, F.; Studt, F.; Rossmeisl, J.; Nørskov, J. K. How Copper Catalyzes the Electroreduction of Carbon Dioxide into Hydrocarbon Fuels. *Energy Environ. Sci.* **2010**, *3*, 1311-1315.
- [12] Görlin, M.; Ferreira de Araújo, J.; Schmies, H.; Bernsmeier, D.; Dresp, S.; Gliech, M.; Jusys, Z.; Chernev, P.; Kraehnert, R.; Dau, H.; Strasser, P. Tracking Catalyst Redox States and Reaction Dynamics in Ni-Fe Oxyhydroxide Oxygen Evolution Reaction Electrocatalysts: The Role of Catalyst Support and Electrolyte pH. *J. Am. Chem. Soc.* **2017**, *139*, 2070-2082.
- [13] Grimaud, A.; Diaz-Morales, O.; Han, B.; Hong, W. T.; Lee, Y.-L.; Giordano, L.; Stoerzinger, K. A.; Koper, M. T. M.; Shao-Horn, Y. Activating Lattice Oxygen Redox Reactions in Metal Oxides to Catalyze Oxygen Evolution. *Nat. Chem.* **2017**, *9*, 457-465.
- [14] Huang, Z.-F.; Xi, S.; Song, J.; Dou, S.; Du, Y.; Diao, C.; Xu, Z. J.; Wang, X. Tuning of Lattice Oxygen Reactivity and Scaling Relation to Construct Better Oxygen Evolution Electrocatalyst. *Nat. Commun.* **2021**, *12*, 3992.
- [15] Pan, Y.; Xu, X.; Zhong, Y.; Ge, L.; Chen, Y.; Veder, J.-P. M.; Guan, D.; O'Hayre, R.; Li, M.; Wang, G.; Wang, H.; Zhou, W.; Shao, Z. Direct Evidence of Boosted Oxygen Evolution Over Perovskite by Enhanced Lattice Oxygen Participation. *Nat. Commun.* **2020**, *11*, 2002.
- [16] Voiry, D.; Chhowalla, M.; Gogotsi, Y.; Kotov, N. A.; Li, Y.; Penner, R. M.; Schaak, R. E.; Weiss, P. S. Best Practices for Reporting Electrocatalytic Performance of Nanomaterials. *ACS Nano* **2018**, *12*, 9635-9638.
- [17] El-Sayed, H. A.; Weiß, A.; Olbrich, L. F.; Putro, G. P.; Gasteiger, H. A. OER Catalyst Stability Investigation Using RDE Technique: A Stability Measure or an Artifact. *J. Electrochem. Soc.* **2019**, *166*, f458.
- [18] Shi, Y.; Du, W.; Zhou, W.; Wang, C.; Lu, S.; Lu, S.; Zhang, B. Unveiling the Promotion of Surface-Adsorbed Chalcogenate on the Electrocatalytic Oxygen Evolution Reaction. *Angew. Chem. Int. Ed.* **2020**, *59*, 22470-22474.
- [19] Hausmann, J. N.; Menezes, P. W. Effect of Surface-Adsorbed and Intercalated (Oxy)anions on the Oxygen Evolution Reaction. *Angew. Chem. Int. Ed.* **2022**, e202207279.
- [20] Wu, Y.; Liu, C.; Wang, C.; Yu, Y.; Shi, Y.; Zhang, B. Converting Copper Sulfide to Copper with Surface Sulfur for Electrocatalytic Alkyne Semi-Hydrogenation with Water. *Nat. Commun.* **2021**, *12*, 3881.
- [21] Xiao, Z.; Huang, Y.; Dong, C.-L.; Xie, C.; Liu, Z.; Du, S.; Chen, W.; Yan, D.; Li Tao; Shu, Z.; Zhang, G.; Duan, H.; Wang, Y.; Zou, Y.; Chen, R.; Wang, S. *Operando* Identification of the Dynamic Behavior of Oxygen Vacancy-Rich Co₃O₄ for Oxygen Evolution Reaction. *J. Am. Chem. Soc.* **2020**, *142*, 12087-12095.
- [21] Zhuang, L.; Jia, Y.; Liu, H.; Li, Z.; Li, M.; Zhang, L.; Wang, X.; Yang, D.; Zhu, Z.; Yao, X. Sulfur-Modified Oxygen Vacancies in Iron-Cobalt Oxide Nanosheets: Enabling Extremely High Activity of the Oxygen Evolution Reaction to Achieve the Industrial Water Splitting Benchmark. *Angew. Chem. Int. Ed.* **2020**, *59*, 14664-14670.

- [22] Yang, H.; Gong, L.; Wang, H.; Dong, C.; Wang, J.; Qi, K.; Liu, H.; Guo, X.; Xia, B. Y. Preparation of Nickel-Iron Hydroxides by Microorganism Corrosion for Efficient Oxygen Evolution. *Nat. Commun.* **2020**, *11*, 5075.
- [23] Zhang, N.; Feng, X.; Rao, D.; Deng, X.; Cai, L.; Qiu, B.; Long, R.; Xiong, Y.; Lu, Y.; Chai, Y. Lattice Oxygen Activation Enabled by High-Valence Metal Sites for Enhanced Water Oxidation. *Nat. Commun.* **2020**, *11*, 4066.
- [24] Yuan, D.; Dou, Y.; He, C.-T. Yu, L.; Xu, L.; Adekoya, D.; Xia, Q.; Ma, J.; Dou, S. X.; Zhang, S. Sulfur Doping Optimized Intermediate Energetics of FeCoOOH for Enhanced Oxygen Evolution Catalytic Activity. *Cell Rep. Phys. Sci.* **2021**, *2*, 100331.
- [25] Yu, L.; Wu, L.; McElhenny, B.; Song, S.; Luo, D.; Zhang, F.; Yu, Y.; Chen, S.; Ren, Z. Ultrafast Room-Temperature Synthesis of Porous S-Doped Ni/Fe (Oxy) Hydroxide Electrodes for Oxygen Evolution Catalysis in Seawater Splitting. *Energy Environ. Sci.* **2020**, *13*, 3439-3446.
- [26] Zhang, W.; Wang, Y.; Zheng, H.; Li, R.; Tang, Y.; Li, B.; Zhu, C.; You, L.; Gao, M.-R.; Liu, Z.; Yu, S.-H. Zhou, K. Embedding Ultrafine Metal Oxide Nanoparticles in Monolayered Metal-Organic Framework Nanosheets Enables Efficient Electrocatalytic Oxygen Evolution. *ACS Nano* **2020**, *14*, 1971-1981.
- [27] Liao, H.; Luo, T.; Tan, P.; Chen, K.; Lu, L.; Liu, Y.; Liu, M.; Pan, J. Unveiling Role of Sulfate Ion in Nickel-Iron (Oxy) Hydroxide with Enhanced Oxygen-Evolving Performance. *Adv. Funct. Mater.* **2021**, *31*, 2102772.
- [28] Zheng, X.; Cao, Y.; Wu, Z.; Ding, W.; Xue, T.; Wang, J.; Chen, Z.; Han, X.; Deng, Y.; Hu, W. Rational Design and Spontaneous Sulfurization of NiCo-(oxy)Hydroxysulfides Nanosheets with Modulated Local Electronic Configuration for Enhancing Oxygen Electrocatalysis. *Adv. Energy Mater.* **2022**, *12*, 2103275.
- [29] Wang, Y.; Zhang, Y.; Liu, Z.; Xie, C.; Feng, S.; Liu, D.; Shao, M.; Wang, S. Layered Double Hydroxide Nanosheets with Multiple Vacancies Obtained by Dry Exfoliation as Highly Efficient Oxygen Evolution Electrocatalysts. *Angew. Chem. Int. Ed.* **2017**, *56*, 5867-5871.
- [30] Hu, Y.; Luo, G.; Wang, L.; Liu, X.; Qu, Y.; Zhou, Y.; Zhou, F.; Li, Z.; Li, Y.; Yao, T.; Xiong, C.; Yang, B.; Yu, Z.; Wu, Y. Single Ru Atoms Stabilized by Hybrid Amorphous/Crystalline FeCoNi Layered Double Hydroxide for Ultraefficient Oxygen Evolution. *Adv. Energy Mater.* **2021**, *11*, 2002816.
- [31] He, J.; Liu, Y.; Huang, Y.; Li, H.; Zou, Y.; Dong, C.-L.; Wang, S. Fe²⁺-Induced *In Situ* Intercalation and Cation Exsolution of Co₈₀Fe₂₀(OH)(OCH₃) with Rich Vacancies for Boosting Oxygen Evolution Reaction. *Adv. Funct. Mater.* **2021**, *31*, 2009245.
- [32] Peng, S.; Gong, F.; Li, L.; Yu, D.; Ji, D.; Zhang, T.; Hu, Z.; Zhang, Z.; Chou, S.; Du, Y.; Ramakrishna, S. Necklace-like Multishelled Hollow Spinel Oxides with Oxygen Vacancies for Efficient Water Electrolysis. *J. Am. Chem. Soc.* **2018**, *140*, 13644-13653.
- [33] Yao, N.; Wang, G.; Jia, H.; Yin, J.; Cong, H.; Chen, S.; Luo, W. Intermolecular Energy Gap-Induced Formation of High-Valent Cobalt Species in CoOOH Surface Layer on Cobalt Sulfides for Efficient Water Oxidation. *Angew. Chem. Int. Ed.* **2022**, *61*, e202117178.
- [34] Chen, Z.; Chen, M.; Yan, X.; Jia, H.; Fei, B.; Ha, Y.; Qing, H.; Yang, H.; Liu, M.; Wu, R. Vacancy Occupation-Driven Polymorphic Transformation in Cobalt Ditelluride for Boosted Oxygen Evolution Reaction. *ACS Nano* **2020**, *14*, 6968-6979.
- [35] Peng, W.; Deshmukh, A.; Chen, N.; Lv, Z.; Zhao, S.; Li, J.; Yan, B.; Gao, X.; Shang, L.; Gong, Y.; Wu, L. Deciphering the Dynamic Structure Evolution of Fe- and Ni-Codoped CoS₂ for Enhanced Water Oxidation. *ACS Catal.* **2022**, *12*, 3743-3751.
- [36] Wang, Y.; Qiao, M.; Li, Y.; Wang, S. Tuning Surface Electronic Configuration of NiFe LDHs Nanosheets by Introducing Cation Vacancies (Fe or Ni) as Highly Efficient Electrocatalysts for Oxygen Evolution Reaction. *Small* **2018**, *14*, 1800136.
- [37] Zeng, L.; Cao, B.; Wang, X.; Liu, H.; Shang, J.; Lang, J.; Cao, X.; Gu, H. Ultrathin Amorphous Iron-Doped Cobalt-Molybdenum Hydroxide Nanosheets for Advanced Oxygen Evolution Reactions. *Nanoscale* **2021**, *13*, 3153-3160.
- [38] Wu, Z.-P.; Zhang, H.; Zuo, S.; Wang, Y.; Zhang, S. L.; Zhang, J.; Zang, S.-Q.; Lou, X. W. Manipulating the Local Coordination and Electronic Structures for Efficient Electrocatalytic Oxygen Evolution. *Adv. Mater.* **2021**, *33*, 2103004.
- [39] Liu, J.; Ji, Y.; Nai, J.; Niu, X.; Luo, Y.; Guo, L.; Yang, S. Ultrathin Amorphous Cobalt-Vanadium Hydr(oxy)oxide Catalysts for the Oxygen Evolution Reaction. *Energy Environ. Sci.* **2018**, *11*, 1736-1741.
- [40] Wang, Q.; Xue, X.; Lei, Y.; Wang, Y.; Feng, Y.; Xiong, X.; Wang, D.; Li, Y. Engineering of Electronic States on Co₃O₄ Ultrathin Nanosheets by Cation Substitution and Anion Vacancies for Oxygen Evolution Reaction. *Small* **2020**, *16*, 2001571.
- [41] Zhang, J.; Qian, J.; Ran, J.; Xi, P.; Yang, L.; Gao, D. Engineering Lower Coordination Atoms onto NiO/Co₃O₄ Heterointerfaces for Boosting Oxygen Evolution Reactions. *ACS Catal.* **2020**, *10*, 12376-12384.
- [42] Liu, J.; Zhu, D.; Ling, T.; Vasileff, A.; Qiao, S.-Z. S-NiFe₂O₄ Ultra-Small Nanoparticle Built Nanosheets for Efficient Water Splitting in Alkaline and Neutral pH. *Nano Energy* **2017**, *40*, 264-273.
- [43] Liu, Z.; Huang, Y.; Wang, Y.; Cen, J.; Yang, H.; Chen, X.; Tong, X.; Su, D.; Dong, C.-L.; Wang, S. Quinary Defect-Rich Ultrathin Bimetal Hydroxide Nanosheets for Water Oxidation. *ACS Appl. Mater. Interfaces* **2019**, *11*, 44018-44025.

- [44] Yu, X.; Yu, Z.-Y.; Zhang, X.-L.; Li, P.; Sun, B.; Gao, X.; Yan, K.; Liu, H.; Duan, Y.; Gao, M.-R.; Wang, G.; Yu, S.-H. Highly Disordered Cobalt Oxide Nanostructure Induced by Sulfur Incorporation for Efficient Overall Water Splitting. *Nano Energy* **2020**, *71*, 104652.
- [45] Zhou, Y.-N.; Yu, W.-L.; Cao, Y.-N.; Zhao, J.; Dong, B.; Ma, Y.; Wang, F.-L.; Fan, R.-Y.; Zhou, Y.-L.; Chai, Y.-M. S-Doped Nickel-Iron Hydroxides Synthesized by Room-Temperature Electrochemical Activation for Efficient Oxygen Evolution. *Appl. Catal. B Environ.* **2021**, *292*, 120150.
- [46] Gao, L.; Cui, X.; Wang, Z.; Sewell, C. D.; Li, Z.; Liang, S.; Zhang, M.; Li, J.; Hu, Y.; Lin, Z. *Operando* Unraveling Photothermal-Promoted Dynamic Active-Sites Generation in NiFe₂O₄ for Markedly Enhanced Oxygen Evolution. *PNAS* **2021**, *118*, e2023421118.
- [47] Zhang, J.; Yan, Y.; Mei, B.; Qi, R.; He, T.; Wang, Z.; Fang, W.; Zaman, S.; Su, Y.; Ding, S.; Xia, B. Y. Local Spin-State Tuning of Cobalt-Iron Selenide Nanoframes for the Boosted Oxygen Evolution. *Energy Environ. Sci.* **2021**, *14*, 365-373.
- [48] Zhang, N.; Hu, Y.; An, L.; Li, Q.; Yin, J.; Li, J.; Yang, R.; Lu, M.; Zhang, S.; Xi, P.; Yan, C.-H. Surface Activation and Ni-S Stabilization in NiO/NiS₂ for Efficient Oxygen Evolution Reaction. *Angew. Chem. Int. Ed.* **2022**, e202207217.
- [49] Dai, L.; Chen, Z.-N.; Li, L.; Yin, P.; Liu, Z.; Zhang, H. Ultrathin Ni(0)-Embedded Ni(OH)₂ Heterostructured Nanosheets with Enhanced Electrochemical Overall Water Splitting. *Adv. Mater.* **2020**, *32*, 1906915.
- [50] Gong, L.; Yang, H.; Wang, H.; Qi, R.; Wang, J.; Chen, S.; You, B.; Dong, Z.; Liu, H.; Xia, B. Y. Corrosion Formation and Phase Transformation of Nickel-Iron Hydroxide Nanosheets Array for Efficient Water Oxidation. *Nano Res.* **2021**, *14*, 4528-4533.
- [51] Xiao, Z.; Wang, Y.; Huang, Y.; Wei, Z.; Dong, C.-L.; Ma, J.; Shen, S.; Li, Y.; Wang, S. Filling the Oxygen Vacancies in Co₃O₄ with Phosphorus: An Ultra-Efficient Electrocatalyst for Overall Water Splitting. *Energy Environ. Sci.* **2017**, *10*, 2563-2569.
- [52] Yu, L.; Yang, J. F.; Guan, B. Y.; Lu, Y.; Lou, X. W. Hierarchical Hollow Nanoprisms Based on Ultrathin Ni-Fe Layered Double Hydroxide Nanosheets with Enhanced Electrocatalytic Activity towards Oxygen Evolution. *Angew. Chem. Int. Ed.* **2018**, *57*, 172-176.
- [53] Yu, Z.-Y.; Duan, Y.; Liu, J.-D.; Chen, Y.; Liu, X.-K.; Liu, W.; Ma, T.; Li, Y.; Zheng, X.-S.; Yao, T.; Gao, M.-R.; Zhu, J.-F.; Ye, B.-J.; Yu, S.-H. Unconventional CN Vacancies Suppress Iron-Leaching in Prussian Blue Analogue Pre-Catalyst for Boosted Oxygen Evolution Catalysis. *Nat. Commun.* **2019**, *10*, 2799.
- [54] Zhang, Y.; Zhang, C.; Guo, Y.; Liu, D.; Yu, Y.; Zhang, B. Selenium Vacancy-Rich CoSe₂ Ultrathin Nanomeshes with Abundant Active Sites for Electrocatalytic Oxygen Evolution. *J. Mater. Chem. A* **2019**, *7*, 2536-2540.
- [55] Zhao, C.-X.; Li, B.-Q.; Zhao, M.; Liu, J.-N.; Zhao, L.-D.; Chen, X.; Zhang, Q. Precise Anionic Regulation of NiFe Hydroxysulfide Assisted by Electrochemical Reactions for Efficient Electrocatalysis. *Energy Environ. Sci.* **2020**, *13*, 1711-1716.
- [56] Niu, S.; Jiang, W.-J.; Wei, Z.; Tang, T.; Ma, J.; Hu, J.-S.; Wan, L.-J. Se-Doping Activates FeOOH for Cost-Effective and Efficient Electrochemical Water Oxidation. *J. Am. Chem. Soc.* **2019**, *141*, 7005-7013.
- [57] Ye, S.; Wang, J.; Hu, J.; Chen, Z.; Zheng, L.; Fu, Y.; Lei, Y.; Ren, X.; He, C.; Zhang, Q.; Liu, J. Electrochemical Construction of Low-Crystalline CoOOH Nanosheets with Short-Range Ordered Grains to Improve Oxygen Evolution Activity. *ACS Catal.* **2021**, *11*, 6104-6112.
- [58] Dou, Y.; He, C.-T.; Zhang, L.; Yin, H.; Al-Mamun, M.; Ma, J.; Zhao, H. Approaching the Activity Limit of CoSe₂ for Oxygen Evolution via Fe Doping and Co Vacancy. *Nat. Commun.* **2020**, *11*, 1664.
- [59] Yuan, G.; Bai, J.; Zhang, L.; Chen, X.; Ren, L. The Effect of P Vacancies on the Activity of Cobalt Phosphide Nanorods as Oxygen Evolution Electrocatalyst in Alkali. *Appl. Catal. B Environ.* **2021**, *284*, 119693.
- [60] Yang, J.; Yu, C.; Hu, C.; Wang, M.; Li, S.; Huang, H.; Bustillo, K.; Han, X.; Zhao, C.; Guo, W.; Zeng, Z.; Zheng, H.; Qiu, J. Surface-Confined Fabrication of Ultrathin Nickel Cobalt-Layered Double Hydroxide Nanosheets for High-Performance Supercapacitors. *Adv. Funct. Mater.* **2018**, *28*, 1803272.
- [61] Ji, Q.; Kong, Y.; Tan, H.; Duan, H.; Li, N.; Tang, B.; Wang, Y.; Feng, S.; Lv, L.; Wang, C.; Hu, F. *Operando* Identification of Active Species and Intermediates on Sulfide Interfaced by Fe₃O₄ for Ultrastable Alkaline Oxygen Evolution at Large Current Density. *ACS Catal.* **2022**, *12*, 4318-4326.
- [62] Tian, Y.; Liu, X.; Xu, L.; Yuan, D.; Dou, Y.; Qiu, J.; Li, H.; Ma, J.; Wang, Y.; Su, D.; Zhang, S. Engineering Crystallinity and Oxygen Vacancies of Co(II) Oxide Nanosheets for High Performance and Robust Rechargeable Zn-Air Batteries. *Adv. Funct. Mater.* **2021**, *31*, 2101239.